

The PUMAS library

Valentin Niess^{a,*}

^a *Université Clermont Auvergne, CNRS/IN2P3, LPC, F-63000 Clermont-Ferrand, France.*

Abstract

The PUMAS library is a transport engine for muon and tau leptons in matter. It can operate with a configurable level of details, from a fast deterministic CSDA mode to a detailed Monte Carlo simulation. A peculiarity of PUMAS is that it is revertible, i.e. it can run in forward or in backward mode. Thus, the PUMAS library is particularly well suited for muography applications. In the present document, we provide a detailed description of PUMAS, of its physics and of its implementation.

Keywords: muon, tau, Monte Carlo, transport, backward

PROGRAM SUMMARY

Program Title: The PUMAS library

CPC Library link to program files: (to be added by Technical Editor)

Developer's repository link: <https://niess.github.io/pumas-pages>

Code Ocean capsule: (to be added by Technical Editor)

Licensing provisions: LGPL-3.0

Programming language: C99

Nature of problem: Transport of high energy muon or tau leptons in matter.

Solution method: Transport engine with a configurable level of details, from a fast deterministic CSDA mode to a detailed Monte Carlo simulation. The transport engine can operate in both forward and backward modes.

1. Introduction

The PUMAS library was initially designed for solving the muography forward problem using the Continuous Slowing Down Approximation (CSDA), which is a deterministic transport model. The muography forward problem consists in computing the flux of atmospheric muons transmitted through dense targets ($\rho \gtrsim 1 \text{ g/cm}^3$, typically rocks), with dimensions from metres to kilometres. Inverting this flux in order to determine the target parameters, e.g. its bulk density, is an inverse problem which is beyond the scope of PUMAS.

A spectacular result of muography is the discovery of a big void in Khufu's pyramid, reported by Morishima et al. [1]. Many other applications of atmospheric muons have

*Corresponding author

Email address: niess@in2p3.fr (Valentin Niess)

been investigated as well. A detailed overview of this topic is available in the review of Bonechi et al. [2].

Then, PUMAS has been enhanced with detailed Monte Carlo capabilities similar to other existing muon transport engines, e.g. MUM [3], MUSIC [4] or PROPOSAL [5, 6]. A particular care was taken in accurately modelling the physics, not only at high energies $E \gtrsim 10$ GeV, but also at lower ones down to ~ 1 MeV kinetic energy. While only high energy atmospheric muons are expected to be transmitted through typical muography targets, low energy ones scattering on the target surface contribute to the background of muon images, as discussed by Gómez et al. [7]. Thus, accurate muography predictions require to transport muons precisely over a large range of energies covering the spectrum of atmospheric muons, e.g. up to \sim PeV energies for thick targets.

Though the primary scope of PUMAS is muography it is not limited to that. The transport engine has been extended to tau leptons in addition to muons. PUMAS is part of various experiments software, not only muography ones. For example, it is used by the Giant Radio Array for Neutrino Detection (GRAND) experiment [8] for its sensitivity study to neutrinos of cosmic origin. PUMAS is also used by the COherent Muon to Electron Transition (COMET) experiment [9] in order to estimate the rate of background events induced by atmospheric muons.

From its initial design, PUMAS retains the capacity to operate at various levels of details. The accuracy of the transport is configurable on the fly, i.e. during the particle propagation. While PUMAS is able to perform detailed Monte Carlo simulations, it can be more relevant to resort to CSDA, depending on the use case. As matter of fact, CSDA is surprisingly accurate for the muography of small targets, with an extent of less than a few hundred metres, as illustrated in section 5.1.

Being revertible is another peculiarity of the PUMAS transport engine. PUMAS can run in forward or in backward mode. The latter is implemented using a Jacobian weighting procedure described in detail in Niess et al. [10]. Combined with an accurate modelling of the physics at low energies, PUMAS is particularly efficient for simulating the background induced by scattered muons, as illustrated in section 5.3.

1.1. Scope of the document

This article provides a physics oriented description of the PUMAS library. It does not describe the library Application Programming Interface (API). It does not discuss practical examples of usage either. Those are available from the PUMAS website [11]. The backward specific implementation details have been previously addressed by Niess et al. [10], and are only briefly reported herein. For a complete overview the reader can refer to the original article on backward Monte Carlo.

The article is divided in four main sections. Section 2 discusses the interactions of muon and tau leptons with matter, as implemented in PUMAS. Section 3 provides a detailed overview of the transport algorithms available in PUMAS. Section 4 contains complementary information for more specific usages of PUMAS, e.g. composite materials or non uniform densities. Section 5 discusses a selection of validation tests of PUMAS.

This article concerns version 1.2 of PUMAS, the latest at the time of this writing. However, most physics aspects discussed herein are not bound to a specific version of PUMAS.

Table 1: Definition of physical constants and variables used in the text. A natural system of units is used where $c = 1$ and $4\pi\epsilon_0 = 1$. The values of physical constants are also indicated using PUMAS system of units, i.e. GeV and m.

Symbol	Description	Value (GeV, m)
α	Fine structure constant, $\alpha = e^2/\hbar$.	$7.29735 \cdot 10^{-3}$
\hbar	Reduced plank constant.	$1.97327 \cdot 10^{-16}$
\mathcal{N}_A	Avogadro's number.	$6.02214 \cdot 10^{23}$
m_e	Electron rest mass.	$0.51100 \cdot 10^{-3}$
r_e	Classical electron radius, $r_e = \alpha\hbar/m_e$.	$2.81794 \cdot 10^{-15}$
m	Projectile (muon or tau) rest mass.	
E	Projectile total energy, $E = \gamma m$.	
p	Projectile momentum, $p = \beta E$.	
T	Projectile kinetic energy, $T = E - m$.	
z	Projectile charge number, $z = \pm 1$.	
Z	Target atomic charge number.	
A	Target atomic mass number.	
M	Target average molar mass, (4).	
I	Target mean excitation energy, (41).	
a_S	Target electronic shells scaling factor, (44).	
σ	Reaction cross-section.	
$\nu(x)$	Projectile (fractional) energy loss, (1).	
$\theta(\mu)$	Projectile deflection angle (parameter), (2).	
$\nu_C(\mu_C)$	Energy (angular) cutoff for hard collisions.	
$\Lambda_h(\Sigma_h)$	Hard interaction length ($\Sigma_h = 1/\Lambda_h$), (71).	
$S(S_s)$	Material (soft) stopping power, (5).	
$\lambda_1(\lambda_{1,s})$	(Restricted) transport mean free path, (6).	
$\Omega(\Omega_s)$	(Soft) energy straggling, (80).	

1.2. Common definitions

Before getting into the details, let us introduce some notations and definitions used throughout the discussion. A summary of those can be found in table 1. It should be noted that we use a natural system of units where $c = 1$ and $4\pi\epsilon_0 = 1$.

Let us first consider a single collision of a muon or tau projectile on a target atom. Let m , E and p denote the rest mass, the total energy and the momentum of the projectile before the collision. The relativistic factors of the projectile are $\beta = p/E$ and $\gamma = E/m$. For transport problems, we find more natural to consider the kinetic energy $T = E - m$ instead of the total energy E of the projectile. If not explicitly specified, the term “energy” stands for the projectile kinetic energy herein.

The parameters of the target atom are its charge number Z and its mass number A . Let σ denote the microscopic cross-section of this reaction. The collision parameters of interest to us are the projectile energy loss ν and its deflection angle θ , defined as $\cos \theta = \vec{p} \cdot \vec{p}' / (pp')$, with p' the projectile momentum after the collision. The Differential

Cross-Section (DCS) or Doubly Differential Cross-Section (DDCS) w.r.t. to collision parameters are written using Leibniz notation, e.g. $d\sigma/d\nu$.

In some cases, it is convenient to consider reduced collision parameters x and μ instead of ν and θ . Those are defined as

$$x = \nu/T, \quad (1)$$

$$\mu = (1 - \cos \theta)/2. \quad (2)$$

The propagation of a muon or tau leptons through matter can be considered as a succession of independent collision processes with “isolated” atoms constituting the target material. An important exception to the isolated assumption is the collision with bound atomic electrons. Thus, the target material reduces to an atomic mixture together with an electronic structure. Let f_i denote the mass fractions of constituent atomic elements of the material and A_i their corresponding mass numbers. Let σ_{el} be the cross-section for collisions with bound electrons of the material and σ_{ij} the one for collisions on atom i with physics process j . The total cross-section σ is given by

$$\frac{1}{M}\sigma = \sum_{i,j} \frac{f_i}{A_i} \sigma_{ij} + \frac{1}{M}\sigma_{el}, \quad (3)$$

where M is the average molar mass of the atomic mixture, defined as

$$\frac{1}{M} = \sum_i \frac{f_i}{A_i}. \quad (4)$$

The transport of muon or tau particles through matter implies a large number of collisions, most of which occur with little energy loss or deflection. Those soft events are thus best treated collectively. Two quantities are of particular interest when considering collective effects: the stopping power, denoted S , and the transport mean free path, denoted λ_1 . When considering only soft collisions with energy transfer below some cutoff value ν_c , one gets the soft stopping power

$$S_s(T, \nu_c) = \frac{N_A}{M} \int_0^{\nu_c} \frac{d\sigma}{d\nu}(T) \nu d\nu. \quad (5)$$

The total stopping power is $S(T) = S_s(T, T)$. Note that we use the mass stopping power. In order to get the stopping power per path length, one must multiply S or S_s by the density of the target material.

The transport mean free path $\lambda_{1,s}$ restricted to soft collisions with $\mu \leq \mu_c$ is

$$\frac{1}{\lambda_{1,s}(T, \mu_c)} = 2 \frac{N_A}{M} \int_0^{\mu_c} \frac{d\sigma}{d\mu}(T) \mu d\mu. \quad (6)$$

As for the stopping power, $\lambda_{1,s}$ is defined per mass of the target material. The total transport mean free path is $\lambda_1(T) = \lambda_{1,s}(T, 1)$. The transport mean free path is the analogue of the stopping power for angular deflections. It is directly related to the multiple scattering angle after a large number of collisions.

A target material of particular importance for muography is “standard rock”. This is a fictitious material whose properties approximate an average rock of the Cayuga Rock

Salt Mine near Ithaca, New York. Let us follow the definition of Groom et al. [12]. Standard rock is thus made of a single fictitious atom of “rockium” (Rk) with $Z = 11$ and $A = 22$ g/mol. It has the electronic structure of calcium carbonate, but its density is 2.65 g/cm³. Let us point out that real rocks are actually composite materials made of several minerals. However, standard rock has been established as a convenient standard over years in the astroparticle community. Hence, it is used as reference material herein.

2. Interactions of muons and taus with matter

In the present section we review the interactions of muon and tau leptons with matter, as implemented in PUMAS. The interactions of muons and taus are described with the same models. These models differ from the one used for electrons due to the larger masses of muons and taus. In the following we focus on the case of muons in order to simplify the discussion. In addition we limit the discussion to collisions with a single atomic element, except for electronic¹ collisions, discussed in section 2.2.

The interactions of muon and tau leptons with matter consist of five physics processes, discussed further in this section. The contributions of these processes to the total stopping power is shown on figure 1, for a muon in standard rock.

2.1. Elastic collisions

The elastic collision of charged particles with atoms is a scattering process, $\ell + Z \rightarrow \ell + Z$. This collision is described by a single parameter, the energy loss ν or alternatively the scattering angle θ . Both are related by collision kinematics.

Elastic collisions occur with a negligible energy transfer compared to other processes discussed hereafter (see e.g. figure 1). They are however the main contribution to the deflection of muons from their initial trajectory, as further discussed in section 3. Thus, unlike other processes, elastic collisions are parametrized by an angular coordinate rather than by the energy loss.

In PUMAS, elastic collisions are modelled following Salvat [13], with some modifications discussed below.

2.1.1. Elastic DCS in the centre of mass frame

For fast projectiles, the elastic process is essentially an electrostatic interaction between a point-like particle and the target atom field, which is considered as unaltered over the course of the interaction. The corresponding radial symmetric interaction potential is

$$V(r) = \frac{zZe^2}{r}\omega(r), \quad (7)$$

where $\omega(r)$ is a screening function depending on the distance r between the projectile and the target atom. For a point-like nucleus, the atomic screening is well approximated by a sum of exponentials:

$$\omega(r) = \sum_{i=1}^n a_i e^{-b_i r}. \quad (8)$$

¹In this manuscript we use “electronic” to refer to scattering from atomic electrons.

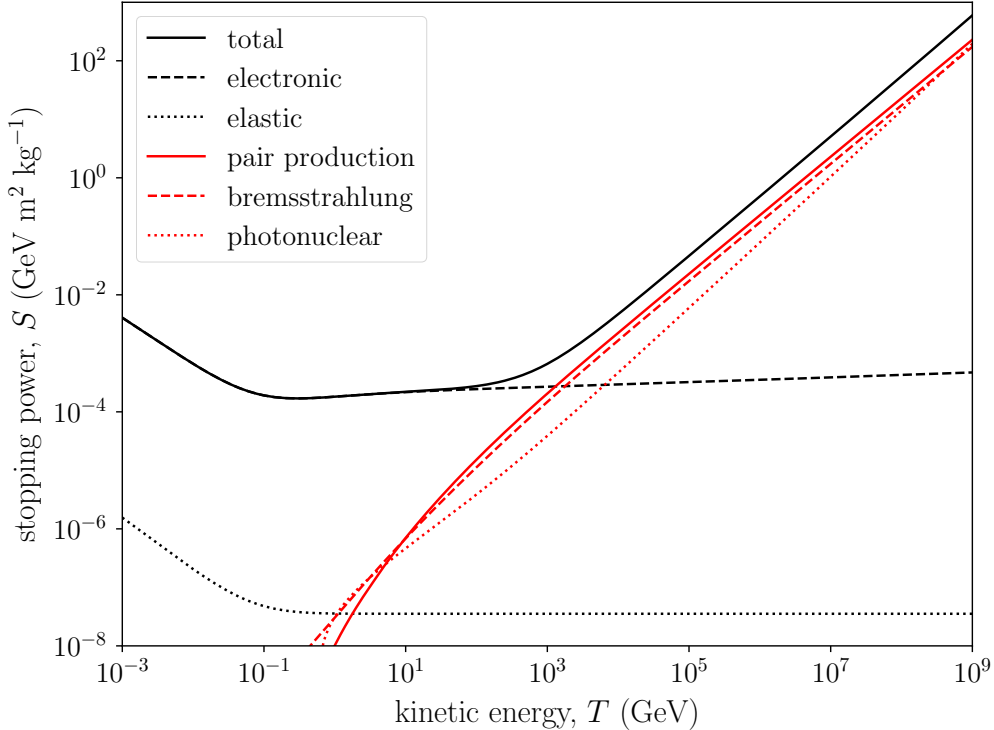


Figure 1: Stopping power, S , for a muon in standard rock. The total stopping power is indicated as well as the individual contributions of the different processes discussed in section 2.

The coefficients a_i and b_i and the number of terms n depend on Z . In PUMAS, we use the results of Salvat et al. [14] as coefficients values. These coefficients have been obtained from self consistent Dirac-Hartree-Fock-Slater (DHFS) calculations. However, for $Z = 1$ we use a single exponential instead, as explained in Appendix D.

The target recoil is accounted for by considering the collision in the Centre of Mass (CM) frame but with an effective projectile mass (see e.g. Boschini et al. [15]). Let p_0 denote the projectile momentum in the CM frame. The projectile and target energies are individually conserved, in the CM frame, but the momentum direction changes by an angle θ_0 . Within the eikonal approximation, the elastic DCS in the CM frame is given by

$$\frac{d\sigma_0}{d\mu_0} = 4\pi \frac{p_0^2}{\hbar^2} \left| \mathcal{H}_0 \{ e^{i\varphi(r)} - 1 \} (k_0) \right|^2, \quad (9)$$

$$\varphi(r) = -2\xi \int_r^{+\infty} \frac{\omega(r')}{\sqrt{r^2 - r'^2}} dr', \quad (10)$$

where $k_0 = 2\frac{p_0}{\hbar} \sqrt{\mu_0}$ and $\mu_0 = \frac{1}{2}(1 - \cos(\theta_0))$. \mathcal{H}_0 is the Hankel transform of order zero,

defined as

$$\mathcal{H}_0\{f\}(k) = \int_0^{+\infty} J_0(kr)f(r)rdr, \quad (11)$$

where J_0 is the Bessel function of the first kind and of order zero (see e.g. Piessens [16]).

The prefactor ξ appearing in the eikonal phase φ is defined as

$$\xi = \frac{\alpha z Z}{\beta}. \quad (12)$$

Note that ξ depends on the projectile relative speed β in the laboratory frame, not in the CM one.

Note also that Salvat [13] applies an extra correction to the eikonal phase following Wallace [17]. However, for the present scope, i.e. muon or tau projectiles with kinetic energy $T \geq 1$ MeV, this correction is negligible, as shown in Appendix A. It is thus not considered in PUMAS.

For exponential screening functions given by equation (8), the eikonal phase is written as

$$\varphi(r) = -2\xi \sum_{i=1}^n a_i K_0(b_i r), \quad (13)$$

where K_0 is the modified Bessel function of the second kind and of order zero. The Hankel transforms of K_0 and of K_0^2 are (see e.g. table 8.3 of Erdélyi et al. [18])

$$\mathcal{H}_0\{K_0(b_i r)\}(k) = \frac{1}{k^2 + b_i^2}, \quad (14)$$

$$\mathcal{H}_0\{K_0^2(b_i r)\}(k) = \frac{1}{k\sqrt{k^2 + 4b_i^2}} \ln \left(\frac{\sqrt{k^2 + 4b_i^2} + k}{\sqrt{k^2 + 4b_i^2} - k} \right). \quad (15)$$

Expanding the exponential in equation (9) at leading order in ξ yields

$$\frac{d\sigma_0}{d\mu_0} = \frac{\pi\hbar^2}{p_0^2} \left(\xi \sum_{i=1}^n \frac{a_i}{\mu_i + \mu_0} + \mathcal{O}(\xi^2) \right)^2, \quad (16)$$

where μ_i is an angular parameter accounting for the nuclear charge screening, defined as

$$\mu_i = \left(\frac{\hbar b_i}{2p_0} \right)^2. \quad (17)$$

2.1.2. Coulomb correction

The elastic DCS given by equation (16) corresponds to the first Born approximation. In order to improve the accuracy of this result, one could compute higher order terms in ξ or integrate the eikonal amplitude numerically. However, this would not be practical within a Monte Carlo like PUMAS. Thus, it is customary to instead use the DCS obtained from the first Born approximation, but with an effective screening parameter $\tilde{\mu}_i$ set in order to reproduce the multiple scattering distribution obtained with the eikonal DCS.

For this purpose, the Coulomb correction computed by Kuraev et al. [19] is used in PUMAS. The screening parameters μ_i are increased by

$$\begin{aligned}\tilde{\mu}_i &= \mu_i e^{2f(\xi)}, \\ f(\xi) &= \Re\{\psi(1+i\xi) - \psi(1)\},\end{aligned}\tag{18}$$

where ψ is the digamma function. For $\xi < 1$, equation (39) of Kuraev et al. provides an accurate approximation of $f(\xi)$. For higher values of ξ , the asymptotic expansion of the digamma function is more efficient. It is given by

$$f(\xi) = \frac{1501}{2520} + \ln(\rho) - \frac{1}{2\rho^2} - \frac{\cos(2\phi)}{12\rho^2} - \frac{\cos(4\phi)}{120\rho^4} - \frac{\cos(6\phi)}{252\rho^6} + \mathcal{O}\left(\frac{1}{\rho^8}\right),\tag{20}$$

where $\rho^2 = 1 + \xi^2$ and $\tan(\phi) = \xi$.

Note that the Coulomb correction computed by Kuraev et al. assumes a single exponential term for the atomic screening ω . It is shown in [Appendix B](#) that the same Coulomb correction can be applied to a weighted sum of exponentials as given by equation (8).

2.1.3. Nuclear form factor

At large scattering angles, i.e. small impact parameters, the finite size of the nucleus charge needs to be taken into account. This effectively modifies the interaction potential V by adding an extra term to the screening function:

$$\omega(r) = \sum_{i=1}^n a_i e^{-b_i r} + \Delta\omega_N(r),\tag{21}$$

$$\Delta\omega_N(r) = \int_0^r \rho_N(r') 4\pi r'^2 dr' + r \int_r^{+\infty} \rho_N(r') 4\pi r' dr' - 1,\tag{22}$$

where ρ_N is the nuclear charge density normalized to one.

It would be convenient to consider an exponential distribution for the nuclear charge distribution, as previously. The exponential distribution leads to a rational fraction in μ for the DCS, which can be integrated analytically. However, the nuclear density has a close to uniform core. Therefore, exponential functions are a rough approximation in this case. Nevertheless, depending on the use case the exponential density might be accurate enough, as discussed in [Appendix D](#).

In order to get a more accurate description of the nucleus charge, the uniform-uniform model of Helm [20] is used in PUMAS. The nuclear density is parametrized by a convolution product of two uniform spheres. Let us further assume that the spheres are identical of radius R_N . The corresponding U^2 nuclear density is given by

$$\rho_{U^2}(r) = \begin{cases} \frac{3}{64\pi R_N^3} \left(16 - \frac{12r}{R_N} + \frac{r^3}{R_N^3}\right) & \text{if } r < 2R_N \\ 0 & \text{otherwise} \end{cases}.\tag{23}$$

The model parameter R_N can be determined from experimental values of nuclear charge radii, e.g. as compiled by Vries et al. [21]. The values used in PUMAS for isotopic mixtures are given in [Appendix C](#).

Computing the modified DCS using the eikonal approximation in equation (9) would be rather involved. Fortunately, since atomic and nuclear screenings operate at different length scales, the nuclear contribution to the screening function can be taken into account by factorising the elastic DCS with a nuclear form factor $|F_N|^2$ (see e.g. Butkevich et al. [22] or Salvat et al. [23]). Within the first Born approximation, the form factor is the Fourier transform of the charge density. For the U^2 distribution one obtains

$$F_{U^2}(k_0) = \left| \frac{3}{(k_0 R_N)^3} (\sin(k_0 R_N) - k_0 R_N \cos(k_0 R_N)) \right|^2. \quad (24)$$

Note that $F_{U^2} = F_U^2$, where F_U is the form factor obtained for a uniform sphere or radius R_N .

Figure 2 shows a comparison of the U^2 form factor to the experimental data of Jansen et al. [24] and Sick and McCarthy [25], obtained from electron scattering on ^{12}C . Similar results are obtained for other atomic elements, e.g. ^{16}O . The form factor for the exponential density is also indicated. The U^2 distribution reproduces well the main peak of the form factor using a single parameter R_N . But, this simple model fails to reproduce higher order harmonics. However, this is not considered relevant for the present purpose. Let us point out that we also investigated the use of two different radii, R_1 and R_2 , instead of a single one. This was not able to improve the fit of secondary peaks, while requiring $R_1 \simeq R_2$ in order to fit the main peak. Note also that using a single sphere instead of a U^2 convolution product results in a too smooth decrease of the form factor.

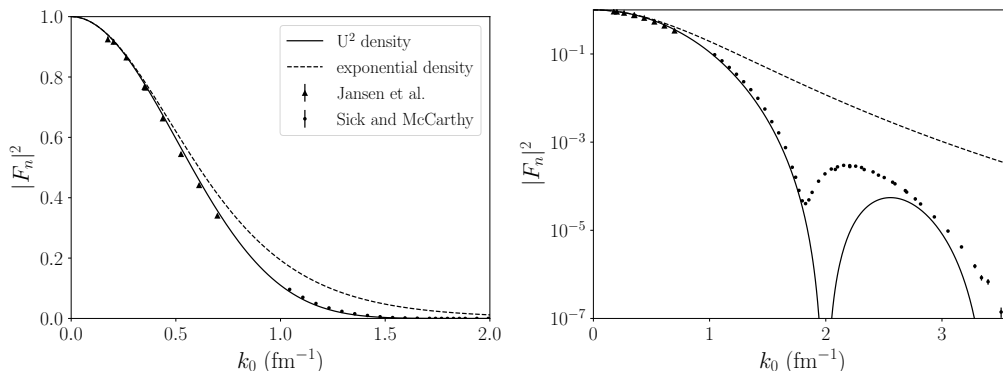


Figure 2: Nuclear form factor, $|F_N|^2$, for ^{12}C using a linear (left) or logarithmic (right) scale. Markers are experimental results from Jansen et al. [24] and Sick and McCarthy [25]. The solid and dashed lines correspond to parametrizations using a U^2 or exponential nuclear charge density.

Let us recall that the nuclear form factors considered so far have been obtained from the first Born approximation. In the case of an exponential density, it is shown in Appendix B that the Coulomb correction from Kuraev et al. [19] is still valid. It amounts to rescaling the nuclear radius parameter, or the momentum transfer k_0 , by

$$\tilde{R}_N = R_N e^{-f(\xi)}, \quad (25)$$

where $f(\xi)$ was given previously in equation (18). In the case of the U^2 distribution we assume that this rescaling is valid as well.

2.1.4. Spin correction

The elastic DCS discussed previously have been derived for spinless projectiles. In order to account for the muon or tau spin we follow Salvat [13] and apply an additional multiplicative factor \mathcal{R}_s defined as the ratio of the spin 1/2 to the spin 0 elastic DCS obtained from the first Born approximation. It is given by

$$\mathcal{R}_s = 1 - \beta^2 \mu_0. \quad (26)$$

2.1.5. Total elastic DCS

Collecting all terms, PUMAS uses the following elastic DCS in the CM frame:

$$\frac{d\sigma_0}{d\mu_0} = \frac{\pi r_e^2 m_e^2 Z^2}{\beta^2 p_0^2} \left(\sum_{i=1}^n \frac{a_i}{\tilde{\mu}_i + \mu_0} \right)^2 \left| F_U \left(\sqrt{\frac{\mu_0}{\tilde{\mu}_{n+1}}} \right) \right|^4 (1 - \beta^2 \mu_0), \quad (27)$$

where

$$F_U(x) = \frac{3}{x^3} (\sin(x) - x \cos(x)), \quad (28)$$

and

$$\tilde{\mu}_{n+1} = \left(\frac{\hbar e^{f(\xi)}}{2p_0 R_N} \right)^2. \quad (29)$$

The elastic DCS in the laboratory frame can be computed from the CM one using Lorentz transform e.g. as detailed by Salvat [13]. However, in practice it is seldom required to transform the CM DCS in PUMAS. For example, the scattering angle in an elastic collision is simulated in the CM frame, and then transformed back to the laboratory frame. Additional technical details are provided in [Appendix D](#).

The energy lost in elastic collisions is related to the scattering angle θ (see e.g. equation (49) from Salvat [13]). For muon and tau leptons, elastic collisions contribute to less than 0.1% to the stopping power, for atomic elements ranging from hydrogen to uranium. Therefore, elastic collisions are approximated as lossless in PUMAS.

2.2. Electronic collisions

The electronic energy loss consists of inelastic collisions of the projectile with the bound electrons of the target resulting in an excited electronic state. Such collisions may lead to the ionisation of the target with ejection of a fast electron, a.k.a. delta ray. As for elastic collisions, in PUMAS, electronic collisions are modelled following Salvat [13] with some modifications discussed below.

2.2.1. Electronic DCS

The target electronic structure is represented by n shells with binding energies E_k and occupancy numbers Z_k . The total electric charge is $Z = \sum Z_k$. Note that the additivity assumption over atomic constituents is not valid for the electronic DCS. I.e. the target electronic structure must be considered as a whole in this case.

Following Salvat [13], the electronic shells are modelled as independent δ -oscillators with Generalized Oscillator Strength (GOS) f_k given by

$$f_k(\nu, Q) = \begin{cases} \delta(\nu - I_k) & \text{if } Q \leq E_k \\ \delta(\nu - Q) & \text{otherwise} \end{cases}, \quad (30)$$

where Q is the recoil energy of the collided electron and $I_k > E_k$ the resonance energy of the δ -oscillator.

The electronic DCS can be computed from the GOSs as in Fano [26]. It is obtained by summing up the contributions of each shell and by integrating out the electron recoil, taking into account the medium dielectric polarization. Details of the computation are provided in the PENELOPE-2014 manual [27]. The result can be expressed as:

$$\frac{d\sigma}{d\nu} = \sum_{k=1}^n Z_k \left(\frac{d\sigma_{C,k}}{d\nu} + \frac{d\sigma_{D,k}}{d\nu} \right), \quad (31)$$

where $\sigma_{C,k}$ is the cross-section for close collisions ($Q > E_k$) with the k^{th} shell and $\sigma_{D,k}$ the cross-section for distant collisions ($Q \leq E_k$).

The DCS for close collisions is given by

$$\frac{d\sigma_{C,k}}{d\nu} = \begin{cases} \frac{2\pi r_e^2 m_e}{\beta^2} \left[\frac{1}{\nu^2} - \frac{\beta^2}{\nu_{\max}} \frac{1}{\nu} + \frac{1}{2E^2} \right] & \text{if } E_k \leq \nu \leq \nu_{\max}, \\ 0 & \text{otherwise} \end{cases}, \quad (32)$$

where

$$\nu_{\max} = \frac{2m_e \beta^2 \gamma^2}{1 + 2\gamma \frac{m_e}{m} + \left(\frac{m_e}{m}\right)^2}. \quad (33)$$

The DCS for distant collisions has a discrete structure, contrary to the close one. Furthermore, following Fano [26], transverse interactions are impacted by dielectric couplings leading to the ‘‘density effect’’, initially studied by Fermi [28]. The corresponding DCS is given by

$$\frac{d\sigma_{D,k}}{d\nu} = \frac{2\pi r_e^2 m_e}{\beta^2} \left[\ln \left(\frac{2m_e \beta^2 \gamma^2 E_k}{I_k^2 + E_F^2} \right) + \frac{E_F^2}{\gamma^2 E_p^2} - \beta^2 \right] \frac{\delta(\nu - I_k)}{I_k}. \quad (34)$$

The plasma energy is

$$E_p = \hbar\omega_p \simeq 28.816 \text{ eV} \sqrt{\frac{\rho}{\text{g cm}^{-3}} \frac{\text{g mol}^{-1}}{M}} Z \quad (35)$$

where ρ is the target density. The parameter E_F appearing in equation (34) stems from the screening of distant interactions due to the medium dielectric properties. It is obtained by solving

$$\sum_{k=1}^n \frac{Z_k}{I_k^2 + E_F^2} = \frac{Z}{\gamma^2 E_p^2}. \quad (36)$$

The parameter E_F increases with the projectile energy. At high energies it reaches an asymptotic value, $E_F \rightarrow \gamma E_p$, resulting in the density effect saturation of the energy loss. Note that the previous equation (36) has no positive solution for E_F^2 when

$$\sum_{k=1}^n \frac{Z_k}{I_k^2} \leq \frac{Z}{\gamma^2 E_p^2}. \quad (37)$$

In this case there is no density effect, as can be seen e.g. from Appendix B of Fano [29]. Then, it is correct to set $E_F = 0$ in equation (34).

2.2.2. Radiative correction

At high energies, the interaction of the projectile with atomic electrons can result in knock-on electrons with the creation of a bremsstrahlung photon. This process was studied in detail by Kelner et al. [30]. The bremsstrahlung photon can be emitted by the muon or by the knock-on electron. The former case is considered later in section 2.3.1. The latter case is accounted for by a radiative correction to the close electronic cross-section:

$$\frac{d\sigma'_{C,k}}{d\nu} = \frac{d\sigma_{C,k}}{d\nu} (1 + \Delta_{e\gamma}). \quad (38)$$

Following Sokalski et al. [3], the radiative correction is given by

$$\Delta_{e\gamma}(\nu) = \frac{\alpha}{2\pi} \ln\left(1 + \frac{2\nu}{m_e}\right) \left[\ln\left(\frac{4E(E-\nu)}{m^2}\right) - \ln\left(1 + \frac{2\nu}{m_e}\right) \right]. \quad (39)$$

Note that this correction is suppressed for $\nu \ll m_e$. Thus, it does not impact the total cross-section for close interactions, which is essentially due to collisions with $\nu \simeq E_k \ll m_e$. However, $\Delta_{e\gamma}$ increases the electronic energy loss at high energies. This is discussed further below.

2.2.3. Stopping power

Let I_{max} denote the maximum value of the union of the sets $\{E_k\}$ and $\{I_k\}$. Then, collecting previous expressions and assuming $I_{max} \ll \nu_C \leq \nu_{max}$, the soft electronic stopping power is given by

$$S_s(T, \nu_C) = \frac{2\pi r_e^2 m_e Z \mathcal{N}_A}{\beta^2 M} \left[\ln\left(\frac{2m_e \beta^2 \gamma^2 \nu_C}{I^2}\right) - \beta^2 \left(1 + \frac{\nu_C}{\nu_{max}}\right) - \delta_F + \frac{\nu_C^2}{4E^2} + \delta_{e\gamma}(\nu_C) \right], \quad (40)$$

where the material mean excitation energy I and the Fermi density effect correction δ_F are

$$Z \ln I = \sum Z_k \ln I_k \quad (41)$$

$$\delta_F = \sum_{k=1}^n \frac{Z_k}{Z} \ln\left(1 + \frac{E_F^2}{I_k^2}\right) - \frac{E_F^2}{\gamma^2 E_p^2}. \quad (42)$$

A remarkable feature of the electronic stopping power is that, apart from the density effect, the details of the electronic structure are summarised by the mean excitation energy I . The latter can be estimated by various means. In PUMAS, we use the values compiled by the Particle Data Group [31] (PDG) for different materials, available from their website. When no data are available for a specific material, then Bragg additivity rule is used by summing up the contributions to the electronic stopping power of its atomic elements, as in equation (41).

The factor $\delta_{e\gamma}$ in equation (40) arises from the radiative correction discussed previously in section 2.2.2. An analytical approximation for $\delta_{e\gamma}$ is derived in Appendix E. One obtains

$$\delta_{e\gamma}(\nu) \simeq \frac{\alpha}{2\pi} \ln^2\left(1 + \frac{2\nu}{m_e}\right) \left[\ln(2\gamma) - \frac{1}{3} \ln\left(1 + \frac{2\nu}{m_e}\right) \right]. \quad (43)$$

The radiative correction to the electronic stopping power is significant only at high energies. At EeV it increases the electronic stopping power by 20 %. However, as it becomes significant so do also other radiative processes. Overall, the contribution of $\delta_{e\gamma}$ to the total stopping power is negligible when considering all radiative processes. Nevertheless, for consistency with other computations we include this term in the electronic stopping power.

The total electronic stopping power $S(T)$ is obtained by setting the upper bound $\nu_C = \nu_{max}$ in equation (40). Note that $\nu_{max} \geq 2m_e \gg I_{max}$ in practice. Apart from the density effect, the resulting expression is identical to Groom et al. [12]. We refer to the latter for a more in depth discussion of other potential corrections to the electronic stopping power, not included in PUMAS, since those are not relevant for the transport of muons or taus.

2.2.4. Density effect

Computing the density effect correction δ_F requires specifying the electronic structure of the target medium (actually its dielectric response). However, as was pointed out by Fano [26], “crude information on the Z_k and I_k suffices for an estimate of E_F ”. Therefore, let us simply assume that the electronic shells are the union of the atomic shells of the constituent atoms of the target, considered as isolated. I.e. the E_k are taken as the ionisation energies of free atoms, and the Z_k are the corresponding occupancies weighted by the relative densities of constituent atoms. Let us further assume that the oscillator’s resonance energies are

$$I_k = a_S E_K, \quad (44)$$

where a_S is computed from the material mean excitation energy, as

$$\ln a_S = \ln I - \frac{1}{Z} \sum_{k=1}^n Z_k \ln E_k. \quad (45)$$

The latter model is similar to Sternheimer [32], but with a simpler relationship between I_k and E_K . Instead of equation (44), Sternheimer derives the following relationship

$$I_k^2 = \begin{cases} \frac{Z_k}{Z} E_p^2 & \text{for conduction electrons} \\ a_S^2 E_k^2 + \frac{2}{3} \frac{Z_k}{Z} E_p^2 & \text{otherwise} \end{cases}. \quad (46)$$

Note that Sternheimer’s result implies assumptions, one of which is $|E_i - E_j| \gg E_p$ for all pairs of shells i, j . This is not valid in condensed media, e.g water, where hydrogen and oxygen have similar binding energies w.r.t. the plasma energy.

A detailed computation of the density effect in aluminium was done by Inokuti and Smith [33]. This computation proceeds directly from the aluminium dielectric response, which was accurately modelled from experimental data. The detailed computation of Inokuti and Smith allows a cross-check of the accuracy of other models. Figure 3 shows a comparison of the density effect computed by Inokuti and Smith to Sternheimer et al. [34] or using equation (44). In the high energy limit where the density effect matters most, δ_F is insensitive to the details of the electronic structure. Then, electrons can be considered as free and all models give the same result. In this case, the density effect depends only on the total electron density of the target, through the plasma energy E_p .

At low energies the three results disagree. However, the differences on the electronic stopping power are small, as can be seen on the right of Figure 3. Overall, for a muon we find a maximal deviation on the electronic stopping power of 0.26 % (0.21 %) by using (44) (Sternheimer et al.) instead of Inokuti and Smith density effect. The standard deviation of the differences is of 0.09 % (0.10 %).

Given the previous results, it would be tempting to consider an even simpler electronic structure with a single shell of resonance energy $I_1 = I$. This would yield the right behaviour for the stopping power at high energies. However, at intermediate energies (\sim GeV) this model result in significantly larger errors than Sternheimer et al. and our model. In the case of aluminium, we find a 3.5 % maximal deviation on the electronic energy loss when using this single shell model instead of Inokuti and Smith.

The parametrized results of Sternheimer et al. [34] are commonly used in Monte Carlo codes in order to compute the density effect. In PUMAS, the density effect is estimated directly from the atomic binding energies, as described above. In the case of standard rock, it results in a slightly larger stopping power than e.g. Groom et al. [12]. The discrepancy reaches a maximum value of 0.4 % at GeV energy. Considering the lack of data in order to discriminate the various models, this can be considered as the uncertainty on the electronic stopping power related to the density effect.

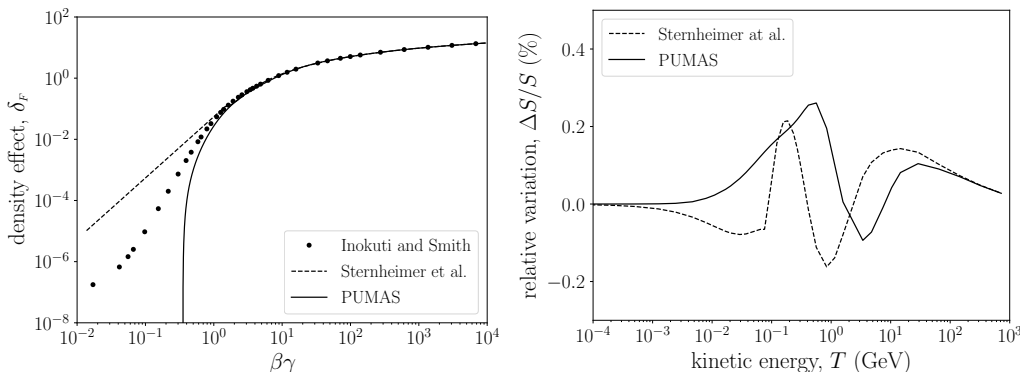


Figure 3: Density effect in aluminium and variation of the electronic stopping power for a muon using various computations. Left: density effect parameter, δ_F , according to Inokuti and Smith [33], Sternheimer et al. [34] and this work (PUMAS). Right: variation of the electronic stopping power w.r.t. Inokuti and Smith [33] by using this work (PUMAS) or Sternheimer et al. [34] computation of the density effect.

2.2.5. Angular deflections

In the general case, describing both the energy loss and the projectile deflection requires considering the DDCS for electronic collisions w.r.t. to ν and to the electron recoil energy Q . Detailed expressions are provided by Salvat [13].

Close collisions are modelled as if the scattering occurs with a free electron at rest. In this case the recoil energy is $Q = \nu$. The projectile scattering angle θ is given by the kinematics, as

$$\cos \theta = \frac{p^2 - \nu(E + m_e)}{p\sqrt{p^2 + \nu^2 - 2E\nu}}. \quad (47)$$

Thus, in order to simulate close electronic collisions it is enough to randomise only the energy loss ν . The corresponding angular deflection is given by equation (47).

In order to compute the transport mean free path λ_1 a numeric integration of equation (47) would be needed. This integration is delicate due to rounding errors at high energies, since both p and ν converge towards E . Let us instead follow Salvat [13] by assuming $\nu \leq \min(\nu_{\max}, \nu_C) \ll E$. With this assumption the angular parameter μ is

$$\mu = \frac{m_e}{2p^2}\nu + \mathcal{O}(\nu^2). \quad (48)$$

Thus, for $\nu_C \ll E$ or $\nu_{\max} \ll E$ (i.e. $E \ll m^2/2m_e$), the transport mean free path restricted to soft close collisions is

$$\lambda_{1,C} = \frac{2p^2}{m_e S_C}. \quad (49)$$

In the case of distant collisions, the energy loss ν and the recoil Q are limited to small values of $\mathcal{O}(E_k)$. Therefore, one can safely assume $Q \ll m_e$ as Salvat. In addition, let us also assume $p \gg I_k$ and $\nu_C \geq I_{max}$. Thus, we obtain the following approximation for the angular DCS in distant collisions:

$$\frac{d\sigma_{D,k}}{d\mu} = \begin{cases} \frac{2\pi r_e^2 m_e}{\beta^2 I_k} \frac{1}{\mu_k + \mu} & \text{if } \mu_k + \mu \leq \frac{m_e E_k}{2p^2}, \\ 0 & \text{otherwise} \end{cases}, \quad (50)$$

where the screening parameter is

$$\mu_k = \frac{I_k^2}{4\beta^2 p^2}. \quad (51)$$

Summing up close and distant collisions, the soft transport mean free path in electronic collisions is approximated by

$$\frac{1}{\lambda_{1,s}} = \frac{2\pi r_e^2 m_e^2 Z \mathcal{N}_A}{\beta^2 p^2 M} \left[\ln\left(\frac{a_S \nu_C}{I}\right) - \beta^2 \frac{\nu_C}{\nu_{max}} + \frac{\nu_C^2}{4E^2} + \frac{1}{a_S} + \delta_{e\gamma}(\nu_C) \right], \quad (52)$$

where the contribution of distant collisions has been reduced to its leading term, $1/a_S$, with a_S the scaling parameter given by equation (45).

Numerical investigations show that equation (52) holds well even for large cutoff values, as can be seen on figure 4. In standard rock, with PUMAS default relative cutoff value of $x_C = 5\%$ the approximation error is less than 0.1% of the total transport mean free path, summing up elastic and electronic contributions. At high energy, $\nu_{\max} \rightarrow E$ (see equation (33)). Thus, for $\nu_C = T$ the assumption $\nu \leq \min(\nu_{\max}, \nu_C) \ll E$ breaks. Nevertheless, it can be seen that even in this extreme case the approximation error is small, 1.3% in standard rock, above 1 TeV. These errors are considered as acceptable for the present purpose. Equation (52) is thus used in PUMAS over all values of ν_C .

2.3. Radiative collisions

When the projectile energy is high enough, the collision with target atoms might lead to the creation of secondary particles or to the fragmentation of the target. Those

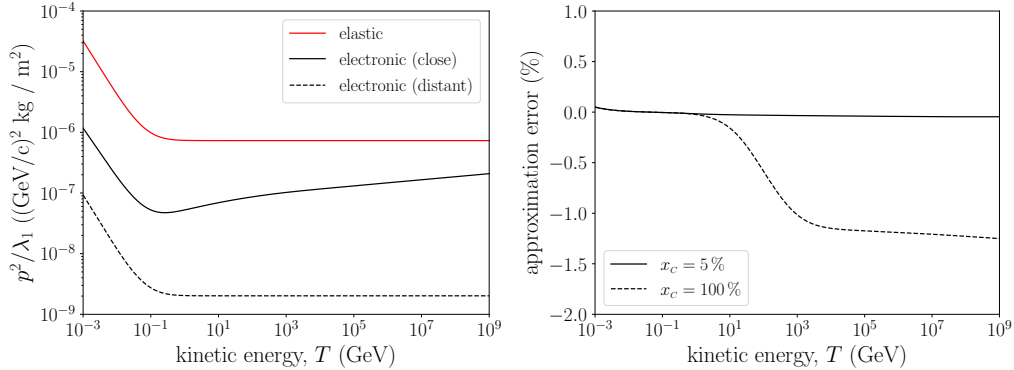


Figure 4: Transport mean free path for electronic collisions in standard rock. A muon projectile is considered. Left: normalised transport, p^2/λ_1 , for close and distant electronic collisions ($x_C = 100\%$). For purpose of comparison, the corresponding value for elastic collisions is also indicated. Right: relative error on the total transport mean free path, summing up elastic and electronic contributions, when using the approximation of equation (52). The default cutoff value used in PUMAS is $x_C = 5\%$.

collisions are conventionally designated as “radiative”. At low energy, radiative collisions contribute only marginally to the total stopping power. However, as the projectile energy increases, radiative processes becomes important. Their contribution to the stopping power increases approximately linearly with the projectile energy, contrary to electronic collisions. Thus, radiative processes are the dominant source of energy loss at high energies. The energy E_c at which half of the stopping power is due to radiative processes is called the “critical energy”. The critical energy of muons in standard rock is $E_c = 693$ GeV [12].

Contrary to electronic collisions, high energy radiative collisions are likely to result in “catastrophic events”, where the muon loses a significant fraction of its energy. The muon range thus fluctuates significantly above the critical energy. On the contrary, muons have an almost deterministic energy loss below E_c , with a well defined range given by CSDA.

Three radiative processes are of importance for the transport of muons and taus: bremsstrahlung, direct e^+e^- production and photonuclear interactions. These processes have been extensively studied in the past. Different DCS parametrizations are implemented in PUMAS. The initial implementation was done following Groom et al. [12] and Geant4 [35]. More recently updated models have been developed, especially for the PROPOSAL Monte Carlo [5, 6]. These updated models have been added in PUMAS v1.1. A summary of the DCS parametrizations available in PUMAS is given in table 2. A comparison of their stopping powers is shown on figure 5. A specific parametrization can be selected by the user during the physics initialisation. Otherwise, a default model is used as indicated in the table.

Before discussing the details of the DCS parametrizations, let us point out that the Ter-Mikaelian [36] and Landau, Pomeranchuk and Migdal [37, 38] (LPM) effects are not included in PUMAS. Those lead to a suppression of radiative DCSs due to interferences with other processes: elastic collisions of the projectile or Compton scattering of the

Table 2: DCS parametrizations implemented in PUMAS for radiative processes. The default parametrizations used in PUMAS v1.2 are indicated with a star (*) symbol.

Process	Label	Parametrization name	References
bremsstrahlung	ABB	Andreev, Bezrukov and Bugaev	[3, 40]
	KKP	Kelner, Kokoulin and Petrukhin	[5, 12, 41, 42]
	SSR*	Sandrock, Soedingrekso and Rhode	[6, 43, 44]
e^+e^- production	KKP	Kelner, Kokoulin and Petrukhin	[35, 42, 45, 46]
	SSR*	Sandrock, Soedingrekso and Rhode	[5, 44, 47]
photonuclear	BBKS	Bezrukov, Bugaev, Kokoulin and Shlepin	[5, 48–51]
	BM	Butkevich and Mikheyev	[5, 52]
	DRSS*	Dutta, Reno, Sarcevic and Seckel	[5, 53, 54]

secondary photon. However, these effects are important only at very high energies, above $\sim 10^{11}$ GeV for muons in rocks according to Koehne et al. [5]. This is thus not considered relevant for muography applications.

A priori, at high energy one must also consider the direct $\mu^+\mu^-$ production, not only the e^+e^- one. The contribution to the stopping power of the former is negligible according to Koehne et al. [5]. However, $\mu^+\mu^-$ production increases the total transmitted flux since secondary muons are produced. This was studied by Kelner et al. [39]. Their results suggest that secondary muons contribute at most at $\sim 0.1\%$ to the transmitted flux of muons at large depths. Thus, $\mu^+\mu^-$ production is not considered in PUMAS.

2.3.1. Bremsstrahlung

The bremsstrahlung process models the interaction of a charged projectile in the electromagnetic field of a nucleus resulting in the creation of a photon, as $\ell+Z \rightarrow \ell+Z+\gamma$. Three parametrizations for the DCS of this process are available in PUMAS.

The Kelner, Kokoulin and Petrukhin parametrization [41] (KKP) of the bremsstrahlung DCS was initially implemented in PUMAS according to Groom et al. [12]. In version 1.1 of PUMAS this cross-section has been updated following Koehne et al. [5]. The nuclear excitation term is taken into account (see e.g. Kelner et al. [41]), as well as a more accurate radiation logarithm computation from Kelner et al. [42].

An improved parametrization was proposed by Sandrock, Soedingrekso and Rhode [44] (SSR). This parametrization refines the modelling of atomic screening functions and takes into account radiative corrections to the bremsstrahlung cross-section from Sandrock et al. [43]. As a result, the energy loss due to bremsstrahlung increases by 2% at high energies. The PROPOSAL implementation of the SSR bremsstrahlung DCS is used in PUMAS (see e.g. Dunsch et al. [6]). The SSR parametrization is the default bremsstrahlung model for PUMAS v1.2.

The Andreev, Bezrukov and Bugaev parametrization [40] (ABB) of the bremsstrahlung DCS has been added to PUMAS as well. MUM’s implementation is used (see e.g. Sokalski et al. [3]).

In order to simulate angular deflections in bremsstrahlung processes the DDCS would

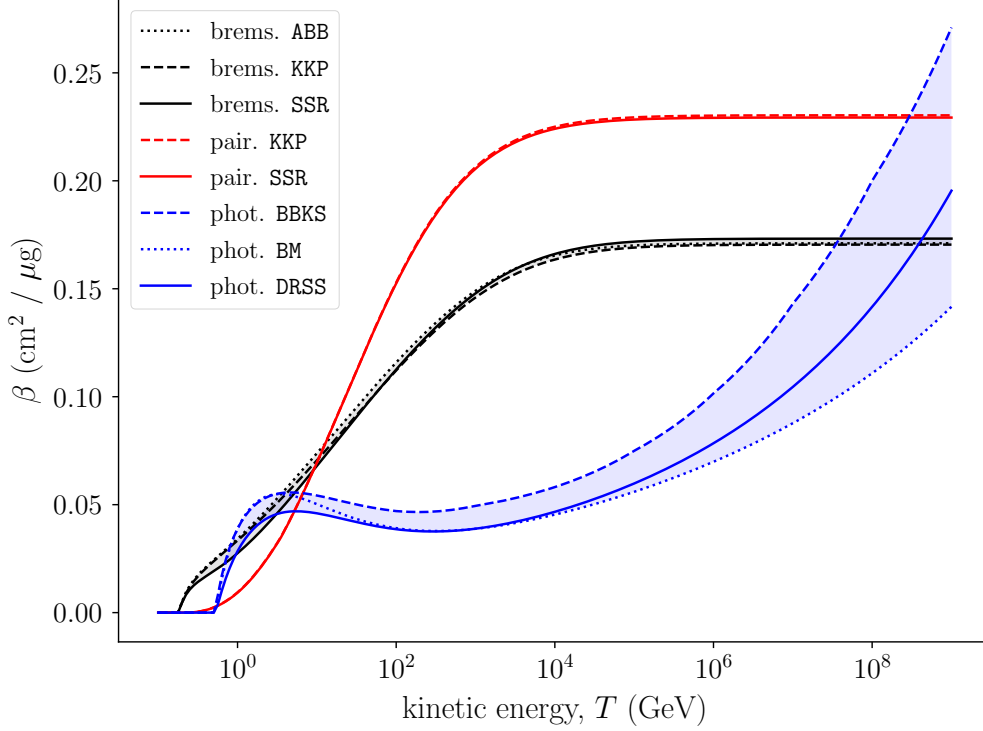


Figure 5: Normalised stopping power, $\beta = S/E$, for bremsstrahlung (black), e^+e^- production (red) and photonuclear interactions (blue). A muon in standard rock is considered. The different lines correspond to the models indicated in table 2. The default models used in PUMAS v1.2 (SSR and DRSS) are indicated with a solid line. The shaded area represent the range of variation between models for a given process.

be required. However, the parametrizations discussed previously only provide the DCS. As an alternative, we rely on the DDCS from Tsai [55], but scaled to the DCS selected in PUMAS. Thus, the DDCS used in PUMAS is

$$\frac{d^2\sigma}{d\nu d\mu} = \frac{1}{\frac{d\sigma_T}{d\nu}} \left(\frac{d^2\sigma_T}{d\nu d\mu} \right) \frac{d\sigma}{d\nu}, \quad (53)$$

where σ_T is given by Tsai [55] and where σ is the bremsstrahlung DCS actually selected.

Tsai obtains the DDCS w.r.t. the bremsstrahlung photon emission angle θ_k . In order to express the DDCS as function of the muon scattering angle θ , let us neglect the target recoil in the collision. Then, from momentum conservation one has

$$p' \sin(\theta) = \nu \sin(\theta_k), \quad (54)$$

where p' is the muon momentum after the collision and ν the energy transferred to the photon. Let us further consider the ultra-relativistic limit, where $p' \simeq E - m - \nu$ and

where both θ and θ_k are small. Neglecting Coulomb corrections, one obtains

$$\frac{d^2\sigma_T}{d\nu d\mu} = \frac{2\alpha r_e^2}{\nu} \left[(2 - 2y + y^2) \frac{\mu_0}{(\mu_0 + \mu)^2} - 4(1 - y) \frac{\mu_0^2 \mu}{(\mu_0 + \mu)^4} \right] X(\mu), \quad (55)$$

where $y = \nu/E$ and where the screening parameter is

$$\mu_0 = \frac{m^2 \nu^2}{E^2 (E - \nu)^2}. \quad (56)$$

The form factor X for an exponential distribution of the nucleus charge was computed by Tsai [55] (see also the erratum [56]). Let us recall its expression:

$$X(\mu) = \begin{cases} Z^2 \left[(1 + 2qr) \ln \left(\frac{1+qr}{r+qr} \right) - (1 - r) \frac{1+2q}{1+q} \right] & \text{if } \mu \leq \sqrt{\mu_0} - \mu_0 \\ 0 & \text{otherwise} \end{cases}, \quad (57)$$

where $q = (1 + \mu/\mu_0)^2/\mu_N$ and $r = \mu_0(1 + \mu/\mu_0)^2$. The nuclear cutoff parameter is

$$\mu_N = \frac{6\hbar^2}{m^2 \langle r^2 \rangle} \quad (58)$$

where $\langle r^2 \rangle$ is the nuclear charge radius squared given in [Appendix C](#).

2.3.2. e^+e^- production

The electron pair production process is similar to bremsstrahlung but with the direct creation of an e^+e^- pair, as $\ell + Z \rightarrow \ell + Z + e^+ + e^-$. Two parametrisations for the DCS of this process are available in PUMAS.

The Kelner, Kokoulin and Petrukhin parametrisation [45, 46] (KKP) was the first implemented in PUMAS. The KKP parametrisation provides the DDCS w.r.t. to the total energy loss ν and the e^+e^- relative energy difference ρ . The Geant4 implementation was initially used in PUMAS (see e.g. [35]). The e^+e^- production DDCS is numerically integrated over ρ using a Legendre-Gauss quadrature in $\ln(1 - \rho)$. This cross-section has been updated in version 1.1 of PUMAS. The improved radiation logarithm computation from Kelner et al. [42] is used. In addition, the order of the Legendre-Gauss numeric integration was increased from 8 to 12. With these two modifications, the PUMAS pair production DCS agrees with Koehne et al. [5] at better than 0.1%. Note that the resulting DCS is now 2% lower than the Geant4 (10.7) one in standard rock, due to these two modifications.

A refined parametrisation of the e^+e^- pair production cross-section has been proposed by Sandroek, Soedingrekso and Rhode [44] (SSR), as for the bremsstrahlung cross-section. Improvements in the modelling of atomic screening functions yield a 0.5% decrease on the energy loss w.r.t. the KKP parametrisation. Higher order radiative corrections are not currently modelled. They are estimated to be of the order of 1% (see e.g. Sandroek et al. [47] for a more detailed discussion). The PROPOSAL implementation of the SSR doubly differential cross-section is used in PUMAS. It is integrated over ρ using a Legendre-Gauss quadrature.

Note that the collision kinematics is not fully determined given only ν and ρ , even when the target recoil is neglected. Properly simulating scattering angles in e^+e^- pair

production would require a triply differential cross-section. However, since in PUMAS the distribution of secondary particles is not a concern, the following approximation is used. The e^+e^- pair is considered as a virtual photon of energy ν . Then, the pair production DDCS w.r.t. the muon angular parameter μ is approximated using equation (53), as for the bremsstrahlung process, but using the pair production DCS for $d\sigma/d\nu$.

2.3.3. Photonuclear interaction

The photonuclear process models an inelastic interaction of a lepton with a nuclei. Three parametrisations for the DCS of this process are available in PUMAS.

The Dutta, Reno, Sarcevic and Seckel [54] (DRSS) parametrisation has been initially implemented in PUMAS. It relies on the ALLM97 [53] parametrisation of the F_2 proton structure function. In the initial DRSS paper, $Z = A/2$ is assumed when modelling the atomic screening function. In PUMAS v1.1, this has been refined, e.g. as in section 2.3.2 of Koehne et al. [5]. The DRSS parametrisation requires integrating the doubly differential photonuclear cross-section over the square of the four momentum transfer Q^2 , given by

$$Q^2 = 2(E E' - pp' \cos \theta - m^2), \quad (59)$$

where p (p') is the initial (final) momentum of the muon and θ its scattering angle. The integration of the DDCS is done numerically using a Gaussian quadrature in $\ln Q^2$.

An alternative parametrisation of the F_2 neutron, proton and atomic structure functions was proposed by Butkevich and Mikhailov [52], resulting in the BM DDCS for photonuclear interactions. The PROPOSAL implementation for the BM photonuclear DDCS is used in PUMAS. As for the DRSS parametrisation, the BM DCS is integrated numerically over Q^2 using a Gaussian quadrature in $\ln Q^2$.

The initial parametrisation of Bezrukov and Bugaev [48] (BB) has been widely used in the past, e.g. by Groom et al. [12]. In this model, the photonuclear DCS is normalised to the photon-nucleon cross-section $\sigma_{\gamma N}$ for the absorption of a real photon. A refined parametrisation for the latter was proposed by Kokoulin [49]. The BB cross-section of 1981 misses a hard QCD component which makes it inaccurate at high energies, e.g. as compared to the DRSS or BM cross-sections (see Sokalski et al. [57] for a more detailed discussion). An improved model taking into account the hard QCD component was given more recently by Bugaev and Shlepin [50] (parametrised in Bugaev et al. [51]). This leads to the Bezrukov, Bugaev, Kokoulin and Shlepin (BBKS) cross-section for photonuclear interactions. The PROPOSAL implementation of this parametrisation is used in PUMAS.

The DDCS w.r.t. the angular parameter μ is related to the one in Q^2 by

$$\frac{d^2\sigma}{d\nu d\mu} = 4pp' \frac{d^2\sigma}{d\nu dQ^2}. \quad (60)$$

For the DRSS and BM parametrizations the scattering angle of the muon is thus derived from the DDCS in Q^2 . In the case of the BBKS parametrization, the DRSS DDCS is used, but rescaled to the BBKS DCS, as detailed previously for bremsstrahlung.

3. Transport algorithms

From the expressions given in section 2, it can be observed that DCSs are diverging functions for $\nu \rightarrow 0$, down to some lower bound cutoff. This implies that most collisions

are soft, i.e. resulting in a small individual energy loss and deflection. However, the sum of these soft events constitute the bulk of the energy loss and scattering over macroscopic distances. Simulating in detail every collision would be highly inefficient CPU-wise. This is seldom done in practice. Instead, one relies on condensed simulation schemes by replacing a group of collisions with an approximate condensed model, allowing to directly render the behaviour of multiple collisions. This procedure was outlined in detail by Berger [58].

PUMAS implements three algorithms for the simulation of the energy loss, designated in the following as “CSDA”, “mixed” and “straggled”. In CSDA mode, the energy loss of the projectile is deterministic given by its average value. The mixed and straggled modes are class II algorithms according to Berger’s terminology. A cutoff value ν_c is selected on the projectile energy loss in individual collisions. Events are separated into soft collisions ($\nu \leq \nu_c$) and hard ones ($\nu > \nu_c$) accordingly. Soft collisions are rendered collectively while catastrophic ones are simulated explicitly. In mixed mode the soft part is rendered by CSDA while in straggled mode soft electronic collisions are fluctuated.

The projectile deflections are rendered by a mixed algorithm as well. A cutoff is applied on the scattering angle in individual elastic collisions, following Fernández-Varea et al. [59]. This procedure reproduces the exact multiple scattering distribution and the corresponding spatial displacement when the number of elastic collisions is $n \gtrsim 20$.

The energy loss and the scattering can also be disabled, independently. Disabling all physics processes can be useful in order to cross-check the geometry implementation (see e.g. section 4.4). Furthermore, the simulation scheme can be changed on the fly during the tracking of a particle. For example, if the energy of a backward transported particle exceeds 0.1-1 TeV, then scattering can be turned off as a CPU optimisation.

Let us also recall that a peculiarity of PUMAS is that it can operate in both forward and backward Monte Carlo mode. In particular, care was taken into implementing the mixed and straggled simulation schemes in a symmetric way. In the following, we provide specific details on the simulation algorithms available in PUMAS, as well as on their implementation.

3.1. CSDA mode

CSDA is frequently used in muography applications together with the assumption that muons follow straight paths. CSDA provides accurate estimates of the transmitted flux of muons for moderate target thickness, $d \lesssim 300$ m of standard rock, as illustrated in section 5.1. For thicker targets, CSDA underestimates the transmitted flux because of strong fluctuations in the energy loss, due to radiative processes. However, when CSDA is applicable it is particularly efficient, since it provides direct semi-analytical solutions to the transport problem.

3.1.1. Forward CSDA transport

Within CSDA, the projectile energy loss per unit path length is deterministic. It is equal to the total stopping power S given by equation (5), setting $\nu_c = T$ and considering all processes discussed in section 2. In a uniform medium, S does not depend on the projectile position but only on its energy. Thus, within CSDA the curvilinear distance s along the projectile path and its kinetic energy T are equivalent representations of the

particle state. They are related by

$$\begin{aligned}\rho(s_1 - s_0) &= \int_{T_1}^{T_0} \frac{dT}{S} \\ &= R(T_0) - R(T_1),\end{aligned}\tag{61}$$

where ρ is the medium density and

$$R(T) = \int_0^T \frac{dT'}{S(T')},\tag{62}$$

is the mass CSDA range. The CSDA range is a strictly increasing function of the energy of the projectile. Let $R^{(-1)}$ denote its inverse, i.e. the minimum kinetic energy required in order to travel over a path length $\rho\Delta s$. Let us consider a particle with initial energy T_0 travelling over a distance $\Delta s = s_1 - s_0$. The particle final energy, T_1 , is obtained by inverting equation (61):

$$T_1 = \begin{cases} R^{(-1)}(R(T_0) - \rho\Delta s) & \text{if } \rho\Delta s \leq R(T_0) \\ 0 & \text{otherwise} \end{cases}.\tag{63}$$

In the case where $\rho\Delta s > R(T_0)$, the particle stops after a path length $R(T_0)/\rho < \Delta s$ with a null kinetic energy.

Note that the previous equations are not valid in a non uniform medium due to the density effect. While it is conventional to express the stopping power and CSDA range of muons per mass, this is actually miss-leading because these quantities depend on the medium density, due to δ_F . This is especially the case at energies where CSDA is a good approximation, i.e. when the stopping power is dominated by electronic collisions. However, there are some exceptions to this that are discussed further in section 4.2.

Equation (63) is used in PUMAS for transporting particles in CSDA mode. The CSDA range is pre-computed by PUMAS and tabulated as function of the projectile energy using a logarithmic sampling. Then, at runtime a lookup algorithm is used, detailed in Appendix F. The converse CSDA energy $R^{(-1)}$ is obtained from the same data and lookup algorithm, but swapping columns.

3.1.2. Backward CSDA transport

In order to introduce the case of the backward transport, let us perform a toy muography experiment. Let us consider a uniform medium as discussed previously with density ρ . Let there be a muon source located at s_0 with differential flux ϕ_0 , and let there be a counting detector located at s_1 . The expected rate of muons in the detector is

$$\tau = \int_0^\infty \int_0^\infty A(T)p(T; T_0)dT \phi_0(T_0)dT_0,\tag{64}$$

where $p(T; T_0)$ is the Probability Density Function (PDF) for a muon to exit the target with kinetic energy T given its initial energy T_0 . A denotes the detector acceptance, i.e. in this simple model the probability to detect and select a muon of energy T .

Within CSDA, p is a Dirac δ -distribution:

$$p(T; T_0) = \delta(T - T_1(T_0)),\tag{65}$$

where T_1 is given by equation (63). Inserting equation (65) into (64) and integrating out the final energy yields the CSDA rate

$$\tau = \int_0^\infty A(T_1) H(T_0 - R^{(-1)}(\rho\Delta s)) \phi_0(T_0) dT_0, \quad (66)$$

where H is the Heaviside step function. When it is further assumed that the detector acceptance A is also a step function, then equation (66) leads to an approximation frequently used in muography applications (see e.g. Nagamine et al. [60]). The accuracy of CSDA is discussed more in depth in section 5.1.

The backward formulation of the previous problem consists in a change of the integration variable from T_0 to T_1 . Inverting the CSDA transport equation (63) for T_0 yields

$$T_0 = R^{(-1)}(R(T_1) + \rho\Delta s). \quad (67)$$

The Jacobian of this change of variable is

$$\left| \frac{dT_0}{dT_1} \right| = \frac{S(T_0)}{S(T_1)}. \quad (68)$$

Thus, one obtains

$$\tau = \int_0^\infty A(T_1) \phi_0(T_0) \frac{S(T_0)}{S(T_1)} dT_1. \quad (69)$$

In PUMAS, the Jacobian factor given by equation (68) is applied to the particle weight when a backward CSDA transport is done. Let us point out that this is consistent with the backward Monte Carlo method described in Niess et al. [10], summarised hereafter.

3.2. Mixed mode

In mixed mode, a class II Monte Carlo algorithm is used following Berger [58]. The cutoff value between soft and hard collisions is set to a fraction x_c of the projectile kinetic energy. By default $x_c = 5\%$. This can be modified during the physics initialisation. A 5% relative cutoff might seem rather high. However, it was shown by Sokalski et al. [3] to give accurate results for the transport of a continuous flux, e.g. for atmospheric muons. It is confirmed in section 5.1 that this cutoff value is appropriate for most muography applications, i.e. for targets thinner than ~ 3 km of standard rock. However, note that in order to simulate the impulse response for a mono-energetic muon beam, a smaller cutoff would be needed as discussed by Koehne et al. [5].

3.2.1. Forward mixed transport

The energy loss due to soft collisions is rendered with CSDA. It is computed using equation (5), as previously, but restricted to soft collisions with $\nu \leq \nu_c$. All processes are considered except elastic collisions. However, for electronic losses an effective model is used, described below. This model reproduces the exact soft stopping power and DCS for $\nu_c \gtrsim I$, where I is the mean excitation energy.

Let us consider the following effective DCS for electronic collisions with the i^{th} atom of the target material:

$$\frac{d\sigma_{C,i}}{d\nu} = \begin{cases} \frac{2\pi r_e^2 m_e Z_i}{\beta^2} \left[\frac{1}{\nu^2} - \frac{\beta^2}{\nu_{\max}} \frac{1}{\nu} + \frac{1}{2E^2} \right] & \text{if } \alpha I_i \leq \nu \leq \nu_{\max}, \\ 0 & \text{otherwise} \end{cases}, \quad (70)$$

where $\alpha = 0.62$ corresponds to the ratio of the ionisation energy of liquid hydrogen to its mean excitation energy (see e.g. Zyla et al. [31]).

Summing over atomic elements yields the correct electronic DCS for $\nu \geq I_{max}$, apart from the radiative term, as can be seen from section 2.2. I.e., for ν large w.r.t. the atomic binding energies, the electronic DCS does not depend on the details of the electronic structure, but only on the total electron number $Z = \sum Z_i$. However, the stopping power does depend on the electronic structure. Therefore, let us use the exact stopping power given by equation (5) with $\nu_C = \nu_{max}$, but let us subtract from the latter the contributions of hard electronic collisions as given by our effective DCSs, i.e. equation (70). This gives the correct soft stopping power for $\nu \geq I_{max}$, apart from the radiative term $\Delta_{e\gamma}$. For the latter, all collisions are treated as soft, i.e. $\nu_C = \nu_{max}$.

We could have included the radiative term to the effective DCS. However, this would have significantly complicated the simulation of hard electronic collisions while this correction is overall negligible. Therefore, we only take it into account for the stopping power. Note also that the ‘‘atomic’’ mean excitation energy is used in equation (70) instead of the material one. As a result, the material can be considered as a pure atomic mixture for *all* hard collisions.

The use of an effective model simplifies the implementation of electronic processes, but at the cost of a loss of accuracy at \sim MeV energies and large Z . However, as discussed in Appendix A, the range of muons is negligible in this case, $\lesssim 10 \mu\text{m}$. Hence, this is not relevant for muography applications considering targets larger than ~ 1 m. Note also that contrary to Salvat [13], with this effective model we do not explicitly simulate distant hard collisions with atomic electrons. This is not a problem since we are not concerned by the spectrum of secondary knock-on electrons, but only by the projectile energy loss.

The mixed Monte Carlo algorithm requires specifying the interaction length restricted to hard collisions:

$$\frac{1}{\Lambda_h} = \mathcal{N}_A \sum_{i,j} \frac{f_i}{A_i} \int_{\nu_C}^{\infty} \frac{d\sigma_{ij}}{d\nu} d\nu, \quad (71)$$

where f_i and A_i are the mass fraction and the atomic weight of the i^{th} constituent atom of the medium. The sum over j runs over all physics processes except elastic collisions. Note that for electronic collisions the effective DCS described previously is used.

Let us further consider a uniform medium such that the stopping power per unit mass does not depend on the target density. Then, as discussed previously in the CSDA case, between two hard collisions the projectile kinetic energy T and its path length s are analogous variables. Let T_0 denote the projectile kinetic energy at s_0 . The probability for a hard collision to occur with $T \leq T_1$ can be expressed semi-analytically, e.g. as Berger [58]. It is given by

$$P(T \leq T_1; T_0) = e^{N_h(T_1) - N_h(T_0)}, \quad (72)$$

where

$$N_h(T) = \int_0^T \frac{dT'}{\Lambda_h S_s}, \quad (73)$$

is the average number of hard collisions over the path from T to 0 and where S_s is the stopping power restricted to soft collisions as discussed previously.

Equation (72) provides an easy way to sample the energy T_1 at which the next hard collision would occur using the inverse Cumulative Distribution Function (CDF) method. Let $N_h^{(-1)}$ denote the inverse of N_h . Then, T_1 is given by

$$T_1 = \begin{cases} N_h^{(-1)}(N_h(T_0) + \ln \xi) & \text{if } \ln \xi > -N_h(T_0) \\ 0 & \text{otherwise} \end{cases}, \quad (74)$$

where ξ is a random number uniformly distributed in $[0, 1]$. Note that if $T_1 = 0$, then the projectile actually lost all its energy before any hard collision occurred. The path length s_1 at which the hard collision occurs is given by equation (61), but using the range R_s restricted to soft collisions.

In practice, the quantities N_h and R_s are tabulated at PUMAS initialisation, and then read back during the simulation using the lookup algorithm detailed in Appendix F. Between two hard collisions, the projectile behaves as in CSDA mode, but using a soft stopping power S_s and range R_s instead of S and R .

3.2.2. Backward mixed transport

In backward mode, the energy of the previous hard collision is obtained by inverting equation (74) for T_0 . Thus

$$T_0 = N_h^{-1}(N_h(T_1) - \ln \xi). \quad (75)$$

It is not enough to invert the transport equation in order to preserve the flux of particles in a backward process. As demonstrated in Niess et al. [10] a backward Monte Carlo weight should also be applied as well. This backward weight is given by the Jacobian of the change of variable from T_0 to T_1 . The differentiation of the previous equation (75) yields

$$\left| \frac{dT_0}{dT_1} \right| = \frac{\Lambda_h(T_0)S_s(T_0)}{\Lambda_h(T_1)S_s(T_1)}. \quad (76)$$

This result is similar to the CSDA Jacobian factor given by equation (68) but with an extra vertex weight, $\Lambda_h(T_0)/\Lambda_h(T_1)$. It is thus convenient to use the following scheme for backward Monte Carlo weights:

- When the projectile is backward transported from s_1 to s_0 , its Monte Carlo weight is multiplied by $S_s(T_0)/S_s(T_1)$.
- At a backward collision vertex, the particle Monte Carlo weight is multiplied by $\Lambda_h(T_0)/\Lambda_h(T'_1)$, where T_0 (T'_1) is the energy of the particle before (after) the backward collision, i.e. $T'_1 > T_0$.

This scheme is still valid in the case that the backward transport stops before a hard collision occurs, because the particle reached a medium boundary or an external constraint, as demonstrated in Niess et al. [10] (corollary 3). Note also that in the case where there is no continuous energy loss, the previous vertex weighting is still correct. One just needs to set the backward transport weight to 1.

The weighting scheme described previously only accounts for the projectile backward transport between two hard collisions vertices. One needs to apply an additional collision backward weight at vertices, as discussed hereafter in section 3.5.

3.3. Straggled mode

In straggled mode, a class II Monte Carlo simulation is performed following PENELOPE [27], with some modifications for convenient usage in backward mode. Physics processes are split as in mixed mode, but in addition the soft electronic energy loss is fluctuated around its mean value, S_s . This implies that one cannot directly draw the position of the next hard collision as in mixed mode. Instead, one relies on the procedure described hereafter.

3.3.1. Forward straggled transport

Let s_0 and T_0 denote the initial path length and kinetic energy of the projectile. A tentative Monte Carlo step length Δs_E is set as

$$\Delta s_E = \frac{\epsilon_s}{\rho} R_s(T_0), \quad (77)$$

where ϵ_s is a configurable parameter allowing to tune the simulation accuracy. By default $\epsilon_s = 1\%$. This tentative step length is compared to other processes as detailed in [Appendix I](#). Thus, the actual step length $\Delta s = s_1 - s_0$ might be smaller than Δs_E in practice.

Using the notations of PENELOPE manual, the mean energy loss over the step and the variance are given by

$$\langle \omega \rangle = T_0 - \bar{T}_1 + \mathcal{O}(\Delta s^3), \quad (78)$$

$$\begin{aligned} \text{var}(\omega) = & \frac{\rho \Delta s}{2} (\Omega_s^2(T_0) + \Omega_s^2(\bar{T}_1)) \times \\ & \left[1 + \frac{\rho \Delta s}{\langle \omega \rangle} (S_s(\bar{T}_1) - S_s(E_0)) \right] + \mathcal{O}(\Delta s^3), \end{aligned} \quad (79)$$

where $\bar{T}_1 = R_s^{(-1)}(R_s(T_0) - \rho \Delta s)$ is the energy at s_1 assuming CSDA for soft collisions. The soft energy straggling is

$$\Omega_s^2(T) = \frac{\mathcal{N}_A}{M} \int_0^{\nu^c} \frac{d\sigma}{d\nu}(T) \nu^2 d\nu, \quad (80)$$

where only soft electronic collisions are considered, as discussed hereafter.

Equations (78) and (79) differ from the original energy corrected expressions found in PENELOPE [27]. It is shown in [Appendix G](#) that those are equivalent to PENELOPE at order 2 of Taylor expansion in the step length Δs . The present expressions are symmetric by exchange of T_0 and T_1 , which is convenient for the backward formulation of the transport.

The energy loss ω is drawn from equations (4.59) to (4.63) of the PENELOPE manual [27], using the procedure described there, and the energy T_1 at s_1 is set to $T_1 = T_0 - \omega$. Note that this procedure reproduces the correct mean and variance for the energy loss ω , i.e. equations (78) and (79). For large energy losses ($\langle \omega \rangle^2 > 9 \text{var}(\omega)$), a truncated Gaussian distribution is used. For intermediate energy losses ($3 \text{var}(\omega) < \langle \omega \rangle^2 \leq 9 \text{var}(\omega)$), a uniform distribution is used. For small energy losses ($\langle \omega \rangle^2 \leq 3 \text{var}(\omega)$), an admixture of a delta and a uniform distribution is used. The delta distribution allows for null losses with a non null probability.

Once T_0 and T_1 are known, we are left with randomising a possible hard collision over Δs . Since the soft energy loss is randomised, the mixed procedure described in section 3.2.1 (see e.g. equation (74)) is rigorously no more valid. Therefore, a rejection sampling method is used instead, following section 4.3 of the PENELOPE manual [27]. The total cross-section is regularised with a virtual “do nothing” (δ) process. Let $\Lambda_{h,0}$ and $\Lambda_{h,1}$ denote the interaction lengths for T_0 and T_1 . Let the regularised interaction length be $\Lambda_{min} = \min(\Lambda_{h,0}, \Lambda_{h,1})$. The distance to the next event is

$$\Delta s_h = -\frac{\Lambda_{min}}{\rho} \ln \xi, \quad (81)$$

where ξ is uniformly distributed over $[0, 1]$. If $\Delta s_h \leq \Delta s$, then a hard collision or a δ event occurred over the step at $s_h = s_0 + \Delta s_h \leq s_1$.

The kinetic energy T_h at s_h is determined by linear interpolation, by assuming that the ratio of the actual energy loss to the CSDA expectation, $(T_0 - T)/(T_0 - \bar{T})$, is constant over the step. Thus,

$$T_h = T_0 - \frac{T_0 - T_1}{T_0 - \bar{T}_1} (T_0 - \bar{T}_h), \quad (82)$$

where $\bar{T}_h = R_s^{(-1)}(R_s(T_0) - \rho \Delta s_h)$.

Let $\Lambda_h(T_h)$ denote the interaction length for T_h . Then, a hard collision occurs with a probability $p_H = \Lambda_{min}/\Lambda_h(T_h)$. Otherwise, a δ event occurred, in which case the event can be ignored, i.e. the projectile kinetic energy and its path length are set to T_1 and s_1 respectively.

Let us recall that only electronic collisions are considered in PUMAS, when computing the soft energy straggling Ω_s^2 . The soft energy loss due to radiative processes is thus not fluctuated. It is deterministic even in straggled mode. This is valid since at high energies where radiative processes represent the bulk of the energy loss, fluctuations are dominated by catastrophic events. These catastrophic fluctuations are efficiently rendered by the mixed algorithm, as shown in section 5.1.

However, if the energy straggling Ω_s^2 includes radiative processes, then it becomes very large at high energies, in the radiative regime. This would complicate the backward simulation as discussed below. Thus, we decided not to fluctuate soft radiative processes in PUMAS. In addition, PENELOPE’s straggling model would not be appropriate to us in this case. Indeed, in the radiative regime, since Ω_s^2 would grow very large, PENELOPE’s model would result in a significant number of Monte Carlo steps without any energy loss at all ($\langle \omega \rangle^2 \leq 3 \text{var}(\omega)$ case). Although the correct energy loss distribution would be recovered over a large enough number of steps, this behaviour does not seem natural for a high energy projectile.

3.3.2. Backward straggled transport

The backward transport procedure in straggled mode would be obtained by inverting the algorithm described previously. However, this is not possible directly because the projectile initial energy is not known a priori in a backward Monte Carlo step. This can be circumvented by using a Backward Importance Sampling (BIS) method, detailed previously in Niess et al. [10] (see corollary 1 of the latter). That is, the energy loss straggling is backward sampled from an alternative (biased) process, whose inverse is

known. Then, Monte Carlo events are weighted in order to correct for the sampling bias, as discussed below.

As biased process, in backward mode let us randomise the energy loss ω with the same procedure as in forward mode, but swapping T_0 and T_1 in the previous equations. I.e. $\langle\omega\rangle = T_1 - \bar{T}_0 \leq 0$ in the backward case, where $\bar{T}_0 = R_s^{(-1)}(R_s(T_1) + \rho\Delta s)$. Note that in the backward case

$$\Delta s_E = \frac{\epsilon_s}{\rho} R_s(T_1) > 0. \quad (83)$$

Since $R_s(T_1) < R_s(T_0)$, in backward mode one tends do do smaller steps than in forward mode.

The biased backward process described previously is a good approximation of the true reverse process as long as T_1 fluctuates closely around its CSDA expectation, \bar{T}_1 , i.e. for large enough steps or summing up several small steps. In the limit $T_1 \rightarrow \bar{T}_1$ ($T_0 \rightarrow \bar{T}_0$) equations (78) and (79) yield the same result for the forward and approximate backward procedure.

In order to correct for the biased process, in principle the projectile Monte Carlo weight must be multiplied by the ratio of the true PDF to the biased one. In addition, a Jacobian backward weight must be applied corresponding to the change of variable from T_0 to T_1 , given by the biased transform. The complete backward weighting procedure would be rather complicated considering the straggling procedure that is used in PUMAS. Thus, an approximate backward weighting is used instead.

When considering multiple steps yielding $T_1, T_2, \dots T_n$, the Jacobian of the total transform is equal to the product of the Jacobians of each step. For a large enough number of steps, we might expect T_n to be close to its CSDA expectation. Hence, for an elementary step, let us use the Jacobian obtained previously in CSDA mode, i.e. equation (68), but substituting the CSDA expectation \bar{T}_0 with the outcome of the backward procedure, T_0 . This procedure yields a backward weight satisfying to the Jacobian composition law and having the correct asymptotic behaviour for $T_0 \rightarrow \bar{T}_0$, as

$$\begin{aligned} \left| \frac{dT_0}{dT_n} \right| &= \frac{S_s(T_0)}{S_s(T_1)} \frac{S_s(T_1)}{S_s(T_2)} \dots \frac{S_s(T_{n-1})}{S_s(T_n)} \\ &= \frac{S_s(T_0)}{S_s(T_n)}. \end{aligned} \quad (84)$$

Note that if we use \bar{T}_0 for the backward weight instead of T_0 , the intermediary terms do not simplify out.

Similarly, when a hard collision occurs, let us use $\Lambda_h(T_h)/\Lambda_h(T'_1)$ as backward weight at the vertex, where T_h is the energy interpolated using equation (82), swapping T_0 and T_1 , and T'_1 the projectile energy after the backward collision.

When fluctuating only soft electronic collisions, the approximate backward procedure described previously is accurate at 0.2% for transmission muography applications, as illustrated in section 5.1. For large values of the straggling, when soft radiative losses are also fluctuated, the approximate procedure is still surprisingly accurate, to a few percent.

3.4. Multiple scattering

As for the energy loss discussed previously, most collisions are soft, resulting in a small angular deflection. However, the collective effect of multiple soft collisions can lead

to a sizeable total deflection over the projectile path length. This is efficiently taken into account with a mixed Monte Carlo algorithm, where the soft scattering is rendered by a “multiple scattering” process.

3.4.1. Transport mean free path

For small values, the multiple scattering deflection angle θ after a path length Δs is approximately Gaussian, with standard deviation

$$\sigma_\theta = \sqrt{\rho \Delta s / \lambda_{1,s}}, \quad (85)$$

where ρ is the density of the target material and $\lambda_{1,s}$ the transport mean free path restricted to soft collisions.

As can be seen from equation (85), the soft transport path $\lambda_{1,s}$ directly quantifies the magnitude of the multiple scattering. It is computed by summing up the contributions of all physics processes as

$$\frac{1}{\lambda_{1,s}} = \frac{1}{\lambda_{1,e}} + \sum_j \frac{1}{\lambda_{1,j}}, \quad (86)$$

where $\lambda_{1,e}$ is the contribution from elastic collisions and the $\lambda_{1,j}$ the contributions from all other processes restricted to soft collisions with $\nu \leq \nu_c$. The elastic contribution is given by

$$\frac{1}{\lambda_{1,e}} = 2 \frac{\mathcal{N}_A}{M} \int_0^{\mu_c} \frac{d\sigma_e}{d\mu} \mu d\mu. \quad (87)$$

Let us recall that, for elastic collisions, the angular parameter μ and the energy loss ν are directly related by the kinematics. However, since in PUMAS we neglect the energy loss in elastic collision, the soft cutoff is applied on the angular parameter μ . Following Fernández-Varea et al. [59], the value of the angular cutoff parameter, μ_c , is set such that a large enough number of hard elastic collisions occur on the projectile path. Thus, μ_c is obtained by solving

$$\Lambda_e(\mu_c) = C_e \min(\lambda_{1,e}(1), R), \quad (88)$$

where R is the CSDA range given by equation (62) and Λ_e the interaction length for hard elastic collisions, defined as

$$\frac{1}{\Lambda_e} = \frac{\mathcal{N}_A}{M} \int_{\mu_c}^1 \sigma_e d\mu. \quad (89)$$

In practice, $R \leq \lambda_{1,e}$ for muon and tau particles. Thus, the cross-section for hard elastic collisions is driven by the projectile range.

The elastic ratio C_e appearing in equation (88) is a configurable parameter. By default, it is set to $C_e = 5\%$, following Fernández-Varea et al. [59]. This results in 20 hard elastic collisions on average on the projectile full range. We did not observe any gain in accuracy by using smaller values for muography applications. However, it might be required to decrease C_e for specific applications with thin targets.

Equation (88) is solved numerically when tabulating material properties. Note that it is possible that no solution exist for $\mu_c \in [0, 1]$, e.g. for low projectile energies and/or

small values of C_e . In this case, μ_C is set to 0, i.e. all elastic collisions are simulated individually.

The non-elastic contributions to multiple scattering are given by

$$\frac{1}{\lambda_{1,j}} = 2 \frac{\mathcal{N}_A}{M} \int_0^{\nu_C} \int \frac{d^2\sigma_j}{d\nu d\mu} \mu d\mu d\nu. \quad (90)$$

For electronic collisions, the approximate result of equation (52) is used. For radiative processes, the DDCSs discussed in section 2.3 are integrated numerically with a Gaussian quadrature.

The results obtained for the soft transport path, using PUMAS default settings, are shown on figure 6, for a muon in standard rock. It can be seen that the soft part of the multiple scattering is dominated by elastic collisions up to very high energies. Above ~ 10 PeV, photonuclear interactions are the dominant source of soft scattering. It would be tempting from this figure to conclude that angular deflections in bremsstrahlung and pair production events are negligible. However, this is only true for soft collisions. At PeV energies and above, the total transport path length is actually dominated by the latter processes with catastrophic collisions, in which the projectile loses most of its initial energy.

3.4.2. Forward multiple scattering

The multiple scattering and energy loss procedures implemented in PUMAS are similar. First, the energy at which the next hard elastic collision would occur is randomised using equation (74), but substituting Λ_h with Λ_e . Then, similarly to straggled mode, Monte Carlo steps are limited to a fraction of the soft transport path, as

$$\Delta s_e = \frac{\epsilon_s}{\rho} \lambda_{1,s}. \quad (91)$$

If both energy loss and scattering are enabled, then the smaller of equation (77) or (91) is used as the Monte Carlo step length Δs . Other conditions might further limit the step length as detailed in Appendix I. E.g. if a hard elastic collision occurs over the step, then the step length is shortened accordingly. In practice, for muons and taus the step length is driven by equation (77), i.e. by the energy loss.

A soft multiple-scattering process is applied at the end of each Monte Carlo step. The soft angular parameter μ_s is randomised using equation (85) and a small angle approximation:

$$\mu_s = -\frac{\rho \Delta s}{4} \left(\frac{1}{\lambda_{1,s}(T_0)} + \frac{1}{\lambda_{1,s}(T_1)} \right) \ln \xi, \quad (92)$$

where T_0 (T_1) is the initial (final) kinetic energy over the step and ξ a random number distributed uniformly over $[0, 1]$. Note that $\lambda_{1,s}$ might vary significantly over the Monte Carlo step due to energy loss. Thus, an average estimate of the transport cross-section $1/\lambda_{1,s}$ is used in equation (92).

Once the angular parameter μ_s has been sampled the projectile momentum direction is rotated accordingly. This is done at the end step location as if a discrete collision had occurred. Note that Fernández-Varea et al. [59] instead apply the soft scattering at a random position over the step. Both procedures are asymptotically valid, i.e. they both yield correct multiple scattering distributions when considering several (~ 20 or more)

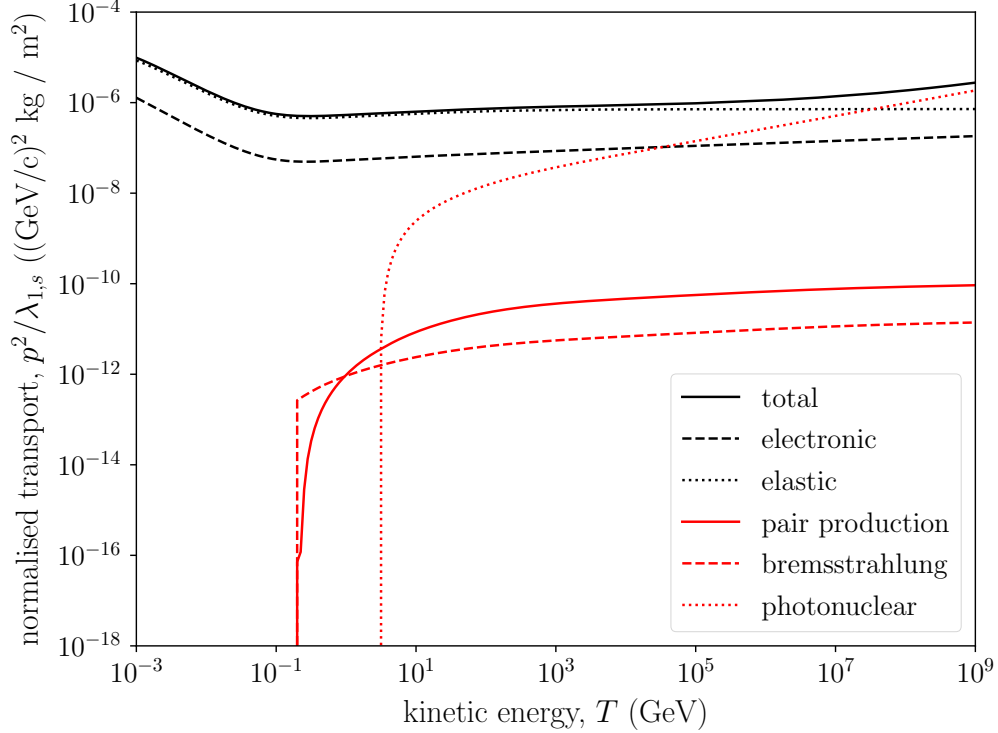


Figure 6: normalised transport cross-section, $p^2/\lambda_{1,s}$, for soft interactions. A muon in standard rock is considered. The total transport cross-section is indicated as well as the individual contributions of the different processes discussed in section 2. PUMAS default cutoff values are used, i.e. an elastic ratio of $C_e = 5\%$ and a relative cutoff of $x_C = 5\%$ on the projectile energy loss.

Monte Carlo steps. The method of Fernández-Varea et al. is however more accurate when considering only a few steps. It reproduces the correct spatial distribution over the step at leading order in the step length (see e.g. section 3 of [59]). But, as a result, soft scattering vertices are interleaved with other processes (energy loss, hard collisions, etc.) occurring at step ends. This is not convenient. Therefore, in PUMAS, the soft scattering is instead applied at end step, i.e. synchronously with other processes.

3.4.3. Backward multiple scattering

The backward simulation of the multiple scattering is almost identical to the forward one. The energy at which the next hard elastic collision would occur is sampled using equation (75) instead of (74). Otherwise, the exact same procedure as in forward mode is applied. Thus, as discussed previously for the straggled mode, backward Monte Carlo steps tend to be smaller than forward ones.

Let us recall that the energy loss is neglected in elastic collisions. Therefore, there is no transport backward weight to apply when such a collision occurs, since Λ_e is the same before and after the collision. In addition, the soft multiple scattering process applied at

the end of each Monte Carlo step is a pure rotation. The Jacobian of this transformation is unity. As a result, the backward simulation of the multiple scattering induces no additional backward weight. Only the already discussed transport weight needs to be applied for the used energy loss algorithm, i.e. equation (68) for CSDA or mixed mode or its equivalent approximation in straggled mode.

3.5. Hard collisions

When a hard collision occurs, an interaction with an individual atom of the target medium is explicitly simulated. This is done in two steps. First the energy loss ν of the projectile is randomised. For this step a different algorithm is used in forward and in backward mode. Second, if scattering is enabled, then the angular parameter μ is randomised according to the DDCS, given the randomised energy loss ν .

In the case of an elastic collision, the energy loss is approximated by zero. The first step is thus skipped, and one directly randomises the angular parameter μ of the collision from the elastic DCS.

3.5.1. Forward collision

In forward mode, first the target atom and the interaction process are randomised using the classical procedure. The probability p_{ij} that the hard collision occurs on the i^{th} atom with the j^{th} physics process is given by the ratio of interactions lengths, as

$$p_{ij} = \frac{\Lambda_h(T)}{\Lambda_{ij}(T)}, \quad (93)$$

where Λ_h is given by equation (71) and where Λ_{ij} is the summand in the latter, i.e. the interaction length for i and j .

Once the target atom and the physics process have been determined, the energy loss ν is randomised by rejection sampling. The efficiency of this method depends critically on the DCS bounding envelope that is used. In the case of electronic collisions, a simple yet efficient envelope is provided by keeping only positive terms in the DCS given by equation (70). The latter envelope can be randomised with the inverse CDF method.

For radiative processes, the DCS expressions are more complex and numeric methods are used. In previous versions of PUMAS, a Zigurat like envelope was used for projectile energies above 10 GeV. This method requires the restricted DCS for hard collisions to be monotone. It was satisfied for projectile energies larger than 10 GeV with a fixed (hard-coded) relative cutoff of $x_c = 5\%$. Below 10 GeV, a weighted procedure was used as described in Niess et al. [10]. Since PUMAS v1.1 the relative cutoff between soft and hard collisions can be varied. Consequently the restricted DCS is not guaranteed to be monotone. Thus, the Zigurat method is no longer valid. It has been replaced by a power law envelope described in Appendix H. The new procedure typically requires 1 or 2 evaluations of the DCS per hard collision, and it is valid over all projectile energies. Thus, since PUMAS v1.1 the Monte Carlo particle states are no longer weighted in forward mode, except possibly from the decay probability as discussed in section 3.6.

At high energies w.r.t. the critical energy, hard collisions are frequent even with the high relative cutoff $x_c = 5\%$ used by default in PUMAS. Then, a single computation of the DCS for a radiative process is already expensive CPU-wise. Therefore, a cubic spline interpolation is used instead for radiative DCSs, as described in Appendix F.

The spline parameters are tabulated at PUMAS initialisation. The spline grid is set in order to achieve a better than 0.1% relative accuracy on the DCS. However, close to kinematic boundaries the DCSs can vary sharply, which would require a very dense grid for the spline. These boundary regions are thus removed from the spline interpolation and an exact computation is used instead. Note that those cases are rare. Thus, it is not expensive CPU-wise to perform a full computation when they occur.

Let us point out that the procedure used in PUMAS for the sampling of the energy loss in hard collisions differs from what is traditionally done. Usually, the inverse CDF method is used instead of rejection sampling. We do not use the former for two reasons. First, the backward sampling described hereafter also requires the DCS not the CDF. Thus, an extra tabulation would be required if using the inverse CDF method. Secondly, accurately tabulating the CDF close to kinematic boundaries could be numerically difficult. With the rejection sampling method this is avoided by using the exact DCS in those cases.

3.5.2. Backward collision

In backward mode, the projectile energy before the collision is not known a priori. Thus, the rejection sampling method described previously cannot be used. Instead, a BIS procedure is used as previously for the energy loss straggling (see section 3.3.2). First, the initial kinetic energy T is randomised from a biased distribution. Let us consider a biased process whose DCS is given by a power law function of exponent $\alpha > 1$. Let its normalized DCS be given by

$$p_b(\nu; T) = \begin{cases} \frac{1}{T} \frac{(\alpha-1)x_C^{\alpha-1}}{1-x_C^{\alpha-1}} \frac{1}{x^\alpha} & \text{if } x \in [x_C, 1] \\ 0 & \text{otherwise} \end{cases}, \quad (94)$$

where $x = \nu/T$ and where $x_C = \nu_C/T$ is the relative cutoff for hard collisions. In order to properly apply the BIS procedure, one needs to consider the mathematical support of the true and biased DCSs, as real-valued functions of ν . In this case, the support of the biased DCS is bounded from below by the cutoff for hard collisions and from above by the kinetic energy. In practice, the true DCS has a smaller support, included into the biased DCS one. This is correct for the biasing procedure, the only downside being that the BIS procedure might result in null Monte Carlo weights. The converse would be wrong however, i.e. if the biased DCS would take null values on the support of the true DCS. Then, the BIS procedure would be biased, since it would miss the corresponding cases.

The value set for α significantly impacts backward Monte Carlo results, especially when backward transporting muons over large distances ($\gtrsim 3$ km of standard rock). In PUMAS v1.2, $\alpha = 2$ is used, which fits the total radiative DCS within 5% for $x \in [0.6, 7]$ %. Previously, a value of $\alpha = 1.4$ was preferred (see [10]). However, the validation procedure described in section 5.1, indicates that the latter value is less efficient. The updated value ($\alpha = 2$) results in lower variance over all distances, and it is numerically more robust. Thus, it must be concluded that the previous estimate of $\alpha = 1.4$ was inaccurate.

For very small cutoff values ($x_C \lesssim 0.1\%$) and large distances, the backward collision method described below is numerically unstable, whatever the selected value of α . Therefore, in mixed or straggled backward modes, PUMAS prevents using a cutoff value

lower than 1%. This is not expected to be a limitation for most muography applications, as shown in section 5.1.

The fractional energy loss x for the biased process can be sampled semi-analytically with the inverse CDF method:

$$x = x_c [1 - \xi (1 - x_c^{\alpha-1})]^{1/\alpha}, \quad (95)$$

where ξ is a random number uniformly distributed over $[0, 1]$. Conversely, equation (95) can be solved for the initial kinetic energy T by substituting $x = 1 - T'/T$. Thus, the initial kinetic energy is backward sampled as

$$T = \frac{T'}{1 - x_c [1 - \xi (1 - x_c^{\alpha-1})]^{1/\alpha}}. \quad (96)$$

Let us point out that the backward weight for the biased DCS is

$$\frac{dT}{dT'} = \frac{T}{T'}. \quad (97)$$

Once the initial energy has been backward sampled, the target atom and the physics process can be randomised. This is done with a biased distribution as well. For this purpose, it is convenient to consider the macroscopic cross-section, $\Sigma_h = 1/\Lambda_h$, instead of the interaction length. The probability to select the i^{th} atom and the j^{th} process is set to

$$p_{ij} = \frac{d\Sigma_{ij}}{d\nu}(T, T - T') \bigg/ \frac{d\Sigma_h}{d\nu}(T, T - T'). \quad (98)$$

Note that for the true distribution, p_{ij} is proportional to the macroscopic cross-section Σ_{ij} instead of the DCS, see previous equation (93). However, since both the initial and the final energies are known at this stage, we prefer to use the DCS. This choice is justified hereafter.

The backward sampling method requires applying a collision backward weight, ω_c , in addition to the transport backward weight discussed previously, e.g. given by equation (76). A detailed proof is provided in Niess et al. [10] (see e.g. corollary 3 and equation (15) of the latter). For the procedure described herein, the collision backward weight is given by

$$\omega_c = \frac{\Lambda_h(T)T}{p_b(T - T', T)T'} \frac{d\Sigma_h}{d\nu}(T, T - T'). \quad (99)$$

Note that the collision backward weight does not depend on the selected target atom and physics process. This is due to the choice of randomising those according to the DCSs instead of the cross-sections. Consequently, the dispersion of backward weights is reduced with the biased target selection. In addition, since we do not simulate secondary particles, the target selection step might be skipped when scattering is disabled.

In principle, the collision backward weight can be null if the kinematics does not match the DCS support of any physics process. This almost never occurs in practice. Still, whenever a backward collision results in a null weight, the backward transport stops and the corresponding event can be dropped. Nevertheless, one should not silently discard these events. They must be counted when computing the Monte Carlo estimate

(average), otherwise the result would be biased. In order to make this point clear, let us denote N_{gen} the total number of generated Monte Carlo events, among which $n_0 \leq N_{\text{gen}}$ have a null weight. Then, one must normalise the Monte Carlo estimate by N_{gen} , not by $N_{\text{gen}} - n_0$.

An additional technical difficulty arises from the fact that the total cross-section for hard collisions is null at low energies, below a value E_0 . This breaks the symmetry between forward and backward collisions, since a backward collision could occur at any energy, but a forward one only for $E > E_0$. This problem is solved by adding a δ -process (“do nothing”) in order to regularize the total cross-section. More details on this can be found in Niess et al. [10], e.g. in section 3.3 of the latter.

3.5.3. Scattering angle

The method used for the randomisation of the scattering angle in a hard collision depends on the physics process. For electronic collisions, the effective model discussed in section 3.2 only considers close interactions. The corresponding scattering angle is directly computed from equation (47). For other processes, rejection sampling is used.

For elastic collisions, the scattering angle is randomised in the CM frame, and then it is transformed back to the laboratory frame. The exact DCS, as well as its envelope, are computed as explained in Appendix D.

For bremsstrahlung and e^+e^- pair production, the Tsai [55] DDCCS is used as discussed previously in section 2.3. An upper bound is given by considering only the first (positive) term in equation (55) and substituting $X(\mu)$ with $X(0)$ since $X(\mu) \leq X(0)$ for all $\mu \in [0, 1]$. Thus,

$$\frac{d^2\sigma_T}{d\nu d\mu} \leq \frac{2\alpha r_e^2}{\nu} X(0) (2 - 2y + y^2) \frac{\mu_0}{(\mu_0 + \mu)^2}. \quad (100)$$

The latter function is used as envelope for the rejection sampling of the angular parameter μ .

For photonuclear interactions, the exact DDCCS is used when available. Otherwise, the DRSS one is used, rescaled as discussed in section 2.3. The squared four momentum transfer Q^2 is sampled, and then the scattering angle is computed from equation (59). As envelope for the rejection sampling, a $1/Q^2$ law is used:

$$\frac{d^2\sigma}{d\nu dQ^2} \leq \sup_{Q^2} \left[Q^2 \frac{d^2\sigma}{d\nu dQ^2} \right] \frac{1}{Q^2}. \quad (101)$$

The maximum is determined numerically using Brent’s algorithm. Note that the latter is done on the fly during the course of the simulation. This might look very expensive CPU-wise. However, when scattering is enabled the number of Monte Carlo steps per track is large and so is the associated CPU cost. As a result, with PUMAS default relative cutoff of $x_C = 5\%$ we observe no significant slow down from the simulation of the scattering in hard photonuclear collisions, even at PeV energies.

In forward and backward modes, the same algorithm is used for simulating the scattering of hard collisions. Since this transform is a rotation, its Jacobian is 1. Thus, no extra backward weight arises from this step.

3.6. Decays

Muon and tau decays are not explicitly simulated by PUMAS. However, the proper time t of the projectile is computed over the course of the simulation. Thus, the reduction of the flux due to decays can be accounted for. PUMAS proposes two methods for this, “weighted” or ‘randomised’, described hereafter. In addition, decays can also be totally disabled.

3.6.1. Proper time

In PUMAS, the trajectory of a transported particle is approximated by a succession of line segments connected by vertices. The vertices correspond to hard collisions or to Monte Carlo steps end points. Between two vertices, the energy is assumed to vary continuously, even in straggled mode. The proper time variation between two successive vertices of index i and $i + 1$ is given by

$$t_{i+1} - t_i = \int_{s_i}^{s_{i+1}} \frac{m}{p_{i,i+1}(s)} ds, \quad (102)$$

where $p_{i,i+1}$ is the momentum of the projectile when going from s_i to s_{i+1} , varying continuously. At hard collision vertices, the particle energy changes discontinuously. Since hard collisions are considered as point-like, no proper time is needed for those. Thus, the total proper time variation is obtained by summing up the contributions of all “soft” segments, over which the projectile momentum varies continuously.

In CSDA or in mixed mode, the proper time elapsed between two hard collisions depends only on the kinetic energy at end points. It is given by

$$\rho(t_{i+1} - t_i) = R_t(T_i) - R_t(T_{i+1}), \quad (103)$$

where R_t is the proper time range defined as

$$R_t(T) = \int_0^T \frac{dT'}{\beta' \gamma' S(T')}. \quad (104)$$

Note that a uniform medium is assumed as discussed previously, e.g. in section 3.1. Note also that, in mixed mode, the total stopping power S must be replaced with the soft one, S_s , in equation (104).

In straggled mode, the proper time is integrated over Monte-Carlo steps using trapezoidal rule. Thus,

$$\rho(t_{i+1} - t_i) = \left(\frac{1}{p_{i+1}} + \frac{1}{p_i} \right) \frac{m(s_{i+1} - s_i)}{2}, \quad (105)$$

where p_i (p_{i+1}) is the projectile initial (final) momentum for the Monte Carlo step.

The proper time is identical in backward and in forward modes. But, in backward mode, the proper time integration proceeds in reverse order, i.e. from the target to the source.

3.6.2. Weighted mode

The weighted mode accounts for decays globally by weighting Monte Carlo states by the survival probability for decays, P_s . This is possible since the survival probability P_s depends only on the total elapsed proper time, $t_1 - t_0 \geq 0$, as

$$P_s(t_0, t_1) = e^{-(t_1 - t_0)/\tau_0}, \quad (106)$$

where t_0 (t_1) is the initial (final) proper time and τ_0 the projectile proper lifetime.

The weighting method does not depend on the direction of the Monte Carlo flow, i.e. forward or backward sampling. However, a time reference must be defined in both cases. In forward mode, it seems natural for the user to specify t_0 at input of the transport procedure, and to get $t_1 \geq t_0$ at output. In backward mode, it would be tempting to instead specify t_1 , and to decrease the proper time in order to deliver t_0 at output of the transport. This would be valid as well, but considering the final state as time reference. Nevertheless, this could be error prone. Let us elaborate more on this point.

A common confusion is to identify backward transport with time reversal, in the sense that it would “rewind” the Monte Carlo as a movie. This would be the case if collision physics was deterministic. But, except when using deterministic approximations, the like CSDA, it is not. Let us consider the example of a point source in order to illustrate this case. Backward transporting particles originating from a point source does not focus them back onto the source, despite collisions are reverse sampled. Instead, the backward transported particles would be spread around the point source. This is contrary to the time rewinding picture described above, showing that this picture is not correct. Indeed, forward and backward Monte Carlo both generate stochastic trajectories according to the collision physics. However, while in forward Monte Carlo one specifies the initial state of a trajectory, backward Monte Carlo let us specify its final state. This is achieved by biasing and weighting. Therefore, backward Monte Carlo should actually be recognised as a particular Importance Sampling (IS) method.

Fixing t_1 and decreasing the proper time, in backward mode, would contribute to propagate the erroneous belief that backward transport would time rewind the Monte Carlo. Therefore, it was decided to use the same time reference in forward and backward modes in PUMAS. Thus, in a backward transport, one actually specifies the initial time t_0 , and then one gets the final time t_1 from the transport routine. In practice, this implies that the reported proper time can only increase, in both forward and backward modes.

For muons, the weighting method is the default algorithm in order to account for decays. Muons have a large lifetime compared to their interaction length. Therefore, it is usually more instructive to weight Monte Carlo events rather than dropping some of them. On the contrary, taus have a short lifetime. As a result, the weighting method becomes highly inefficient as the tau energy decreases. Thus, PUMAS actually forbids weighting for forward taus. By default, taus decays are randomised as explained hereafter.

3.6.3. Randomised mode

The second way to account for decays in PUMAS is by Monte Carlo. At the beginning of the transport, the proper time of the decay is drawn from equation (106) using the inverse CDF method, as

$$t_d = t_0 - \tau_0 \ln \xi, \quad (107)$$

where ξ is a random number distributed uniformly over $[0, 1]$. If the projectile proper time reaches t_d , then the transport stops and the Monte Carlo state is flagged as “decayed”.

In backward mode, “randomising decays” can be understood in different ways. The most comprehensive one would be to generate decay vertices of muons or taus over a volume of interest, and to do a backward transport from there on. This is what is done in the DANTON Monte-Carlo [61]. However, this is not what is relevant for muography. In muography, one is interested in surviving muons not in their decay products. In this case, it is enough to randomise over the survival probability P_s of a backward transported particle. Considering the proper time reference used in PUMAS, this is done with the exact same algorithm as in forward mode. It is correct because when the proper time t of the backward projectile exceeds t_d on its course from s_1 to s_0 , then $t_1 \geq t \geq t_d$ as well. However, with this backward procedure the stopping point does not represent the decay vertex. When a backward state is flagged as decayed, it must be understood that it actually did not reach the final position s_1 , but instead decayed at an unknown location before.

4. Miscellaneous

In the present section we discuss miscellaneous features of PUMAS not covered by the previous sections.

4.1. Composite materials

A type of material frequently encountered in muography applications is “rocks”. A rock is an aggregate of minerals, e.g quartz, calcite, dolomite, etc. The typical grain size of these minerals is of order 0.1-1 mm. Though, large variations can be observed in the grain size. In addition rocks are porous. Pores also have millimetric size. They can be filled with a gas e.g. air and/or a liquid e.g. water.

A mineral has a well defined atomic and electronic structure. Minerals correspond to the definition that has been used so far for materials in PUMAS. On the contrary rocks do not. As a particle traverses a rock, it crosses different mineral grains each of which has its specific dielectric response, hence density effect. Minerals are large enough such that most individual electronic collisions can be approximated as occurring inside a material of infinite extension. However, at the boundary between two minerals transition radiations occur. The latter are beyond the scope of this work, and they are neglected in PUMAS.

On the other hand, the minerals size is small w.r.t. the typical range of atmospheric muons in rocks. E.g. a 1 GeV muon has a range of 2 m in standard rock. When the projectile range is much larger than the minerals grains size, the stopping power of a rock, S_c , can be approximated by the weighted sum of its minerals ones, S_k , as:

$$S_c = \sum_k w_k S_k, \quad (108)$$

where w_k is the mass fraction of the k^{th} mineral.

In PUMAS, materials such as rocks are modelled as “composite” materials. A composite material is defined as a macroscopic mixture of “base” material. It is specified by the mass fractions, w_k , of its base materials components. A base material has been

discussed in previous sections. It is an atomic mixture of elements together with an electronic structure. In practice, the electronic structure is defined from the atomic elements mixture as discussed in section 2.2.

The density, ρ_c , of a composite material depends on the densities, ρ_k , of its parts as:

$$\frac{1}{\rho_c} = \sum_k \frac{w_k}{\rho_k}. \quad (109)$$

The stopping power of a composite is given by equation (108). Similar rules are derived for other macroscopic properties, e.g. the transport cross-section, $1/\lambda_1$, or the energy straggling, Ω^2 . For hard collisions, the composite behaves as a mixture of atomic elements, i.e. identically to a base material.

The impact of rock composition on the accuracy of muography measurements has been studied by Lechmann et al. [62]. Variations of several percent are reported depending on the mineral content and on the rock depth. However, let us point out that while Lechmann et al. consider the same definition of rocks stopping power as us (i.e. equation (108)), they use the approximate parametrisation of Sternheimer and Peierls [63] for the density effect. As a result, their electronic stopping power might differ by $\sim 1\%$ with PUMAS (see e.g. section 2.2.4 and [63]).

4.2. Bulk density

In section 3, we considered a target material with a constant composition and density. This was required in order that the stopping power does not depend on the particle location. However, there are cases where the previous assumption(s) can be relaxed while preserving an (approximately) constant mass stopping power. Then, the transport algorithms discussed in section 3 have simple generalizations. Thus, PUMAS allows users to override the default material density, ρ_0 , with a bulk (effective) value, $\rho(s)$, depending on the projectile location, s . In order to motivate the present discussion, let us first present two particular use cases for this. Then, we discuss the general case and its implementation in PUMAS.

4.2.1. Porous material

Let us consider a composite material made of $n - 1$ solids and of a gas. This could be for example a porous rock made of several minerals and filled with air. The gas density, ρ_n , is much lower than solids ones, ρ_k , typically by 3 orders of magnitude. Thus its mass fraction, w_n , is negligible w.r.t. others. However, the gas might occupy a large fraction of the composite volume, such that the bulk density of the composite, ρ_c , is significantly lower than the ones of its solids components, ρ_k .

Let us further assume that the relative composition of solids components is constant. Then, neglecting the gas contribution, the mass stopping power of the composite, S_c , is approximately constant as can be seen from equation (108). However, the bulk density (porosity) of the composite material can vary spatially. Thus, instead of considering a composite of solids and gas, it is equivalent to consider a material made only of solids, but with a bulk density reflecting porosity. Note that the material can be a base material as well, e.g. standard rock, not necessarily a composite. Let us also point out that due to the density effect correction, δ_F , this bulk density approach differs from a material whose mineral density would be set lower.

4.2.2. Gas material

A second use case is a pure gas material. The density of a gas is variable, e.g. with temperature and pressure conditions. Due to the density effect correction, δ_F , an accurate computation of the gas mass stopping power would require to take its density variations into account. However, the variations of δ_F are usually a second order correction to the projectile energy loss in comparison to the density variation itself. Let us consider Earth's atmosphere as a practical illustration. The air density decreases by a factor of 3 between sea level and an altitude of 10 km. In comparison, the mass stopping power varies at most by 2% over the same range.

In addition, for similar path lengths the projectile energy loss in gas is negligible in comparison to the one in liquids and solids, due to the large density difference. Thus, depending on the geometry of the simulation one might simply neglect the density effect corrections for gases and use an average density value. However, density variations are mostly taken into account by using a local density value that might differ from the one used for computing the gas mass stopping power.

For projectiles with energy much larger than the critical energy, the contribution of electronic collisions to the stopping power is negligible. Thus, the density effect can be neglected at high energy. However, in the radiative regime the stopping power depends strongly on the target atomic content as $\sim Z^2/A$. Provided that the material composition is constant, at high energy the stopping power per unit mass would be approximately independent of the material density. In practice, having a constant composition but variable density seldom happens, apart from the two cases discussed previously, i.e. for a gas material like Earth's atmosphere or, approximately, for a porous rock with a uniform mineral content.

4.2.3. General case

Let us assume that the mass stopping power is constant, but that the local target density depends on the location s along the projectile path. Let X denote the column density along the path s , as:

$$X = \int_0^s \rho(s') ds'. \quad (110)$$

For a constant mass stopping power, the CSDA range defined by equation (62) only depends on the projectile energy not on its location. Thus, equation (61) can be generalized as:

$$X_1 - X_0 = R(T_0) - R(T_1). \quad (111)$$

For a constant mass stopping power, assuming CSDA, the column density and the particle kinetic energy are related independently of the details of the density distribution of the target medium. Therefore, the CSDA transport equations of section 3.1 can be generalized as well by substituting X for ρs . The relation between the particle location, s , and X is given by the previous equation (110). It is a priori complex for an arbitrary density distribution.

The cross-sections for hard collisions do not depend on the target density. Thus, the mixed algorithm discussed in sections 3.2 and 3.4 is unchanged. The average number of hard collisions, N_h , depends only on the projectile initial energy or equivalently on the column density, X . The expressions for the soft multiple scattering and for the straggled energy loss can be generalized as well by substituting X for ρs , as for the CSDA mode.

E.g. in equation (81) the column density to the next hard collision, ΔX_h , is randomised instead of $\rho\Delta s_h$.

In addition, the Monte Carlo stepping algorithm requires some modifications when letting the density vary. The local density value is provided by the user with a callback function. This function must also indicate the typical length, L_ρ , over which the density varies. For example, for a density gradient, $\vec{\nabla}\rho$, it would return:

$$L_\rho = \frac{\rho}{|\vec{\nabla}\rho \cdot \vec{u}|}, \quad (112)$$

where \vec{u} is the momentum direction of the projectile. Then, the Monte Carlo local step length is defined as

$$\Delta s_l = \epsilon_s L_\rho, \quad (113)$$

where ϵ_s a configurable parameter allowing to tune the accuracy of the simulation. This local step length is compared to other conditions, as detailed in [Appendix I](#), leading to an actual Monte Carlo step $\Delta s \leq \Delta s_l$.

The column density over a Monte Carlo step, ΔX , is computed with the trapezoidal rule from the local density values, ρ_0 and ρ_1 , at the beginning and end of the step. Thus,

$$\Delta X = \frac{\rho_0 + \rho_1}{2} \Delta s. \quad (114)$$

If a hard collision occurs over the step at a column density $\Delta X_h < \Delta X$, then its location is interpolated by assuming that the density varies linearly over the step. Note that this assumption is consistent with the trapezoidal rule used in equation (114).

The stepping algorithm used in PUMAS relies on the assumption that the local density variations of the material are continuous. If this is not the case, then different propagation media should be used instead, as described in [section 4.4](#).

4.3. Magnetic field

PUMAS allows an external magnetic field to be supplied. However, electric fields are not supported, as in PUMAS v1.2.

Magnetic fields are defined, by the user, with the same callback as for local density models, discussed in previous [section 4.2](#). If the magnetic field is not uniform, then the user must indicate the typical length over which it varies. As for the density model, the variations are expected to be continuous. If this is not the case, then different media should be used. If both a variable local density and a variable magnetic field are used, then the smallest of both variation lengths should be returned.

The interaction with the external magnetic field \vec{B} is treated using a classical formalism. Magnetic fields are assumed to be weak enough such that synchrotron radiation can be neglected. This is for example valid for a muon evolving in Earth's geomagnetic field. For a point-like particle of electric charge $q = ze$, the relativistic equation of motion writes

$$\frac{d\vec{u}}{ds} = \frac{ze}{p} \vec{u} \times \vec{B} \quad (115)$$

where \vec{u} is the momentum direction. Note that $e \simeq 0.2998 \text{ GeV}/c\text{T}^{-1} \text{m}^{-1}$, which is convenient when p is expressed in GeV/c and B in Tesla.

The classical magnetic deflection conserves the particle energy. However, the projectile loses energy over its path due to collisions. In addition, the magnetic field might vary over the path. In order to take these effects into account, the equation of motion is discretized over Monte Carlo steps. In practice, the method used in PUMAS is equivalent to modelling the interaction with the external magnetic field as an additional, and independent, scattering process. It is similar to the soft multiple scattering, i.e. it is applied at end-step (see section 3.4), but a deterministic deflection angle is used, derived from the equation of motion (115).

The update rule is derived from finite differences of the equation of motion. Let \vec{u}_0 denote the initial momentum direction of the projectile and p_0 its absolute value. Let \vec{B}_0 denote the magnetic field at the step starting location. Then, at the end of the Monte Carlo step, the projectile momentum direction would be updated as

$$\vec{u}_1 = \vec{u}_0 + \frac{ze\Delta s}{2} \vec{u}_0 \times \left(\frac{\vec{B}_0}{p_0} + \frac{\vec{B}_1}{p_1} \right) \quad (116)$$

where p_1 and B_1 are the projectile momentum and the magnetic field at the end of the Monte Carlo step. Let us recall that the projectile follows a straight line trajectory over the step, along \vec{u}_0 . Its direction is only modified at the end of the Monte Carlo step.

The previous update rule does not properly conserve the norm of the momentum direction, \vec{u} . This could be solved by re-normalising the direction after each update. An alternative solution is to instead use the following update rule, equivalent at leading order in Δs to equation (116). In order to simplify the notations let us first define:

$$\vec{\ell}_{0,1} = \vec{u}_0 \times \left(\frac{\vec{B}_0}{p_0} + \frac{\vec{B}_1}{p_1} \right). \quad (117)$$

Then, the update rule, used in PUMAS, for magnetic deflection is

$$\vec{u}_1 = \cos\left(\frac{\Delta s}{r_B}\right) \vec{u}_0 + \sin\left(\frac{\Delta s}{r_B}\right) \vec{u}_\perp \quad (118)$$

with

$$\frac{1}{r_B} = \frac{ze}{2} |\vec{\ell}_{0,1}| \quad (119)$$

and

$$\vec{u}_\perp = \vec{\ell}_{0,1} / |\vec{\ell}_{0,1}|. \quad (120)$$

Equation (118) conserves the norm of \vec{u} since $\{\vec{u}_0, \vec{u}_\perp\}$ forms an orthonormal basis.

In order for the finite difference method to be accurate, the Monte Carlo step length Δs must be small w.r.t. the magnetic bending radius. Thus, when a magnetic field is defined, the Monte Carlo step length is limited by $\Delta s \leq \Delta s_B$ with:

$$\Delta s_B = \frac{\epsilon_s p_0}{ze |\vec{u}_0 \times \vec{B}_0|} \quad (121)$$

where ϵ_s is a configurable parameter allowing to tune the accuracy of the simulation.

In the case of a uniform magnetic field, a muon would follow a circular (helix) trajectory in the void. Instead, PUMAS approximate this trajectory with line segments. The relative difference on the path length, between both trajectories, is of $\mathcal{O}(\Delta s^2/r_B^2)$. It is assumed that $\epsilon_S \lesssim 1\%$. Thus, the path length difference would be negligible, and no additional correction is applied in PUMAS.

In backward Monte Carlo mode, the same algorithm is used for magnetic deflections as in forward mode. The backward update rule is obtained by swapping \vec{u}_0 and \vec{u}_1 , as well as other quantities in equation (118). In addition, one must take care that the magnetic deflection is reversed since the projectile propagates along $-\vec{u}_1$. This can be accounted for by changing the sign of the deflection angle $\Delta s/r_B$, in equation (118). Note also that, since the magnetic deflection is a pure rotation, the corresponding backward weight is unity.

A typical use case of magnetic field in PUMAS is the deflection of low energy muons by Earth’s geomagnetic field, as they travel through the atmosphere. Let us point out that Earth’s geomagnetic field is too weak to significantly deflect muon or tau leptons in dense materials, like rocks or water. In the latter case, the projectile range is much lower than the magnetic bending radius, over all energies. Thus, as an optimisation, the geomagnetic field can be deactivated in dense materials without loss of accuracy.

4.4. Geometry

So far, we considered a single target material potentially with continuous bulk density variations. However, in a practical muography use case the projectile would traverse different materials, e.g. air and rocks. Modelling this requires a geometry description. The PUMAS library does not include a geometry engine with primitive shapes and related functions, such as ray tracers. Instead, the geometry must be supplied by the user with a callback. Nevertheless, this generic mechanism allows one interfacing PUMAS with external geometry engines. The PUMAS website [11] provides examples of interfaces with Geant4 [64–66], using a G4Navigator, or with the TURTLE library [67]. In principle, PUMAS could also be interfaced with ROOT [68] using a TGeo object. However, at the time of this writing we are not aware of any publicly available example of this.

Let us briefly describe the generic geometry representation used in PUMAS. Let us define a propagation medium as a material with possibly a local density model. If no local density is provided, then the material density is assumed for the medium. The geometry of the simulation is supplied by the user as a “medium” callback function. This function gets as input the projectile location, \vec{r} , and its momentum direction, \vec{u} . In return, it is expected to indicate the corresponding medium at \vec{r} and the distance Δs_m to the medium boundary, assuming a straight line propagation. Let us recall that in backward mode the projectile propagates along $-\vec{u}$ instead of \vec{u} . Note also that on some calls both Δs_m and the medium are required, while in other calls only one of those is expected. This is indicated to the user by passing a null pointer when the corresponding information is not needed by PUMAS. Additional technical details are given in [Appendix I](#).

4.5. Software

The present document focuses on the physics used in PUMAS and on its implementation. However, some particular software aspects of PUMAS deserve attention as well. Those are discussed below.

The PUMAS library has been implemented in C99 with the C standard library as sole external dependency. It is LGPL-3.0 licensed. The PUMAS source is 12 k Lines Of Code (LOC) in total. It is contained in two files `pumas.c` and `pumas.h`. Thus, PUMAS can easily be embedded in any software project compatible with the C Application Binary Interface (ABI), e.g. in C++ or Python.

Examples of installation of PUMAS are given on the website [11]. On Linux and OSX, an example of `Makefile` is available for compiling PUMAS with `Make`. However, since PUMAS is standard C we do not expect any specific difficulty for compiling it. PUMAS can also be installed with `CMake` using the provided `CMakeLists.txt` file. This has been tested on Linux, OSX and Windows.

The PUMAS library uses a single namespace. All publicly exported enums, functions, macros and structs are prefixed with `pumas_` or `PUMAS_`.

The library design follows an object oriented pattern with three main C struct objects: `pumas_context`, `pumas_physics` and `pumas_state`. These objects correspond to specific memory usages, detailed hereafter.

The `pumas_physics` object is the first that needs to be instantiated. A physics instance is specific to one type of particle, i.e. muon or tau. It is an opaque C struct that contains the tabulations needed during the Monte Carlo transport. These tables are computed when instantiating the physics. Then, they are readonly at runtime. The initial computation of the physics tables can take tens of seconds to a few minutes, depending on the number of defined materials. This can be problematic in some use cases. For faster initialisation, the physics tables can be dumped to disk and loaded back as well. Note that the raw content of the C struct is written to disk. Therefore, this format is not portable.

The materials to tabulate are defined in a specific XML file called Materials Description File (MDF). The user must supply this file. It specifies the properties of atomic elements, of base materials and of composite materials, used during the simulation. Examples of MDF are available from the PUMAS website [11]. The tabulation generates stopping power text files in the PDG format. These files can be browsed as a cross-check. They can also be overridden in order to rescale PUMAS stopping power to a different model.

The `pumas_context` object manages a simulation stream for a given physics object. It contains configuration parameters for the simulation, which the user can set directly, e.g. the energy loss mode, the transport direction, etc. Limits can be set on the projectile properties as well, e.g. on its travelled path length or on its kinetic energy. In addition, this object manages a set of opaque data needed during the Monte Carlo transport. These data are thread specific. For multithreaded applications one `pumas_context` must be created per thread. The simulation context is forwarded to user callbacks e.g. for local models or for the geometry. Extra user memory can be reserved when instantiating the context object. As for the context data, this user memory is intended to be thread specific.

The `pumas_state` object contains a minimal set of data needed by PUMAS for describing the Monte Carlo state of a transported particle. Those data are the particle charge, its kinetic energy, its position, etc. A PUMAS state is both read and written by the user. For example it is initialised by the user before the transport. Then, the transport routine updates the state and the result is read back by the user. A state structure can be extended by the user, as long as the extension can be cast back to a

`pumas_state`. Depending on the use case, this can be more convenient than reserving extra user memory for the simulation context.

In addition to these three structures, a geometry must be defined by the user. This is done by providing a medium callback to the simulation context, as described in section 4.4. This callback points to the current propagation medium. Propagation media are defined as `pumas_medium` structures. A propagation medium is specified by a material of constant composition and an optional `pumas_locals_cb` callback. The latter allows the user to specify local values of the bulk density, or of the magnetic field, over the medium. If not provided, then the filling material density is used. As for a PUMAS state struct, the media can be extended by the user, as long as the extension can be cast back to a `pumas_medium`.

5. Validation

The PUMAS library has been continuously validated since its initial implementation. The source code is unit tested with a coverage of 91% of LOC for v1.2. The library results are validated on each update with various tests. Still, PUMAS is software. If malfunctioning is observed, these issues can be reported on the PUMAS website [11]. Let us also point out that, although PUMAS can run on Windows and OSX systems, it is developed, tested and mainly used on Linux.

PUMAS physics results have been compared to other Monte Carlo codes showing consistent results. For example PUMAS was compared to Geant4 [64–66] and MUM [57] in Niess et al. [10]. In the following, we provide an updated validation test for a transmission muography problem. In particular, we performed a comparison to PROPOSAL [5, 6]. In addition, we also consider scattering applications with two new cases: a comparison to experimental muon scattering data, and a background estimate with a toy geometry of volcano.

The validation results presented in this section were obtained with v1.1 of PUMAS for default settings ($x_c = 5\%$), and with v1.2 in other cases. The main difference between both version is an improvement in the sampling of backward collisions (see section 3.5.2). It has been checked that v1.1 and v1.2 yield consistent results when using PUMAS default settings.

5.1. Transmission muography

Let us consider a toy transmission muography problem similar to Niess et al. [10], but using updated inputs and software. Let us compute the flux of atmospheric muons Φ_1 transmitted through a given thickness d of standard rock. Let us recall that current muographs cannot measure the energy of detected particles. Thus, only the total flux is observed, not the differential one, ϕ_1 , w.r.t. the energy. As initial differential spectrum ϕ_0 , let us input the sea level parametrisation of Guan et al. [69] at an observation angle of 20 deg w.r.t. the horizon. The latter parametrization was fitted to a compilation of experimental data. Contrary to Gaisser’s parametrization [31, 70] used previously in [10], Guan et al. [69] extends to low energies by correcting for the Earth’s curvature. The observation angle of 20 deg, used herein, is a typical pointing direction for surface muography experiments.

For the present purpose of validating the implemented algorithms, let us symmetrise the problem. Let us clip the initial spectrum ϕ_0 to kinetic energies $T_0 \in [T_{min}, T_{max}]$,

and let us assume that transmitted muons are detected provided that their final kinetic energy T_1 is also in $[T_{min}, T_{max}]$. Let us set $T_{min} = 10^{-3}$ GeV and $T_{max} = 10^9$ GeV. This corresponds to the default energy range of PUMAS.

Given the previous toy problem, the transmitted flux Φ_1 is computed using the different transport modes of PUMAS. For the CSDA mode equation (66) is used in forward mode and equation (69) in backward mode. For other energy loss modes a Monte Carlo simulation is done.

In previous work [10], we compared the transmitted flux values in order to assess the accuracy of PUMAS. However, transmission muography is an inverse problem in which one actually determines the column density, $X = \rho d$, from the observed transmitted flux, Φ_1 . Thus, let us instead interpret flux differences as errors on the bulk density. For this purpose, let us consider as reference the flux $\Phi_{1,FS}$ obtained in forward straggled with PUMAS default cutoff (i.e. $x_C = 5\%$), and let us invert it using other computations. This yields an estimate for the column density differing from the “true” value obtained in forward straggled mode by ΔX . Let us further assume that the rock thickness d is known. Then the error ΔX translates to an error, $\Delta\rho = \Delta X/d$, on the reconstructed bulk density given by

$$\frac{\Delta\rho}{\rho} = \frac{\Phi_1^{(-1)} \circ \Phi_{1,FS}(X) - X}{X}. \quad (122)$$

Let us point out that equation (122) provides values that differ significantly from $\Delta\Phi_1/\Phi_1$ for large X . For thick targets, the transmitted flux drops sharply with X , as can be seen on figure 4 of Niess et al. [10]. Consequently, large $\Delta\Phi_1$ lead to small $\Delta\rho$ in this regime. On the contrary, for very thin targets small relative errors on the flux result in larger errors on the density.

The values obtained for $\Delta\rho/\rho$ in CSDA and mixed mode ($x_C = 5\%$) are shown on figure 7. It can be seen that CSDA is a good approximation in this case, up to column densities of $\sim 10^6$ kg/m⁻², i.e. ~ 300 m of standard rock. For thicker targets, CSDA underestimates the transmitted flux, as was previously reported by Sokalski et al. [3]. Consequently, the bulk density is underestimated when assuming CSDA for thick targets.

A more detailed comparison of the mixed and straggled modes is provided on figure 8 considering various cutoff values for radiative losses, i.e. $x_C = 0.1\%$, 1% or 5% . For a given cutoff, mixed and straggled results agree at better than 0.2% . Forward and backward computations also agree within 0.2% , at least down to $x_C = 1\%$. As of PUMAS v1.2, lower cutoff values are not allowed in backward mode (see section 3.5.2).

Comparing results for different cutoff values, it is seen that PUMAS default setting ($x_C = 5\%$) is accurate up to column densities of $\sim 10^7$ kg/m⁻², i.e. ~ 3 km of standard rock. For thicker targets, slight differences are observed, increasing with X up to 0.5% for 10 km of standard rock. However, for such thick targets the transmitted flux is practically extinguished, i.e. it is out of experimental reach. Indeed, let us point out that current muography detectors have typical exposures smaller than $\sim 2\pi$ m² sr. With the flux model considered herein, this would result in rates lower than 1 event per year for targets thicker than 3.0 km of standard rock (indicated as the shaded region in figure 8). Thus, in practice PUMAS default cutoff is expected to be valid for most muography applications.

In principle, higher cutoff values than $x_C = 5\%$ could be considered as well, depending on the target thickness and on the desired accuracy. However, in practice we

observed that 5% is usually fast enough. For example, if straggling or elastic scattering is activated, then it makes no difference, CPU-wise, to set x_c to a value higher than 5%.

In addition, we also performed a comparison to PROPOSAL v7.0.6 [5, 6] using the same models for radiative DCSs as PUMAS, i.e. SSR for bremsstrahlung and e^+e^- production and DRSS for photonuclear processes. Note however that PROPOSAL uses the parametrization of Sternheimer et al. [34] for the density effect. Thus, in PROPOSAL the electronic stopping power is slightly lower than in PUMAS. The discrepancy reaches 0.4% at GeV energy in standard rock, as discussed in section 2.2.4.

PROPOSAL cuts are set as PUMAS default setting, i.e. $e_{cut} = +\infty$ (see [5]) and $x_c = 5\%$. Continuous randomisation is disabled since PUMAS does not include radiative processes in its straggling. Using this setting, an excellent agreement is found between PROPOSAL and PUMAS for thick targets. For thin targets, a discrepancy is observed. The inverted densities using PROPOSAL are slightly larger than the ones obtained with PUMAS. The discrepancy reaches a value of 0.4% at small X , i.e. depths of a few metres in standard rock. This is consistent with differences in the electronic stopping power discussed previously.

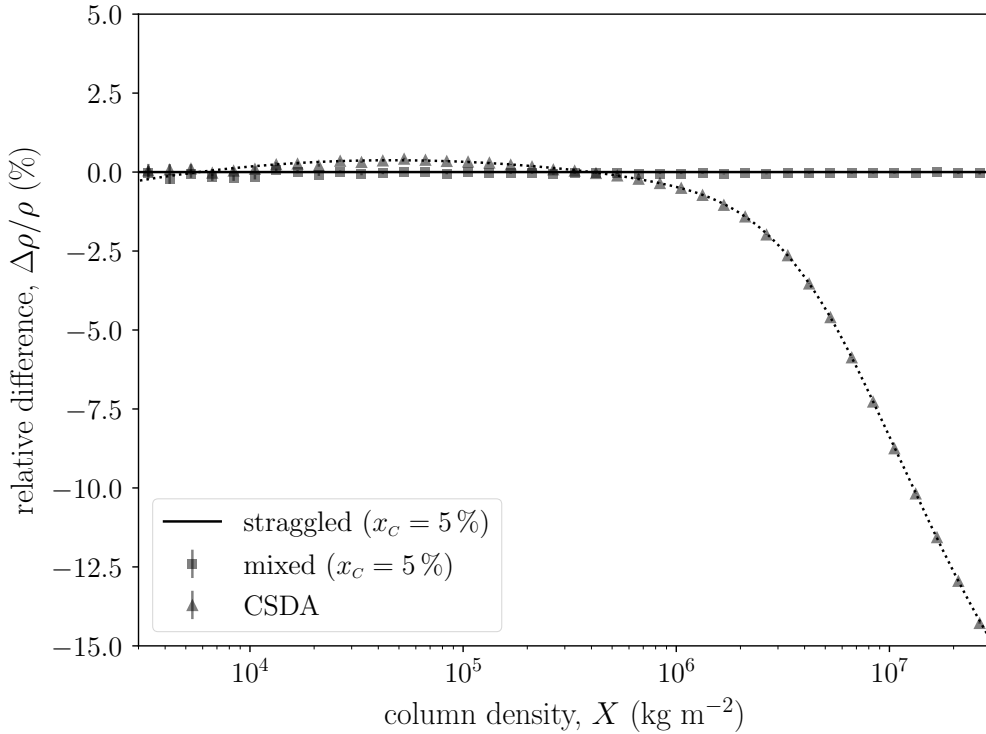


Figure 7: Relative differences on the reconstructed bulk density using CSDA or mixed mode instead of straggled one. A muon in standard rock is considered. Monte Carlo simulations are performed with PUMAS default cutoff for radiative losses, i.e. $x_c = 5\%$.

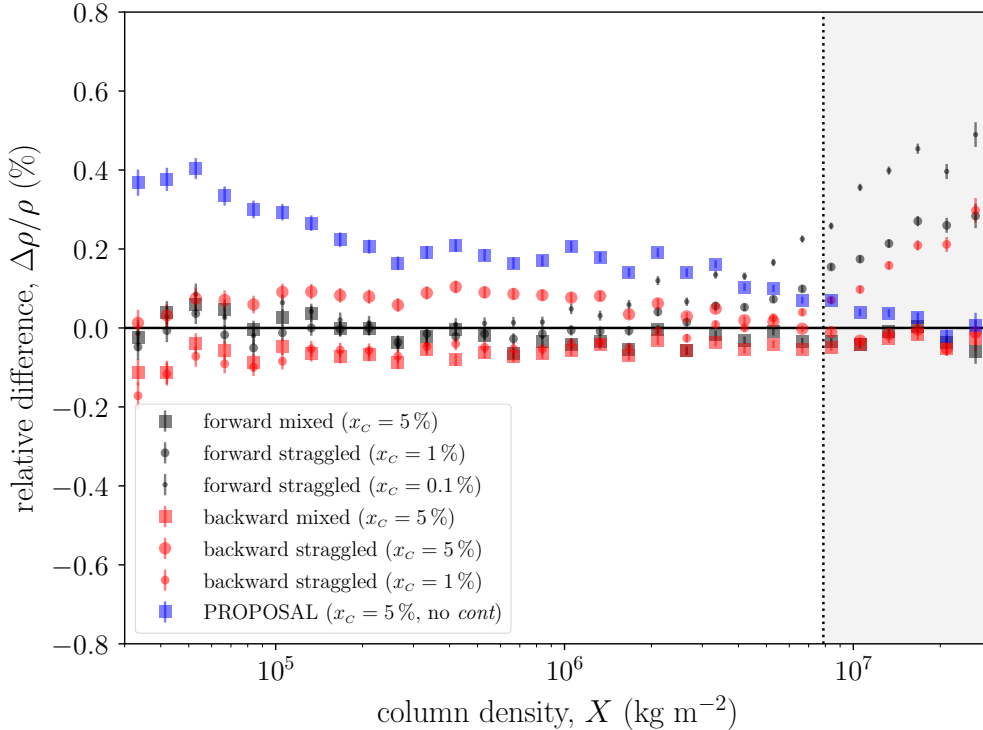


Figure 8: Relative differences on the reconstructed bulk density using mixed or straggled modes for the energy loss simulation, and using backward or forward Monte Carlo. A muon in standard rock is considered. The results obtained for various cutoff values are reported, i.e. $x_c = 0.1\%$, 1% or 5% (PUMAS default). A comparison to PROPOSAL [5, 6] is also shown. The shaded area indicates the region where the rate of events drops below 1 per year, considering an exposure of $2\pi \text{ m}^2 \text{ sr}$.

5.2. Scattering muography

PUMAS was primarily designed in order to solve the transmission muography forward problem. However, it also integrates a detailed elastic scattering model. An accurate description of the scattering of low energy muons ($E \lesssim 10 \text{ GeV}$) is needed in order to simulate background events as discussed in the following section 5.3. Thus, a priori, PUMAS could also be used for simulating scattering muography experiments. However, to our knowledge Geant4 [64–66] fulfils well this use case.

Various internal tests have been carried out in order to validate the software implementation of single and multiple elastic scattering of muons in PUMAS. In particular, we compared PUMAS’ mixed simulation results to a “brute force” Monte Carlo simulation, where every single elastic collision is simulated, i.e. setting $\mu_c = 0$. This test was performed for low energy ($\sim 1 \text{ GeV}$) muons crossing thin foils of standard rock of tens of μm thickness. We found a better than $\sim 1\%$ agreement for the angular and spatial distributions of exiting muons when using PUMAS or a brute force simulation of every elastic collision.

Validating the physics model used in PUMAS for elastic collisions requires a comparison to experimental data. Systematic measurements have been performed by Attwood et al. [71] for 172 MeV/c muons crossing thin foils of various low- Z materials, ranging from H to Fe. Attwood et al. provide unfolded angular distributions for the multiple scattering angle, which allow for direct comparison to Monte Carlo simulations. Figure 9 shows a comparison of PUMAS results to Attwood et al. in the case of an aluminium foil of 1.5 mm. Satisfactory agreement is observed, over five orders of magnitude, for the PDF. However, closer examination shows that the PDFs simulated by PUMAS are systematically broader than the unfolded data, for all target materials. The standard deviation of the simulated scattering angle is 3 to 6% higher than what is expected from the unfolded data. A systematic comparison is provided by table 3.

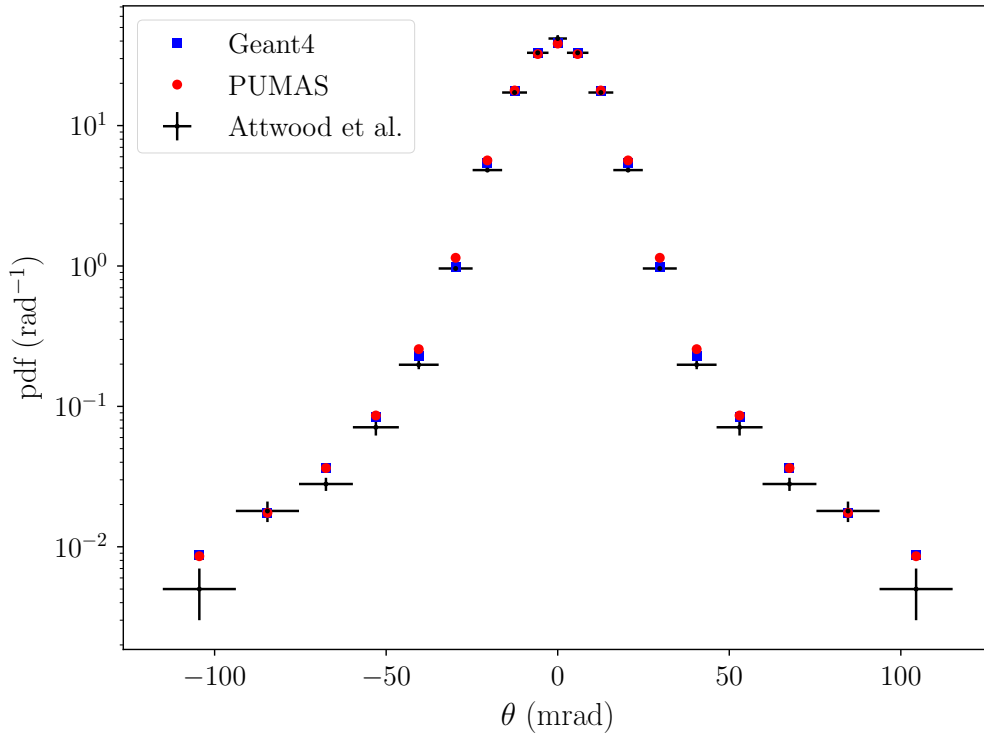


Figure 9: Angular distribution of muons exiting an aluminium foil of 1.5 mm thick. The error bars correspond to the experimental results of Attwood et al. [71] reporting a 172 MeV/c momentum for incident muons. The markers represent the results of PUMAS simulations for 172 and 179 MeV/c incident momentum.

The origin of this discrepancy is not known. It is not specific to PUMAS. The data of Attwood et al. seem to disagree with the elastic DCS obtained from the first Born approximation, even though Coulomb corrections are applied.

In Geant4, this discrepancy has been reduced by assuming that the screening parameter, μ_i in equation (17), is inaccurate. A “correction” is applied such that, for

Table 3: Comparison of PUMAS to experimental values of Attwood et al. [71]. The relative difference on the standard deviation of the multiple scattering angle is reported for various targets. PUMAS simulations have been done for two values of the beam momentum, p , i.e. 172 and 179 MeV/c. The experimental value measured by Attwood et al. is $p = 172$ MeV/c.

p (MeV/c)	H (%)	Li (%)	Be (%)	C (%)	Al (%)	Fe (%)
172	3.2	6.6	5.1	4.9	5.2	2.9
179	-0.6	2.4	0.7	0.5	0.9	-1.2

low- Z materials, the screening parameter is multiplied by ~ 2 . See e.g. line 168 of `G4WentzelOKandVIXSection.cc`.

An alternative explanation for the discrepancy could be an experimental bias. For example, if the momentum of incident muons would actually be higher than 172 MeV/c, estimated by Attwood et al., then the experimental PDFs would be systematically narrower than the ones from simulations with a 172 MeV/c beam. This hypothesis has been tested by performing a global fit of experimental data, but letting the beam energy free. This fit yields a beam momentum of $\hat{p} = 179 \pm 0.5$ MeV/c with a p -value of 27%.

Attwood et al. estimated the beam momentum from time of flight differences between different particles (see e.g. figure 10 of their paper). The reported error is ± 2 MeV, i.e. a 1% relative accuracy. But, this might have been underestimated. A 4% higher beam momentum would be preferred in order to agree with theoretical expectations.

In addition, PUMAS results have also been compared to the experimental scattering data collected by Akimenko et al. [72]. A 1.44 cm thick Copper target is used with incident muons of 7.3 and 11.2 GeV/c. No discrepancy is observed. PUMAS agrees with Akimenko et al. to 0.6% on the standard deviation of the multiple scattering angle. Let us point out that the expansion parameter is $\xi = 21\%$ in this case, as given by equation (12). This leads to a 5% Coulomb correction according to Kuraev et al. [19]. In comparison, for the targets used in Attwood et al. ξ ranges from 0.8% for H ($Z = 1$) to 22% for Fe ($Z = 26$). Thus, the discrepancy between Attwood et al. and Akimenko et al. would not be consistent with misestimated Coulomb corrections.

Given the previous results, it has been decided to trust the theoretical prediction for the elastic scattering DCS. We consider a 4% experimental bias plausible in comparison to a systematic error by a factor of $\sqrt{2}$ on atomic charge radii. As a result of this choice, PUMAS predicts larger scattering angles than Geant4, v10.7 at the time of this writing.

5.3. Background computation

In previous section 5.1, we considered a simple transmission muography experiment. This simplified problem allows us to cross-check the impact on the transmitted flux of uncertainties related to the muon energy loss. However, in a more realistic experiment, not all observed muons propagate straight through the target. In particular, in surface experiments, some down-going atmospheric muons scatter on the target surface, and they are observed as horizontal muons that would have crossed the target. These events are a background for the determination of the target inner structure.

Forward Monte Carlo studies of this background have been performed by Nishiyama et al. [73] and Gómez et al. [7]. However, forward simulations suffer from a large

Monte Carlo inefficiency in this case. The reason for this is well understood from geometric considerations. Contrary to transmitted muons, scattered ones might originate from a large area of the sky, with extents of kilometres. But, only a tiny fraction finally reaches the muography detector, of approximately 1 m extent. Thus, simplifications are needed in order to increase the efficiency of forward Monte Carlo simulations. Therefore, Nishiyama et al. approximated mount Showa-Shinzan, in Japan, using a rotation symmetry around the vertical axis. Reducing the problem dimension, increases the forward Monte Carlo efficiency by approximately 4 orders of magnitude, in this case. This makes forward Monte Carlo simulations of the scattered background tractable on a batch system, but at the cost of a loss of realism.

The backward Monte Carlo procedure available in PUMAS was developed specifically in order to address the problem of the background induced by scattered muons. The reverse Monte Carlo method guarantees that every simulated muon crosses the muography detector. However, it does not guarantee that all events are relevant. For example, not all backward muons reach the sky. Some backward muons end up deep below the ground with energy diverging to absurdly high values. However, this is simple to cope with, e.g. by setting an upper bound on the projectile energy.

In order to validate PUMAS backward method for background computations, let us consider the toy geometry of Nishiyama et al. [73], i.e. a symmetric dome of 270 m high made of standard rock with a bulk density of 2.0 g/cm³. Let us point out that the background method would operate with equal performances if a realistic geometry was used instead, e.g. provided by a Digital Elevation Model (DEM). However, the symmetry assumption is needed in the present case in order to compare forward and backward Monte Carlo results.

Let us assume that the differential flux of atmospheric muons, ϕ_0 , is known on a cylindrical “sky” surface, of 300 m high and 500 m radius, surrounding the target dome. Let us use the parametrisation of Guan et al. [69] for ϕ_0 , as previously in section 5.1. Note that this parametrization is provided for sea level. Thus, in principle a height correction should be applied. This height correction is neglected for the present study.

Following Nishiyama et al., let us consider that the detector is a cylindrical belt, of 500 m radius and of 10 m height, surrounding the dome. The problem consists in computing the flux of atmospheric muons, Φ_1 , that crosses this detector belt as function of the direction of observation w.r.t. the local normal to the detector surface. Owing to the symmetry of the problem, the detector flux Φ_1 does not depend on the radial spherical coordinate. The direction of observation is parametrized with horizontal angular coordinates. An azimuth of 0 deg points toward the central axis of the dome.

Muons are transported between the sky surface and the detector with PUMAS. The transport mode varies depending on the muon energy. Straggling is enabled below 10 GeV. Otherwise, the mixed mode is used. In addition, scattering is disabled above 100 GeV. Both forward and backward Monte Carlo simulations are done using this variable scheme.

In forward mode, muons are generated on the sky surface, while in backward mode they are generated on the detector belt. In both cases, the kinetic energy at generation is randomised from a $1/T$ power law. This results in a log-uniform distribution of generated values, which is efficient for a flux of atmospheric muons spanning several decades in energy. As in section 5.1, the initial and final energy of muons are clipped to $[T_{min}, T_{max}]$, where $T_{min} = 10^{-3}$ GeV and $T_{max} = 10^6$ GeV. In this case, a lower value than previously

is used for T_{max} since one is concerned with the background of low energy muons. In addition, the target model is of moderate size, such that TeV muons are able to cross its largest depth.

The mean values of the detector differential flux, $\bar{\phi}_1$, are computed over three angular control regions: $R1$, $R2$ and $R3$. These regions correspond to the ones defined by Nishiyama et al. [73], but we set a two times larger width in azimuth in order to increase the Monte Carlo statistic. The control regions are visible on figure 11. The corresponding mean differential fluxes are shown on figure 10. At high energy, perfect agreement is found between the forward and backward Monte Carlo results as in section 5.1. The lower the observed muon energy, the less efficient the forward Monte Carlo and the larger the Monte Carlo uncertainties. Forward and backward computations agree within those uncertainties.

The detector mean differential flux has also been computed, in backward Monte Carlo mode, with scattering completely disabled. The results are shown as a dashed line on figure 10. The effect of muon scattering is clearly visible on this figure. Down going atmospheric muons scattering on the target appear as an additional component peaking out at low energy, i.e. ~ 100 MeV for $R2$ and $R3$.

The Monte Carlo simulations have been done on the batch system of CC-IN2P3. The used simulation queue was heterogeneous with both AMD EPYC 7302 and Intel[®] Xeon[®] E5-2650 v4 CPUs. The Monte Carlo performances are measured by the mean time τ_{100} needed in order to achieve a 1% relative accuracy on the detector flux Φ_1 . The values obtained for the three regions of interest are summarised in table 4. When pointing toward the sky, i.e. region $R1$, the backward Monte Carlo is faster than the forward one by 3 orders of magnitude. The most impressive gains are however obtained when pointing through the target, with almost 5 orders of magnitude difference in region $R3$.

The previous gain estimate does not take into account the fact that in forward mode one benefits from using a symmetric target. The corresponding gain can be estimated as the ratio of the belt detector surface, $S_b = 3.1 \cdot 10^4$ m², to the one of a realistic muography detector, i.e. $S_d \simeq 1$ m². This would add 4 extra orders of magnitude speed up in favour of the backward Monte Carlo. However, the gain estimated that way is an upper limit since additional optimizations might be used in forward mode, that have not been considered in the present work. In addition, the reported numbers depend on the detection threshold, T_{min} . The higher the detection threshold the less scattering matters and thus the lower the gain of the backward method.

In any case, it is observed that for transmission muography problems impressive gains can be obtained with backward Monte Carlo. This is particularly true when considering the computation of the background due to low energy scattered muons. Accurate background estimates for realistic topographies are hardly achievable with classical forward techniques.

In order to assess the impact of the background due to scattered muons, let us perform a density inversion. Let us first recall that current muographs cannot measure the energy of detected particles. Thus, only the total flux can be observed, not the differential one w.r.t. the energy.

Let us consider the detector flux computed with scattering enabled as the true values of Φ_1 . Let us estimate the target bulk density using the flux obtained without scattering. The reconstructed density values $\hat{\rho}$ are shown on figure 11. Systematically lower values

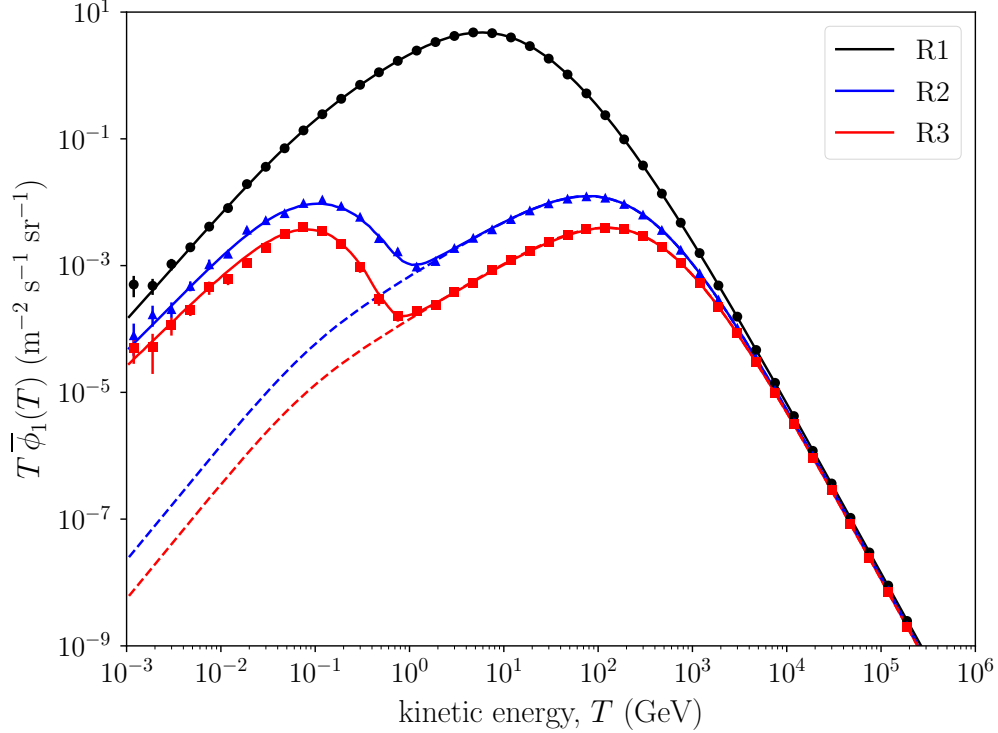


Figure 10: Mean differential flux of muons in the control regions $R1$ (black), $R2$ (blue) and $R3$ (red) for the Showa-Shinzan toy geometry of Nishiyama et al. [73]. The flux is computed with PUMAS as indicated in the text. A standard rock of bulk density 2.0 g/cm^3 is considered for mount Showa-Shinzan. The solid lines stand for the backward Monte Carlo simulation. The markers with error bars indicate the forward Monte Carlo results. The dashed lines show the flux obtained when scattering is disabled.

are found than the true density, i.e. 2.0 g/cm^3 . The reconstructed densities vary from 1.1 g/cm^3 to 1.8 g/cm^3 .

Interestingly, the highest bias is not observed in the central control regions, $R1$, $R2$ or $R3$, but instead on the flanks at points where the slope of mount Showa-Shinzan changes. This indicates that the background due to scattered muons depends on the details of the target shape. Studies of real world targets, with topographies given by DEMs, have shown that some detector locations can be significantly better than others in order to reduce the background. PUMAS can help with that respect, in the process of selecting a proper deployment site.

As stated previously, the present results depend on the detection energy threshold T_{min} , thus on the detector characteristics. The higher this threshold, the lower the bias. In addition, as observed by Nishiyama et al. [73], not only muons contribute to the background but also low energy protons and electrons. PUMAS cannot simulate those.

Table 4: Mean CPU time, τ_{100} , in order to achieve a 1% Monte Carlo accuracy on the flux of muons, Φ_1 . The results for the three control regions, R_1 , R_2 and R_3 are reported for both forward and backward Monte Carlo modes.

region	mode	τ_{100} (h)
R_1	forward	32.9
	backward	0.145
R_2	forward	1 317
	backward	0.540
R_3	forward	3 082
	backward	0.614

6. Conclusion

Muography has been a booming spin-off of astroparticle physics over the last decade, with a plethora of potential applications. Some of these applications require sophisticated computations, whereas faster but more approximate computations are appropriate for others. The PUMAS library is designed to cope with these various cases. It provides a framework with a configurable accuracy, from fast CSDA estimates to detailed backward Monte Carlo computations.

The PUMAS library is an open source project available online under the terms of the LGPL-3.0 license. It benefited from other open source projects, e.g. Geant4 [64–66] and PROPOSAL [5, 6], as well as from a detailed related literature, in particular for the PENELOPE Monte Carlo [27, 74, 75].

In this article, we gave a comprehensive description of the physics implemented in PUMAS. Particular care is taken in being accurate both on the energy loss and on the scattering, over a large range of energies relevant to muography. For transmission muography, good agreement, within 0.4%, is found between PUMAS and PROPOSAL. The observed differences could be related to the use of two different models for the density effect. Considering existing data, both models are valid. Concerning multiple scattering, a 4% discrepancy is observed between experimental results of Attwood et al. [71], on one side, and Akimenko et al. [72] and the theory, on the other side. Additional measurements would be needed in order to assess if this is a theoretical or experimental issue. In the current state, PUMAS follows theoretical predictions. As a result it differs from Geant4, which has been tuned according to the experimental data of Attwood et al.

The unique feature of PUMAS lies in its backward Monte Carlo algorithm. A mathematical description of this technique was provided previously by Niess et al. [10]. In the present article, the main results, relevant to PUMAS, have been summarised in physicist language. Moreover, the efficiency of the backward Monte Carlo method for background estimates has been illustrated.

The PUMAS library is implemented in C99 with no other external dependency but the standard library. It exposes a low level C API whose description is available from the website [11]. The Monte Carlo geometry is supplied by the user as a callback function. This design makes PUMAS very portable, flexible and easy to interface with other codes, not necessarily limited to muography. However, this flexibility comes at a price. It implies

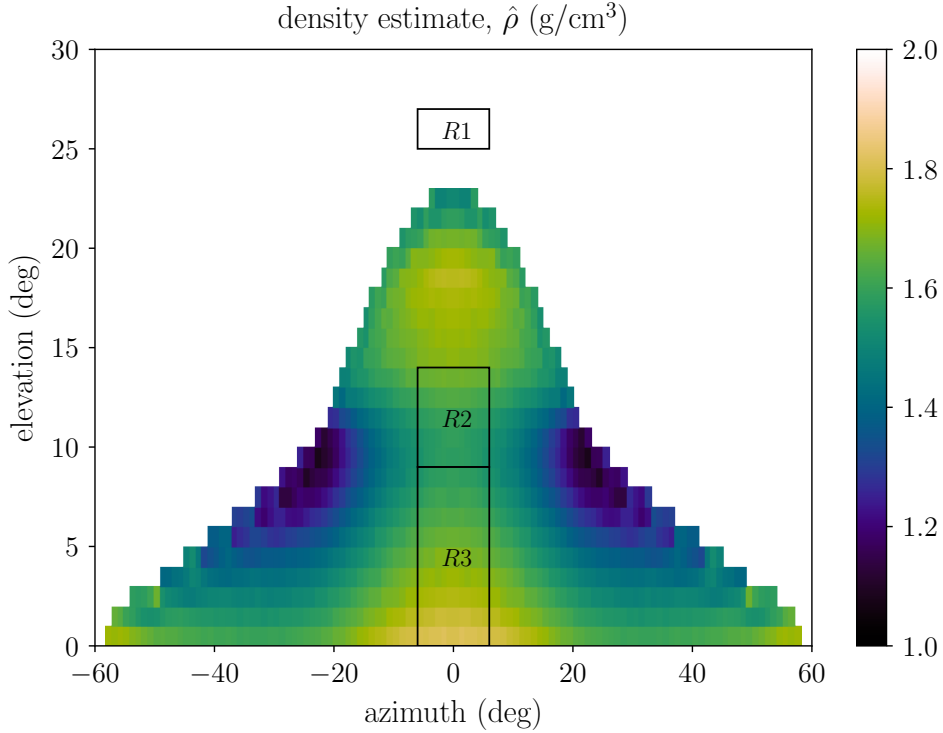


Figure 11: Impact of the scattering on the inverted bulk densities. The Showa-Shinzan geometry of Nishiyama et al. [73] is considered as target. The reported densities, $\hat{\rho}$, are computed by inverting the flux values with scattering using the flux values without scattering. The three control regions, $R1$, $R2$ and $R3$ are also indicated on the figure.

that PUMAS cannot be used out of the box without a minimum of coding. This can be a limitation for the community. Thus, a future improvement would be the development of a Python wrapper.

Acknowledgements

The author thanks J. Linnemann and an anonymous reviewer for their critical reading which contributed to improve the present paper. In addition, we gratefully acknowledge support from the CNRS/IN2P3 Computing Center (Lyon - France) for providing computing and data-processing resources needed for this work. Monte Carlo data analysis was done with numpy [76], and figures were produced with matplotlib [77].

Appendix A. Wallace correction to the eikonal approximation

Following Wallace [17], the eikonal phase is given by

$$\varphi(r) = -2\xi \int_r^{+\infty} \frac{\omega(r')}{\sqrt{r^2 - r'^2}} (1 + \lambda\dot{\omega}(r')) dr', \quad (\text{A.1})$$

$$\lambda = \frac{\alpha z Z \hbar}{\beta p_0}, \quad (\text{A.2})$$

where $\dot{\omega}$ is the first derivative of ω with respect to r . This expression is equivalent to Molière [78], i.e. equation (9) herein, but using an effective atomic charge Z_{eff} and an effective screening function ω_{eff} , as

$$Z_{eff} = Z(1 + \lambda\dot{\omega}(0)), \quad (\text{A.3})$$

$$\omega_{eff}(r) = \frac{Z}{Z_{eff}} \omega(r) (1 + \lambda\dot{\omega}(r)). \quad (\text{A.4})$$

Let us now consider the screening function defined by equation (8). The corresponding effective parameters are

$$Z_{eff} = Z \left(1 - \lambda \sum_{i=1}^n a_i b_i \right) \quad (\text{A.5})$$

$$\begin{aligned} \omega_{eff}(r) = & \sum_{i=1}^n a_i e^{-b_i r} - \lambda \sum_{i=1}^n a_i^2 b_i e^{-2b_i r} \\ & - \lambda \sum_{i=1}^n \sum_{j=i+1}^n a_i a_j (b_i + b_j) e^{-(b_i + b_j)r} \end{aligned} \quad (\text{A.6})$$

The latter is also a sum of exponentials but with $n(n+1)/2$ extra factors. Hence, the same elastic DCS could be used than in equation (27), but using an effective charge Z_{eff} and with $n(n+3)/2$ screening terms instead of n . Doing so would however significantly increase the CPU cost related to the elastic cross-section, since the number of terms to evaluate is increased quadratically. Thus, let us first estimate the magnitude of the Wallace correction in the case of muons. Let us denote δ_W the maximum relative difference of the CM elastic DCS using the Wallace correction or not. In practice, the difference is largest at large scattering angles, reaching a plateau value. Values of δ_W are represented on figure A.12 as function of the muon kinetic energy, for different target atoms. The difference increases as $\sim Z^{1.4}$, and it decreases approximatively as the inverse of the muon kinetic energy. For uranium, δ_W reaches 2% at 1 MeV. Let us point out that similar results are obtained when considering the elastic cross-section or the transport path instead of the maximum DCS deviation. Hence, the Wallace correction is significant only below $\simeq 1$ MeV for muons colliding on heavy elements. But, at this energy the muon range in heavy elements is very small w.r.t. the typical extent of muography targets, i.e. metres to kilometres. E.g. a 1 MeV muon has a range below 10 μm in uranium. Therefore, such corrections are irrelevant for the present purpose.

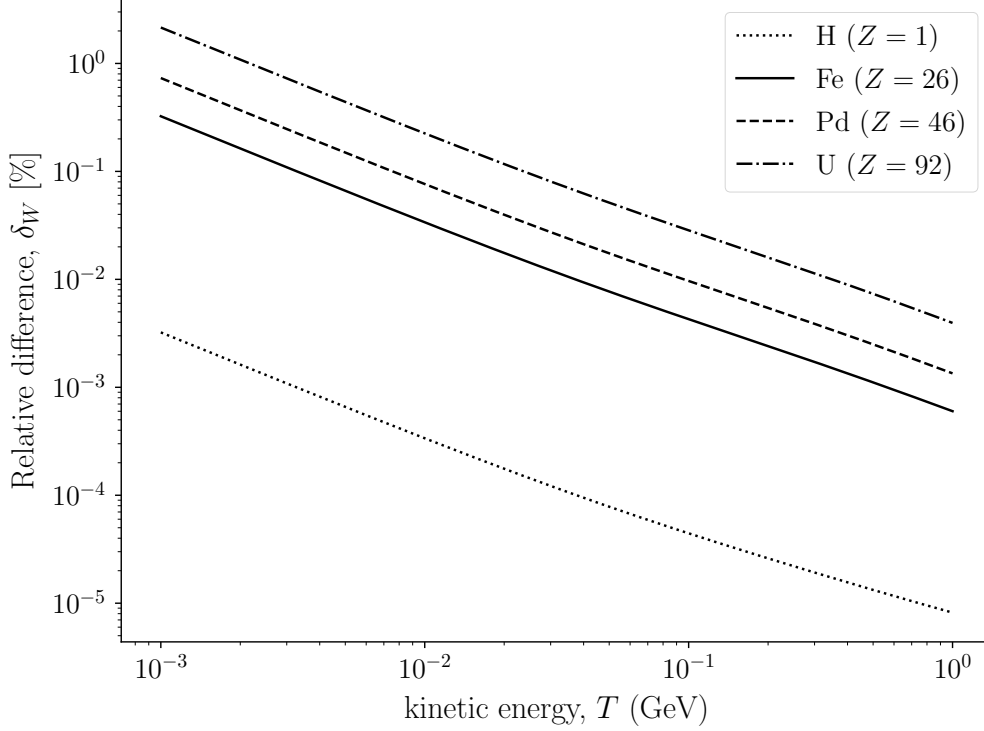


Figure A.12: Relative difference on the CM elastic DCS using the Wallace correction or not. A muon is considered. The different curves correspond to different target atoms as indicated on the figure.

Appendix B. Coulomb correction with a sum of exponentials

Using Kuraev et al. [19] notations, for a sum of exponentials as given by equation (8) herein, the screening function $q(\chi)$ is given by

$$q(\chi) = \left(\sum_{i=1}^n a_i \frac{\chi^2}{\chi^2 + \chi_i^2} \right)^2, \quad (\text{B.1})$$

where $\chi_i^2 = 4\mu_i$. It follows that equation (16) of Kuraev et al. is modified as

$$\lim_{\zeta \rightarrow \infty} \left[\int_0^\zeta \frac{d\chi}{\chi} q(\chi) + \frac{1}{2} - \ln \zeta \right] = - \sum_{i=1}^n a_i^2 \ln \chi_i - 2 \sum_{i=1}^n \sum_{j=i+1}^n a_i a_j \frac{\chi_i^2 \ln \chi_i - \chi_j^2 \ln \chi_j}{\chi_i^2 - \chi_j^2} + \frac{1}{2} \left(1 - \sum_{i=1}^n a_i^2 \right), \quad (\text{B.2})$$

where we have made use of $\sum a_i = 1$. Comparing with the original result, one has to substitute $-\ln \chi_a$ in equation (18) with the r.h.s. of the latter equation (B.2). Let L be

the latter limit and let us rescale all screening factors χ_i by a single factor e^δ such that $\chi'_i = e^\delta \chi_i$. Then, the limit is modified as

$$\Delta L = \delta, \quad (\text{B.3})$$

where again we make use of $\sum a_i = 1$. Thus, in equation (36) of Kuraev et al. we can substitute $\delta = f(\xi)$ for $\Delta_{CC} [\ln(\chi'_a)] = f(\xi)$. This shows that for a sum of exponentials, rescaling all screening parameters χ_i (i.e. b_i) by $e^{f(\xi)}$ allows one to recover the eikonal multiple scattering distribution, in the limit of small angles assumed in Kuraev et al.

Let us now consider the nucleus finite extent where the screening function is modified by a factor $\Delta\omega_N$, i.e. equation (21) herein. Let us consider the following parametrization of the nuclear charge density:

$$\rho_N(r) = \frac{1}{4\pi r (R_2^2 - R_1^2)} \left(e^{-\frac{r}{R_2}} - e^{-\frac{r}{R_1}} \right), \quad (\text{B.4})$$

where $R_2 > R_1$. Note that this differs from the exponential density considered by Butkevich et al. [22] by a factor $1/r$. The nuclear charge density (B.4) yields the following modification to the screening function:

$$\Delta\omega_N(r) = \frac{R_2^2}{R_2^2 - R_1^2} e^{-\frac{r}{R_2}} - \frac{R_1^2}{R_2^2 - R_1^2} e^{-\frac{r}{R_1}}. \quad (\text{B.5})$$

The resulting screening function is a sum of exponentials but with two extra nuclear terms. It still satisfies $\sum a_i = 1$. Therefore, with the nuclear charge density given by equation (B.4) the Coulomb correction from Kuraev et al. [19] is still valid.

Let us further consider the case where $R_1 \simeq R_2$ and let us write $R_1 = R(1 - \epsilon)$ and $R_2 = R(1 + \epsilon)$. Substituting into equation (B.4) yields

$$\rho_N(r) = \frac{1}{8\pi R^3} e^{-\frac{r}{R}} + \mathcal{O}(\epsilon). \quad (\text{B.6})$$

In the limit $\epsilon \rightarrow 0$, one recovers the exponential nuclear charge distribution used e.g. by Butkevich et al. [22]. Considering the limit $\epsilon \rightarrow 0$ in equation (B.2) we need to scrutinize the term

$$\lim_{\epsilon \rightarrow 0} \left[\frac{\chi_2^2 \ln \chi_2 - \chi_1^2 \ln \chi_1}{\chi_2^2 - \chi_1^2} \right] = \ln \chi_N + \frac{1}{2}, \quad (\text{B.7})$$

where $\chi_1 = \frac{\chi_N}{1-\epsilon}$, $\chi_2 = \frac{\chi_N}{1+\epsilon}$ and $\chi_N = \frac{\hbar}{p_0 R}$. Thus, in the limit of the exponential nuclear charge distribution equation (B.3) is unchanged. This proves that the scaling $\delta = f(\xi)$ can also be applied to the exponential nuclear density, e.g. to its inverse radius, $\frac{1}{R}$.

Appendix C. Nuclear charge radii

Vries et al. [21] provides an extensive compilation of data relative to nuclear charge distributions. In particular, table I collects estimates of the r.m.s. radius, $\sqrt{\langle r^2 \rangle}$. For the nuclear charge distribution of equation (23) one obtains

$$R_N^2 = \frac{5}{6} \langle r^2 \rangle, \quad (\text{C.1})$$

which let us set the radius parameter R_N .

Note that most entries in table I of Vries et al. [21] concern specific isotopes, e.g. ^{12}C or ^{14}C . In PUMAS, we usually do not make this distinction, although it could be done if desired. Instead, for a given atomic number Z , a single element is used with an average atomic mass A , considering isotope natural abundances. In order to determine the nuclear charge radius of these average elements the following procedure is used. For a given Z , we consider all isotope data available in Vries et al. and select the bracketing ones, i.e. the largest below A and the lowest above A in atomic mass. Let (A_0, r_0) and (A_1, r_1) denote the corresponding bracketing values with $A_0 < A_1$, and let r_0, r_1 be the corresponding nuclear charge radii. If no isotope is found with atomic mass above or below, we repeat the search for the missing(s) bound, but considering all data available this time, i.e. other atomic elements with different Z . Once a proper bracketing is found, the mean nuclear charge radius $\sqrt{\langle r^2 \rangle}$ is estimated from a linear interpolation in log-log using the bracketing values, as

$$\ln \sqrt{\langle r^2 \rangle} = \ln r_0 + \frac{\ln(A/A_0)}{\ln(A_1/A_0)} \ln \left(\frac{r_1}{r_0} \right). \quad (\text{C.2})$$

The procedure described previously works for $Z \leq 92$, i.e. uranium. For atomic elements with larger Z there are no entries in the compilation of Vries et al. [21]. Then, an extrapolation is used instead, as

$$\sqrt{\langle r^2 \rangle} = 1.32A^{0.27} \text{ fm}, \quad (\text{C.3})$$

following Butkevich et al. [22] but with a higher prefactor matching high Z data.

The results of this procedure are compiled in table C.5 and summarised on figure C.13. The corresponding mean atomic masses A , taken from the PDG, are also indicated in the table. Note that for $Z = 1$, we make an explicit distinction between hydrogen and its other isotopes, e.g. Deuterium, since in this case the nuclear charge radii are significantly different.

Appendix D. Implementation of elastic collisions

Hard elastic collisions are randomised using a rejection sampling method. The elastic DCS of equation (27) is bounded from above by

$$\frac{d\sigma_0}{d\mu_0} \leq \pi \left(\frac{\alpha Z \hbar}{\beta p_0} \right)^2 \left(\frac{1}{\tilde{\mu}_{\min} + \mu_0} \right)^2, \quad (\text{D.1})$$

where $\tilde{\mu}_{\min} = \min(\tilde{\mu}_i)$. The bounding PDF can be randomised directly using the inverse CDF method, as

$$\mu_0 = \frac{(\tilde{\mu}_{\min} + \mu_H)(\tilde{\mu}_{\min} + 1)}{\tilde{\mu}_{\min} + 1 - \xi(1 - \mu_H)} - \tilde{\mu}_{\min}, \quad (\text{D.2})$$

where μ_H is the cutoff value between soft and hard elastic scattering, and where ξ is a random number uniformly distributed over $[0, 1]$.

The simulation of elastic collisions also requires integrating the elastic DCS and its first moment, as discussed in section 3.4 (see e.g. equation (87)). With the U² nuclear

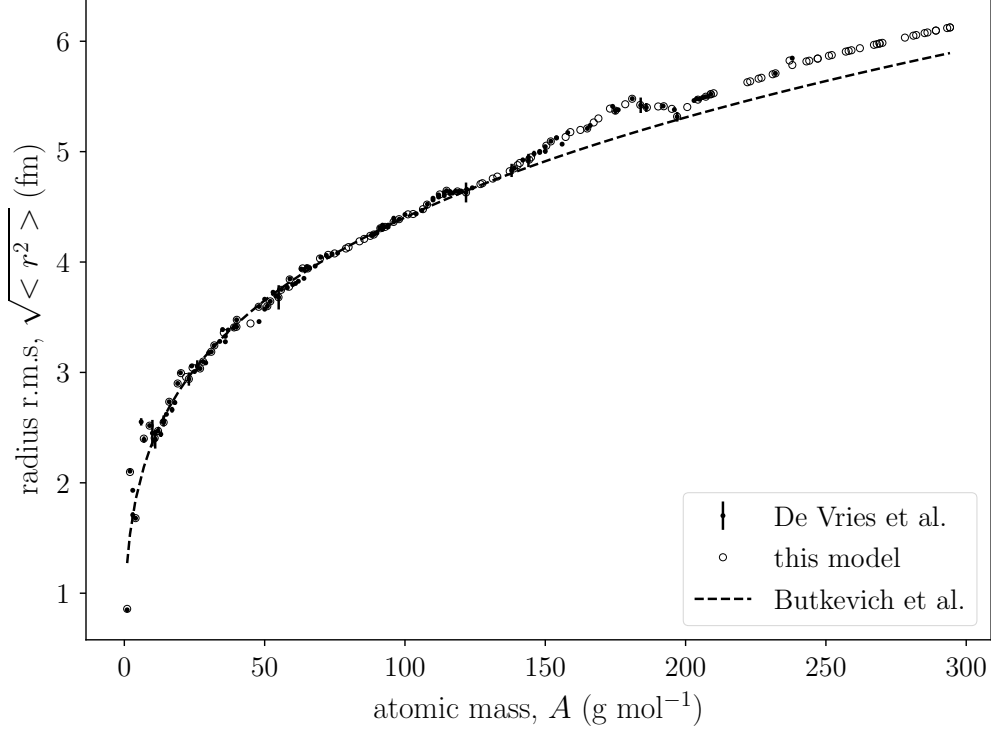


Figure C.13: Nuclear charge radii, $\sqrt{\langle r^2 \rangle}$. The black dots with error bars correspond to the compilation of Vries et al. [21]. The open dots are the fit results used in PUMAS. The dashed line indicates the model used by Butkevich et al. [22].

form factor, this would require a numerical integration. However, in this case the integral is well approximated by using a smoother nuclear form factor, obtained from an exponential charge density, as

$$F_{exp} = \left(\frac{\tilde{\mu}_{n+1}}{\tilde{\mu}_{n+1} + \mu} \right)^4, \quad (\text{D.3})$$

where $\tilde{\mu}_{n+1} = 10\tilde{\mu}_{n+1}$ (see equation (29) for definition of $\tilde{\mu}_{n+1}$). Consequently, the elastic DCS is approximated by a rational fraction in μ_0 with the following shape:

$$R(x) = \left(\sum_{i=1}^n \frac{A_i}{x_i + x} \right)^2 \frac{x_{n+1}^4}{(x_{n+1} + x)^4} (1 - Bx). \quad (\text{D.4})$$

This rational fraction can be reduced to

$$R(x) = \left(\sum_{i=1}^n \frac{a_i}{(x_i + x)^2} + \sum_{i=1}^n \frac{b_i}{x_i + x} + \sum_{i=1}^4 \frac{c_i}{(x_{n+1} + x)^i} \right) (1 - Bx). \quad (\text{D.5})$$

The coefficients a_i , b_i and c_i of the reduction are given by

$$a_i = r_{n+1,i}^4 A_i^2, \quad (\text{D.6})$$

$$b_i = r_{n+1,i}^4 (s_i - 4A_i^2 d_{n+1,i}), \quad (\text{D.7})$$

$$c_i = x_{n+1}^{i-1} \left(\frac{5-i}{x_{n+1}} \sum_{j=1}^n A_j^2 r_{n+1,j}^{6-i} - \sum_{j=1}^n s_j r_{n+1,j}^{5-i} \right), \quad (\text{D.8})$$

where

$$d_{ij} = \frac{1}{x_i - x_j}, \quad r_{ij} = \frac{x_i}{x_i - x_j} \quad \text{and} \quad s_i = 2A_i \sum_{j=1, j \neq i}^n A_j d_{ji}. \quad (\text{D.9})$$

The reduced fraction given by equation (D.5) can be integrated analytically yielding the (restricted) elastic cross-section for higher moments, e.g. the transport path. The m^{th} moment is

$$\begin{aligned} \int_0^{x_0} R(x) x^m dx &= \sum_{i=1}^n a_i (I_{m,2}(x_0, x_i) - BI_{m+1,2}(x_0, x_i)) + \\ &\quad \sum_{i=1}^n b_i (I_{m,1}(x_0, x_i) - BI_{m+1,1}(x_0, x_i)) + \\ &\quad \sum_{i=1}^4 c_i (I_{m,i}(x_0, x_{n+1}) - BI_{m+1,i}(x_0, x_{n+1})), \end{aligned} \quad (\text{D.10})$$

where

$$I_{m,p}(a, b) = \int_0^a \frac{x^m}{(b+x)^p} dx, \quad (\text{D.11})$$

for $m \geq 0$ and $p \geq 0$. Depending on the use case, the upper bound x_0 in integral (D.10) can stand for the angular cutoff parameter, μ_c , defined in the CM frame, or $x_0 = 1$ when computing the total moment. The latter family of integrals can be computed by recurrence starting from

$$I_{m,0} = \frac{a^{m+1}}{m+1}, \quad (\text{D.12})$$

$$I_{0,p} = \begin{cases} \ln\left(1 + \frac{a}{b}\right) & \text{if } p = 1 \\ \frac{1}{p+1} \left(\frac{1}{a^{p+1}} - \frac{1}{(a+b)^{p+1}} \right) & \text{if } p \geq 2 \end{cases}, \quad (\text{D.13})$$

and using the recurrence relation

$$I_{m+1,p+1} = I_{m,p} - bI_{m,p+1}. \quad (\text{D.14})$$

While the previous expressions for the integral of elastic DCS might seem complicated for an analytical resolution, the implementation in a computing language like C is rather straightforward. Nevertheless, due to rounding errors, the integrated reduced fraction can be numerically unstable at high energies, where the screening factor are very small. This can be solved by noting that $c_0 + \sum b_i = 0$, e.g. by considering the limit $xR(x)/(1-Bx)$

when $x \rightarrow \infty$ in equation (D.5). Thus, the terms depending only on x_0 can be set to zero when injecting $I_{m,1}$ and $I_{m+1,1}$ back in equation (D.10). This was found to solve the numerical instabilities at high energy.

Using the parametrization of Salvat et al. [14] for the screening function, the case of hydrogen was found numerically problematic even at low energies. This can be understood by looking at the corresponding parameter values. The exponents b_i differ only by 0.3% and, as a result, the prefactors a_i are very large with opposite signs. This is pathological, suggesting that the double exponential model is not relevant in the case of hydrogen. Therefore, in this case we decided to use a single exponential instead with an exponent b_H fitted in order to reproduce the same transport path as the original model of Salvat et al. [14]. This procedure yields

$$b_H = 1.1172 a_0, \quad (\text{D.15})$$

where a_0 the Bohr radius. Note that the value obtained that way is close from the one given by the Thomas-Fermi model, i.e. $b_{TF} = 1.1299 a_0$.

Let us point out that equation (D.10) assumes that the integration is done in the CM frame. However, the transport path is needed in the laboratory frame. In order to transform the integral to the laboratory, frame we use the following approximation. For small angles, the reduced angular parameter in the laboratory frame, μ , is proportional to the CM one, μ_0 , as:

$$\mu = \frac{1}{\gamma_{\text{CM}}^2 (1 + \tau)^2} \mu_0 + \mathcal{O}(\mu_0^2), \quad (\text{D.16})$$

where

$$\gamma_{\text{CM}}^2 = \frac{(E + m_A)^2}{m^2 + 2m_A E + m_A^2}, \quad (\text{D.17})$$

and

$$\tau = \frac{m_A E + m^2}{m_A E + m_A^2}, \quad (\text{D.18})$$

where m_A is the target atom rest mass energy. Consequently the moments of the elastic DCS in the CM and laboratory frames are approximatively related by

$$\int \mu^m \frac{d\sigma}{d\mu} d\mu \simeq \frac{1}{\gamma_{\text{CM}}^{2m} (1 + \tau)^{2m}} \int \mu_0^m \frac{d\sigma_0}{d\mu_0} d\mu_0. \quad (\text{D.19})$$

The higher the projectile energy the more accurate the previous approximation, due to the relativistic boost factor γ_{CM} that squeezes the scattering angle towards small values, as can be seen from equation (D.16). On the contrary, the higher the projectile energy the less accurate the approximation of the nuclear form factor with an exponential distribution, because the closer to the nuclei the projectile can reach. The combined effect of both approximations was checked by comparing the result of the analytical integration, using equation (D.10) together with (D.16), to a numeric integration of the initial elastic DCS, given by (27), but transformed to the laboratory frame. The total approximation error was found to be at most 1% for muon kinetic energies between 1 MeV to 1 EeV. This is considered acceptable for the present purpose.

Appendix E. Radiative correction to the electronic stopping power

Computing the contribution of the radiative correction to the electronic stopping power requires integrating terms such as $\Delta_{e\gamma}\nu^p$, with $p \in \{-1, 0, 1\}$. An analytical approximation can be obtained as following. First, let us point out that the variation of $\Delta_{e\gamma}$ with ν is logarithmic, hence mild. Then, inspecting the energy loss due to close interactions without the radiative correction, it is observed that the term $p = -1$ gives the dominant contribution. Further noting that $\Delta_{e\gamma} \rightarrow 0$ for $\nu \ll m_e$, it is expected that at high energies the bulk of the energy loss occurs for $m_e \ll \nu \ll E$. Thus, one has:

$$\delta_{e\gamma}(\nu) \simeq \frac{\alpha}{2\pi} \int_{m_e/2}^{\nu} \ln\left(\frac{2\nu'}{m_e}\right) \left[2 \ln(2\gamma) - \ln\left(\frac{2\nu'}{m_e}\right) \right] \frac{d\nu'}{\nu'}, \quad (\text{E.1})$$

$$\simeq \frac{\alpha}{2\pi} \ln^2\left(\frac{2\nu}{m_e}\right) \left[\ln(2\gamma) - \frac{1}{3} \ln\left(\frac{2\nu}{m_e}\right) \right], \quad (\text{E.2})$$

where the lower integration limit was arbitrarily set to $m_e/2$ in order to simplify expressions. The approximation provided by equation (E.2) diverges for $\nu \rightarrow \infty$ instead of going to zero. This can be solved by substituting back $1 + 2\nu/m_e$ instead of $2\nu/m_e$ in the logarithm, yielding (43). The latter approximation results in an error on the electronic loss that increases steadily with the projectile energy. At EeV it reaches $\sim 1\%$, which is considered accurate enough since at those energies the energy loss is highly dominated by other radiative processes.

Appendix F. Tabulations and interpolations

The Monte Carlo transport procedures discussed in section 3 imply several integral quantities, like the stopping power or the CSDA range. Computing those on the fly at each Monte Carlo step would be prohibitive CPU-wise. Instead, these quantities are tabulated, at PUMAS initialisation, as function of the projectile kinetic energy. Then, intermediate values are interpolated using cubic splines, as detailed below.

Let us consider a continuous property, f , whose values f_i have been computed at n knots x_i . For a given x in $[x_0, x_{n-1}[$ the value $f(x)$ at x is estimated in two steps, as

- (i) First, the bracketing interval $[x_i, x_{i+1}[$ with $x_i \leq x < x_{i+1}$ is determined using a bisection.
- (ii) Then, the value $f(x)$ is estimated by interpolation on $[x_i, x_{i+1}[$ using an order 3 polynomial, H_i , matching f and its first derivative, f' , at x_i and x_{i+1} .

The matching polynomial, H_i , can be cast as

$$H_i(x) = \sum_{j=0}^3 a_{ij} t_i^j, \quad (\text{F.1})$$

$$a_{i,0} = f_i, \quad (\text{F.2})$$

$$a_{i,1} = d_i, \quad (\text{F.3})$$

$$a_{i,2} = -3(f_i - f_{i+1}) - 2d_i - d_{i+1}, \quad (\text{F.4})$$

$$a_{i,3} = 2(p_i - p_{i+1}) + d_i + d_{i+1}, \quad (\text{F.5})$$

where $t_i = (x - x_i)/(x_{i+1} - x_i)$, $d_i = f'(x_i)(x_{i+1} - x_i)$ and $d_{i+1} = f'(x_{i+1})(x_{i+1} - x_i)$.

In some cases the derivative values f' of f are not known. Then, combinations of finite differences are used instead, following Fritsch and Butland [79]. The latter procedure ensures that the cubic spline respects the local monotonicity of the tabulated values. This is relevant in the present case since the interpolated quantities are monotonic or have single extrema. Therefore, even when the derivative values are known, the smoothing procedure of Fritsch and Butland is applied to knots where the derivative does not satisfy to the local monotonicity condition (see e.g. Higham [80]).

By default, PUMAS tabulations are generated using a log like grid in kinetic energy as in Groom et al. [12]. The original grid extends up to 1 PeV. This can be limiting for some applications. Therefore, in PUMAS v1.1 the energy grid has been extended to higher energies, 1 EeV for muons and 1 ZeV for taus. The accuracy of the interpolation method used in PUMAS was checked to be better than 0.1% with those grids.

The bisection lookup method allows one to use grids with a non regular spacing, e.g. like the grids of Groom et al. An alternative would be to enforce grids to be regular in $\log x$. Then, the bracketing interval could be inferred directly from $\log x$. One might wonder what is the penalty of using a bisection instead of enforcing a log-regular grid. For grids with $\mathcal{O}(100)$ knots, as used in PUMAS, we did not observe any penalty. This can be understood since computing a log is rather expensive CPU-wise, while the bisection converges with few iterations on average. Note however that the CPU cost of the bisection increases as $\ln n$, while the log-regular method has a flat cost. Therefore, for large grids, using the bisection method might be expensive.

The bisection method was further improved by keeping a record of the two last bracketing intervals. Then, when a new interpolation is requested the recorded intervals are checked first before running any bisection. This is relevant since it is frequent that different properties are requested for the same parameter value, e.g. the kinetic energy. Hence, by keeping a record one avoids running redundant bisections. In addition, for small Monte Carlo steps involving many interpolations, it is likely that the particle spends several steps within a same bracketing interval.

Appendix G. Moments of the soft energy loss

Within CSDA, the soft the energy loss between s_0 and s_1 is given by

$$T_0 - \bar{T}_1 = \int_{s_0}^{s_1} S_s ds, \quad (\text{G.1})$$

with S_s per unit path length, following the notations of the PENELOPE manual [27]. At first order of Taylor expansion in Δs the stopping power, S_s , expands as

$$S_s = S_s(T_0) \left(1 - \dot{S}_s(T_0) \Delta s \right) + \mathcal{O}(\Delta s^2), \quad (\text{G.2})$$

where \dot{S}_s is the derivative of S_s w.r.t. the projectile kinetic energy, T , and where it is made use of $dT = -S_s ds$. Substituting equation (G.2) into (G.1) and integrating yields

$$T_0 - \bar{T}_1 = S_s(T_0) \Delta s \left(1 - \frac{1}{2} \dot{S}_s(T_0) \Delta s \right) + \mathcal{O}(\Delta s^3). \quad (\text{G.3})$$

The right hand side of the previous equation is identical to the result obtained for $\langle\omega\rangle$ in the PENELOPE manual, i.e. equation (4.78). Hence, $T_0 - \bar{T}_1$ is an approximation of $\langle\omega\rangle$ at least up to order 2 of expansion in Δs .

Further expanding the square of the straggling parameter, Ω_s^2 , at first order one obtains

$$\Omega_s^2 = \Omega_s^2(T_0) - \dot{\Omega}_s^2(T_0)S_s(T_0)\rho\Delta s + \mathcal{O}(\Delta s^2). \quad (\text{G.4})$$

Substituting equation (G.4) into (79) and collecting terms up to Δs^2 one finds

$$\begin{aligned} \text{var}(\omega) = & \Omega_s^2(T_0)\rho\Delta s \\ & - \dot{\Omega}_s^2(T_0)\rho S_s(T_0)\frac{\Delta s^2}{2} - \Omega_s^2(T_0)\rho\dot{S}_s(T_0)\Delta s^2 + \mathcal{O}(\Delta s^3). \end{aligned} \quad (\text{G.5})$$

The latter is equivalent to equation (4.79) in the PENELOPE manual [27].

Appendix H. Forward sampling of hard energy losses

Let $x = \nu/T$ denote the fractional energy loss in a radiative collision. Let $I = [x_{min}, x_{max}]$ be the support of the DCS, i.e. the interval where it is strictly positive. Then, the following function is a valid envelope of the DCS at the projectile energy E :

$$f_\alpha(x) = \sup_{x \in I} \left[\frac{d\sigma}{dx} x^\alpha \right] x^{-\alpha}. \quad (\text{H.1})$$

The exponent α is selected by considering the logarithmic derivative of the DCS, β , defined as

$$\beta(x) = \frac{d \ln \left(\frac{d\sigma}{dx} \right)}{d \ln x}. \quad (\text{H.2})$$

Values of β are computed over a regular grid with constant spacing in $\ln x$. The envelope parameter α is set as the median value over this grid. The grid interval is restricted to the lower half of I in logarithmic scale. In addition, boundary values are rejected when they are close to a kinematic threshold of the DCS. In the latter case the DCS has very sharp variations that are not considered as representative.

Typical values of β are between 1 and 3. Thus, when sampling x from the envelope, low values close to x_{min} are more frequent than high ones. Therefore, we select α only from the lower logarithmic half of I . This ensures high selection efficiencies of the rejection sampling method for the most frequent outcomes for x .

Appendix I. Monte Carlo stepping algorithm

The Monte Carlo stepping algorithm used in PUMAS proceeds as following. First, a physical step length is determined depending on the physics processes enabled, as

$$\Delta s_p = \min(\Delta s_E, \Delta s_e, \Delta s_B), \quad (\text{I.1})$$

where Δs_E is given by equation (77), Δs_e by (91) and Δs_B by (121). Note that depending on the enabled processes the previous step length(s) might equal $+\infty$. Note also that

these step lengths can be tuned by the user by modifying a shared accuracy parameter, ϵ_s , configurable per simulation context. By default ϵ_s is set to 1%.

Then, the physical step length is compared to the ones provided by the user for the local density model, Δs_l , and for the medium, Δs_m . The smallest value is used as step length, Δs . If Δs is below a minimal resolution, Δs_{min} , then it is set to Δs_{min} . Thus,

$$\Delta s = \max(\min(\Delta s_p, \Delta s_l, \Delta s_m), \Delta s_{min}). \quad (\text{I.2})$$

Requiring that $\Delta s \geq \Delta s_{min}$ is a generic safeguard since the user callback functions may return values close to zero. The minimal resolution is set to $\Delta s_{min} = 0.1 \mu\text{m}$. Note that PUMAS is not expected to be used for such thin targets.

Once the Monte Carlo step length Δs has been determined, a tentative straight displacement is performed along \vec{u} or, in backward mode, along $-\vec{u}$. The medium and the corresponding step length, Δs_m , at the would-be new position are requested. If a change of medium would occur the projectile is moved slightly before the expected boundary at a distance $\Delta s - \Delta s_{min}/2$ from its initial position. The medium at this location is requested. If it differs from the one at the initial location, then a bisection is done in order to locate the change of medium. Then, the projectile is moved just before the boundary. The bisection is a safeguard in case that the users provides approximate step lengths for the geometry. Note that for the bisection, only the medium needs to be requested to the user, not the distance to the next boundary. If no change of medium is detected, then the initial tentative displacement is confirmed.

Once the projectile location has been updated, the soft energy loss is applied, using CSDA or the straggling algorithm described in section 3. If an external magnetic field was supplied, then the projectile momentum direction \vec{u} is rotated, as discussed previously in section 4.3. In addition, if scattering is enabled, then the direction is further rotated by applying the soft multiple scattering process discussed in section 3.4. If a hard collision occurred, then it is simulated at this stage. If instead a change of medium was found, then the projectile is pushed by a distance Δs_{min} into the new medium. Note that this push occurs without any energy loss. As stated previously, PUMAS is expected to be used only for targets significantly thicker than $\Delta s_{min} = 0.1 \mu\text{m}$. Finally, if the particle direction changed in anyway, then a new medium stepping distance Δs_m must be requested. For this call the medium is known. Thus, it is not requested.

PUMAS stepping algorithm ensures that for any call of the local density model, a call to the medium function occurs before at the exact same location \vec{r} and with the same momentum direction \vec{u} . This can be used in order to optimise the implementation of these two callback functions. For example, some parameters might be recorded in the medium function for later use in the local density model. In addition, the user provided steps lengths, Δs_l and Δs_m , are recorded from one Monte Carlo step to the next one. Thus, for a given transport no user callback should occur twice for the same projectile state. For non uniform density models, the density values are also recorded between steps. These values are used for interpolating the density variations over the Monte Carlo step.

References

- [1] Kunihiro Morishima, Mitsuaki Kuno, Akira Nishio, et al. Discovery of a big void in khufu's pyramid by observation of cosmic-ray muons. *Nature*, 552:386–390, 2017. ISSN 14764687. doi:10.1038/nature24647.

- [2] Lorenzo Bonechi, Raffaello D'Alessandro, and Andrea Giammanco. Atmospheric muons as an imaging tool. *Reviews in Physics*, 5:100038, 11 2020. ISSN 24054283. URL: <https://linkinghub.elsevier.com/retrieve/pii/S2405428320300010>, doi:10.1016/j.revip.2020.100038.
- [3] Igor A Sokalski, Edgar V Bugaev, and Sergey I Klimushin. {MUM}: Flexible precise monte carlo algorithm for muon propagation through thick layers of matter. *Phys. Rev. D*, 64:74015, 9 2001. URL: <http://link.aps.org/doi/10.1103/PhysRevD.64.074015>, doi:10.1103/PhysRevD.64.074015.
- [4] V. A. Kudryavtsev. Muon simulation codes music and musun for underground physics. *Computer Physics Communications*, 180:339–346, 2009. ISSN 00104655. doi:10.1016/j.cpc.2008.10.013.
- [5] J.-H. Koehne, K. Frantzen, M. Schmitz, et al. Proposal: A tool for propagation of charged leptons. *Computer Physics Communications*, 184:2070–2090, 9 2013. ISSN 00104655. URL: <https://linkinghub.elsevier.com/retrieve/pii/S0010465513001355>, doi:10.1016/j.cpc.2013.04.001.
- [6] Mario Dunsch, Jan Soedingrekso, Alexander Sandrock, et al. Recent improvements for the lepton propagator proposal. *Computer Physics Communications*, 242:132–144, 9 2019. ISSN 00104655. URL: <https://linkinghub.elsevier.com/retrieve/pii/S0010465519301201>, doi:10.1016/j.cpc.2019.03.021.
- [7] H. Gómez, D. Gibert, C. Goy, et al. Forward scattering effects on muon imaging. *Journal of Instrumentation*, 12, 2017. ISSN 17480221. doi:10.1088/1748-0221/12/12/P12018.
- [8] Jaime Álvarez Muñoz, Rafael Alves Batista, Aswathi Balagopal V, et al. The giant radio array for neutrino detection (grand): Science and design. *Science China: Physics, Mechanics and Astronomy*, 63, 2020. ISSN 18691927. doi:10.1007/s11433-018-9385-7.
- [9] R Abramishvili, G Adamov, R R Akhmetshin, et al. Comet phase-i technical design report. *Progress of Theoretical and Experimental Physics*, 2020, 3 2020. ISSN 2050-3911. URL: <https://academic.oup.com/ptep/article/doi/10.1093/ptep/ptz125/5805094>, doi:10.1093/ptep/ptz125.
- [10] Valentin Niess, Anne Barnoud, Cristina Cârloganu, and Eve Le Ménèdeu. Backward monte-carlo applied to muon transport. *Computer Physics Communications*, 229:54–67, 8 2018. ISSN 00104655. URL: <https://linkinghub.elsevier.com/retrieve/pii/S0010465518300997>, doi:10.1016/j.cpc.2018.04.001.
- [11] V Niess. Pumas, semi analytical muons -or taus- propagation, backwards. URL: <http://niess.github.io/pumas-pages>.
- [12] Donald E. Groom, Nikolai V. Mokhov, and Sergei I. Striganov. Muon stopping power and range tables 10 mev-100 tev. *Atomic Data and Nuclear Data Tables*, 78:183–356, 2001. ISSN 0092640X. URL: <http://www.sciencedirect.com/science/article/pii/S0092640X01908617>, doi:10.1006/adnd.2001.0861.
- [13] Francesc Salvat. A generic algorithm for monte carlo simulation of proton transport. *Nuclear Instruments and Methods in Physics Research, Section B: Beam Interactions with Materials and Atoms*, 316:144–159, 2013. ISSN 0168583X. URL: <http://www.sciencedirect.com/science/article/pii/S0168583X13009191>, doi:10.1016/j.nimb.2013.08.035.
- [14] F. Salvat, J. D. Martínez, R. Mayol, and J. Parellada. Analytical dirac-hartree-fock-slater screening function for atoms ($z=1-92$). *Physical Review A*, 36:467–474, 7 1987. ISSN 0556-2791. URL: <https://link.aps.org/doi/10.1103/PhysRevA.36.467>, doi:10.1103/PhysRevA.36.467.
- [15] M.J. Boschini, C. Consolandi, M. Gervasi, et al. Nuclear and non-ionizing energy-loss for coulomb scattered particles from low energy up to relativistic regime in space radiation environment. pages 9–23. WORLD SCIENTIFIC, 6 2011. ISBN 978-981-4329-02-6. URL: http://www.worldscientific.com/doi/abs/10.1142/9789814329033_0002, doi:10.1142/9789814329033_0002.
- [16] Robert Piessens. The hankel transform. *The transforms and applications handbook*, 2, 2000.
- [17] S. J. Wallace. Eikonal expansion. *Physical Review Letters*, 27:622–625, 8 1971. ISSN 0031-9007. URL: <https://link.aps.org/doi/10.1103/PhysRevLett.27.622>, doi:10.1103/PhysRevLett.27.622.
- [18] Arthur Erdélyi, W Magnus, F Oberhettinger, and F G Tricomi. Bateman manuscript project. *Higher transcendental functions*, 2:133, 1953.
- [19] Eduard Kuraev, Olga Voskresenskaya, and Alexander Tarasov. Coulomb corrections to the parameters of the molière multiple scattering theory. *Physical Review D*, 89:116016, 6 2014. ISSN 1550-7998. URL: <https://link.aps.org/doi/10.1103/PhysRevD.89.116016>, doi:10.1103/PhysRevD.89.116016.
- [20] Richard H. Helm. Inelastic and elastic scattering of 187-mev electrons from selected even-even nuclei. *Physical Review*, 104:1466–1475, 12 1956. ISSN 0031-899X. URL: <https://link.aps.org/doi/10.1103/PhysRev.104.1466>, doi:10.1103/PhysRev.104.1466.
- [21] H. De Vries, C.W. De Jager, and C. De Vries. Nuclear charge-density-distribution parameters from elastic electron scattering. *Atomic Data and Nuclear Data Tables*, 36:495–536, 5 1987. ISSN

- 0092640X. URL: <https://linkinghub.elsevier.com/retrieve/pii/0092640X87900131>, doi:10.1016/0092-640X(87)90013-1.
- [22] A.V. Butkevich, R.P. Kokoulin, G.V. Matushko, and S.P. Mikheyev. Comments on multiple scattering of high-energy muons in thick layers. *Nuclear Instruments and Methods in Physics Research Section A: Accelerators, Spectrometers, Detectors and Associated Equipment*, 488:282–294, 8 2002. ISSN 01689002. URL: <https://linkinghub.elsevier.com/retrieve/pii/S0168900202004783>, doi:10.1016/S0168-9002(02)00478-3.
- [23] Francesc Salvat, Aleksander Jablonski, and Cedric J. Powell. Elsepa - dirac partial-wave calculation of elastic scattering of electrons and positrons by atoms, positive ions and molecules. *Computer Physics Communications*, 165:157–190, 2005. ISSN 00104655. URL: <http://www.sciencedirect.com/science/article/pii/S0010465504004795>, doi:10.1016/j.cpc.2004.09.006.
- [24] J.A. Jansen, R.Th. Peerdeman, and C. De Vries. Nuclear charge radii of ^{12}C and ^9Be . *Nuclear Physics A*, 188:337–352, 6 1972. ISSN 03759474. URL: <https://linkinghub.elsevier.com/retrieve/pii/0375947472900620>, doi:10.1016/0375-9474(72)90062-0.
- [25] I. Sick and J.S. McCarthy. Elastic electron scattering from ^{12}C and ^{16}O . *Nuclear Physics A*, 150:631–654, 7 1970. ISSN 03759474. URL: <https://linkinghub.elsevier.com/retrieve/pii/0375947470904239>, doi:10.1016/0375-9474(70)90423-9.
- [26] U Fano. Penetration of protons, alpha particles, and mesons. *Annual Review of Nuclear Science*, 13:1–66, 12 1963. ISSN 0066-4243. URL: <http://www.annualreviews.org/doi/10.1146/annurev.ns.13.120163.000245>, doi:10.1146/annurev.ns.13.120163.000245.
- [27] F. Salvat. Penelope-2014: A code system for monte carlo simulation of electron and photon transport, 2015. URL: <https://www.oecd-nea.org/lists/penelope.html>.
- [28] Enrico Fermi. The ionization loss of energy in gases and in condensed materials. *Physical Review*, 57:485–493, 3 1940. ISSN 0031-899X. URL: <https://link.aps.org/doi/10.1103/PhysRev.57.485>, doi:10.1103/PhysRev.57.485.
- [29] U. Fano. Atomic theory of electromagnetic interactions in dense materials. *Physical Review*, 103:1202–1218, 9 1956. ISSN 0031-899X. URL: <https://link.aps.org/doi/10.1103/PhysRev.103.1202>, doi:10.1103/PhysRev.103.1202.
- [30] S. R. Kelner, R. P. Kokoulin, and A. A. Petrukhin. Bremsstrahlung from muons scattered by atomic electrons. *Physics of Atomic Nuclei*, 60:576–583, 1997. ISSN 10637788. [Yad. Fiz.60,657(1997)].
- [31] P A Zyla, R M Barnett, J Beringer, et al. Review of particle physics. *Progress of Theoretical and Experimental Physics*, 2020, 8 2020. ISSN 2050-3911. URL: <https://academic.oup.com/ptep/article/doi/10.1093/ptep/ptaa104/5891211>, doi:10.1093/ptep/ptaa104.
- [32] R. M. Sternheimer. The density effect for the ionization loss in various materials. *Physical Review*, 88:851–859, 11 1952. ISSN 0031-899X. URL: <https://link.aps.org/doi/10.1103/PhysRev.88.851>, doi:10.1103/PhysRev.88.851.
- [33] Mitio Inokuti and David Y. Smith. Fermi density effect on the stopping power of metallic aluminum. *Physical Review B*, 25:61–66, 1 1982. ISSN 0163-1829. URL: <https://link.aps.org/doi/10.1103/PhysRevB.25.61>, doi:10.1103/PhysRevB.25.61.
- [34] R.M. Sternheimer, M.J. Berger, and S.M. Seltzer. Density effect for the ionization loss of charged particles in various substances. *Atomic Data and Nuclear Data Tables*, 30:261–271, 3 1984. ISSN 0092640X. URL: <https://linkinghub.elsevier.com/retrieve/pii/0092640X84900020>, doi:10.1016/0092-640X(84)90002-0.
- [35] Geant4. Geant physics reference manual, 12 2009. URL: <https://geant4-userdoc.web.cern.ch/UsersGuides/PhysicsReferenceManual/html/index.html>.
- [36] L. M. Ter-Mikaelian. *High-Energy Electromagnetic Processes in Condensed Media*, volume 18. John Wiley and Sons, 1972. ISBN 978-0471851905.
- [37] L. D. Landau and I. J. Pomeranchuk. No title. *Dokl. Akad. Nauk. SSSR*, 92:535, 1953.
- [38] A. B. Migdal. Bremsstrahlung and pair production in condensed media at high energies. *Physical Review*, 103:1811–1820, 9 1956. ISSN 0031-899X. URL: <https://link.aps.org/doi/10.1103/PhysRev.103.1811>, doi:10.1103/PhysRev.103.1811.
- [39] S. R. Kelner, R. P. Kokoulin, and A. A. Petrukhin. Direct production of muon pairs by high-energy muons. *Physics of Atomic Nuclei*, 63:1603–1611, 9 2000. ISSN 1063-7788. URL: <http://link.springer.com/10.1134/1.1312894>, doi:10.1134/1.1312894.
- [40] Yu. Andreev, L. Bezrukov, and E. V. Bugaev. Excitation of a target in muon bremsstrahlung. *Physics of Atomic Nuclei*, 57:2066–2074, 1994.
- [41] S. R. Kelner, R. P. Kokoulin, and A. A. Petrukhin. About cross-section for high energy muon bremsstrahlung, 1995. URL: <https://cds.cern.ch/record/288828/files/MEPHI-024-95.pdf>.
- [42] S.R. Kelner, R.P. Kokoulin, and A.A. Petrukhin. Radiation logarithm in the hartree-fock model.

- Physics of Atomic Nuclei*, 62:1894–1898, 1999. ISSN ISSN 1063-7788. URL: https://inis.iaea.org/search/search.aspx?orig_q=RN:35067232, doi:10.1134/1.855464.
- [43] A. Sandrock, S.R. Kelner, and W. Rhode. Radiative corrections to the average bremsstrahlung energy loss of high-energy muons. *Physics Letters B*, 776:350–354, 1 2018. ISSN 03702693. URL: <https://linkinghub.elsevier.com/retrieve/pii/S0370269317309395>, doi:10.1016/j.physletb.2017.11.047.
- [44] Jan Soedingrekso, Alexander Sandrock, and Wolfgang Rhode. The effect of improved high-energy muon cross-sections. *PoS*, 8 2019. URL: <http://arxiv.org/abs/1910.07050>.
- [45] Rostislav Pavlovich Kokoulin and Anatoly Afanasievich Petrukhin. Influence of the nuclear form-factor on the cross-section of electron pair production by high energy muons. volume 4, pages 2436–2444. Proceedings of the 12th International Conference on Cosmic Rays (ICCR 1971), 1971.
- [46] Stanislav Rikhardovich Kelner. Pair production in collisions between muons and atomic electrons. *Physics of Atomic Nuclei*, 61:448–456, 1998.
- [47] A Sandrock, R P Kokoulin, and A A Petrukhin. Theoretical uncertainties of muon transport calculations for very large volume neutrino telescopes. *Journal of Physics: Conference Series*, 1690:012005, 12 2020. ISSN 1742-6588. URL: <https://iopscience.iop.org/article/10.1088/1742-6596/1690/1/012005>, doi:10.1088/1742-6596/1690/1/012005.
- [48] L.B. Bezrukov and E. V. Bugaev. No title. *Soviet Journal of Nuclear Physics*, 33:1195, 1981.
- [49] R.P. Kokoulin. Uncertainties in underground muon flux calculations. *Nuclear Physics B - Proceedings Supplements*, 70:475–479, 1 1999. ISSN 09205632. URL: <https://linkinghub.elsevier.com/retrieve/pii/S0920563298004757>, doi:10.1016/S0920-5632(98)00475-7.
- [50] E. V. Bugaev and Yu. V. Shlepin. Photonuclear interaction of high energy muons and tau leptons. *Physical Review D*, 67:034027, 2 2003. ISSN 0556-2821. URL: <https://link.aps.org/doi/10.1103/PhysRevD.67.034027>, doi:10.1103/PhysRevD.67.034027.
- [51] E. Bugaev, T. Montaruli, Y. Shlepin, and I. Sokalski. Propagation of τ -neutrinos and τ -leptons through the earth and their detection in underwater/ice neutrino telescopes. *Astroparticle Physics*, 21:491–509, 8 2004. ISSN 09276505. URL: <https://linkinghub.elsevier.com/retrieve/pii/S0927650504000544>, doi:10.1016/j.astropartphys.2004.03.002.
- [52] V. Butkevich and S. P. Mikheyev. Cross section of the muon-nuclear inelastic interaction. *Journal of Experimental and Theoretical Physics*, 95:11–25, 7 2002. ISSN 1063-7761. URL: <http://link.springer.com/10.1134/1.1499897>, doi:10.1134/1.1499897.
- [53] Halina Abramowicz and Aharon Levy. The allm parameterization of $\sigma_{\text{tot}}(\gamma * p)$ - an update, 12 1997. URL: <http://arxiv.org/abs/hep-ph/9712415>.
- [54] S. Iyer Dutta, M. H. Reno, I. Sarcevic, and D. Seckel. Propagation of muons and taus at high energies. *Physical Review D - Particles, Fields, Gravitation and Cosmology*, 63:10, 4 2001. ISSN 15502368. doi:10.1103/PhysRevD.63.094020.
- [55] Yung-Su Tsai. Pair production and bremsstrahlung of charged leptons. *Reviews of Modern Physics*, 46:815–851, 10 1974. ISSN 0034-6861. URL: <https://link.aps.org/doi/10.1103/RevModPhys.46.815>, doi:10.1103/RevModPhys.46.815.
- [56] Yung-Su Tsai. Erratum: Pair production and bremsstrahlung of charged leptons. *Reviews of Modern Physics*, 49:421–423, 4 1977. ISSN 0034-6861. URL: <https://link.aps.org/doi/10.1103/RevModPhys.49.421>, doi:10.1103/RevModPhys.49.421.
- [57] I. A. Sokalski, E. V. Bugaev, and S. I. Klimushin. Accuracy of muon transport simulation. 1 2002. URL: <http://arxiv.org/abs/hep-ph/0201122>.
- [58] M.J. Berger. Monte carlo calculation of the penetration and diffusion of fast charged particles. *Methods in Computational Physics*, 1:135–215, 1963.
- [59] J M Fernández-Varea, R Mayol, J Baró, and F Salvat. On the theory and simulation of multiple elastic scattering of electrons. *Nuclear Instruments and Methods in Physics Research Section B: Beam Interactions with Materials and Atoms*, 73:447–473, 1993. ISSN 0168-583X. URL: <http://www.sciencedirect.com/science/article/pii/0168583X9395827R>, doi:http://dx.doi.org/10.1016/0168-583X(93)95827-R.
- [60] K Nagamine, M Iwasaki, K Shimomura, and K Ishida. Method of probing inner-structure of geophysical substance with the horizontal cosmic-ray muons and possible application to volcanic eruption prediction. *Nuclear Instruments and Methods in Physics Research Section A: Accelerators, Spectrometers, Detectors and Associated Equipment*, 356:585–595, 3 1995. ISSN 01689002. URL: <https://linkinghub.elsevier.com/retrieve/pii/0168900294011699>, doi:10.1016/0168-9002(94)01169-9.
- [61] Valentin Niess and Olivier Martineau-Huynh. Danton: A monte-carlo sampler of τ from ν_τ interacting with the earth, 2018.

- [62] Alessandro Lechmann, David Mair, Akitaka Ariga, et al. The effect of rock composition on muon tomography measurements. *Solid Earth*, 9:1517–1533, 12 2018. ISSN 1869-9529. URL: <https://se.copernicus.org/articles/9/1517/2018/>, doi:10.5194/se-9-1517-2018.
- [63] R M Sternheimer and R F Peierls. General expression for the density effect for the ionization loss of charged particles. *Physical Review B*, 3:3681, 1971.
- [64] S Agostinelli et al. {Geant4-}a simulation toolkit. *Nuclear Instruments and Methods in Physics Research Section A: Accelerators, Spectrometers, Detectors and Associated Equipment*, 506:250–303, 2003. ISSN 0168-9002. URL: <http://www.sciencedirect.com/science/article/pii/S0168900203013688>, doi:[http://dx.doi.org/10.1016/S0168-9002\(03\)01368-8](http://dx.doi.org/10.1016/S0168-9002(03)01368-8).
- [65] J. Allison, K. Amako, J. Apostolakis, et al. Geant4 developments and applications. *IEEE Transactions on Nuclear Science*, 53:270–278, 2 2006. ISSN 00189499. doi:10.1109/TNS.2006.869826.
- [66] J. Allison, K. Amako, J. Apostolakis, et al. Recent developments in geant4. *Nuclear Instruments and Methods in Physics Research, Section A: Accelerators, Spectrometers, Detectors and Associated Equipment*, 835:186–225, 2016. ISSN 01689002. doi:10.1016/j.nima.2016.06.125.
- [67] Valentin Niess, Anne Barnoud, Cristina Cârloganu, and Olivier Martineau-Huynh. Turtle: A c library for an optimistic stepping through a topography. *Computer Physics Communications*, 247, 4 2019. ISSN 00104655. URL: <http://arxiv.org/abs/1904.03435><http://dx.doi.org/10.1016/j.cpc.2019.106952>, doi:10.1016/j.cpc.2019.106952.
- [68] Rene Brun and Fons Rademakers. Root — an object oriented data analysis framework. *Nuclear Instruments and Methods in Physics Research Section A: Accelerators, Spectrometers, Detectors and Associated Equipment*, 389:81–86, 4 1997. ISSN 01689002. URL: <https://linkinghub.elsevier.com/retrieve/pii/S016890029700048X>, doi:10.1016/S0168-9002(97)00048-X.
- [69] Mengyun Guan, Ming-Chung Chu, Jun Cao, et al. A parametrization of the cosmic-ray muon flux at sea-level. 9 2015. URL: <http://arxiv.org/abs/1509.06176>.
- [70] Thomas K. Gaisser, Ralph Engel, and Elisa Resconi. Cosmic rays and particle physics. *Cosmic Rays and Particle Physics*, pages 1–444, 2016. doi:10.1017/CB09781139192194.
- [71] D. Attwood, P. Bell, S. Bull, et al. The scattering of muons in low-z materials. *Nuclear Instruments and Methods in Physics Research Section B: Beam Interactions with Materials and Atoms*, 251:41–55, 9 2006. ISSN 0168583X. URL: <https://linkinghub.elsevier.com/retrieve/pii/S0168583X06006756>, doi:10.1016/j.nimb.2006.05.006.
- [72] S.A. Akimenko, V.I. Belousov, A.M. Blik, et al. Multiple coulomb scattering of 7.3 and 11.7 gev/c muons on a cu target. *Nuclear Instruments and Methods in Physics Research Section A: Accelerators, Spectrometers, Detectors and Associated Equipment*, 243:518–522, 3 1986. ISSN 01689002. URL: <https://linkinghub.elsevier.com/retrieve/pii/S0168900286909903>, doi:10.1016/0168-9002(86)90990-3.
- [73] Ryuichi Nishiyama, Akimichi Taketa, Seigo Miyamoto, and Katsuaki Kasahara. Monte carlo simulation for background study of geophysical inspection with cosmic-ray muons. *Geophysical Journal International*, 206:1039–1050, 2016. ISSN 1365246X. doi:10.1093/gji/ggw191.
- [74] J Baró, J Sempau, J M Fernández-Varea, and F Salvat. Penelope: An algorithm for monte carlo simulation of the penetration and energy loss of electrons and positrons in matter. *Nuclear Instruments and Methods in Physics Research Section B: Beam Interactions with Materials and Atoms*, 100:31–46, 1995. ISSN 0168-583X. URL: <http://www.sciencedirect.com/science/article/pii/S0168583X95003495>, doi:[http://dx.doi.org/10.1016/0168-583X\(95\)00349-5](http://dx.doi.org/10.1016/0168-583X(95)00349-5).
- [75] J. Sempau, E. Acosta, J. Baró, et al. An algorithm for monte carlo simulation of coupled electron-photon transport. *Nuclear Instruments and Methods in Physics Research, Section B: Beam Interactions with Materials and Atoms*, 132:377–390, 1997. ISSN 0168583X. URL: <http://www.sciencedirect.com/science/article/pii/S0168583X9700414X>, doi:10.1016/S0168-583X(97)00414-X.
- [76] Charles R Harris, K Jarrod Millman, Stéfan J van der Walt, et al. Array programming with numpy. *Nature*, 585:357–362, 9 2020. ISSN 0028-0836. URL: <https://www.nature.com/articles/s41586-020-2649-2>, doi:10.1038/s41586-020-2649-2.
- [77] John D Hunter. Matplotlib: A 2d graphics environment. *Computing in Science & Engineering*, 9:90–95, 2007. ISSN 1521-9615. URL: <http://ieeexplore.ieee.org/document/4160265/>, doi:10.1109/MCSE.2007.55.
- [78] Gert Molière. Theorie der streuung schneller geladener teilchen i. einzelstreuung am abgeschirmten coulomb-feld. *Zeitschrift für Naturforschung A*, 2:133–145, 3 1947. ISSN 1865-7109. URL: <https://www.degruyter.com/document/doi/10.1515/zna-1947-0302/html>, doi:10.1515/zna-1947-0302.
- [79] F. N. Fritsch and J. Butland. A method for constructing local monotone piecewise cubic interpolants. *SIAM Journal on Scientific and Statistical Computing*, 5:300–304, 6 1984. ISSN 0196-5204.

- URL: <http://epubs.siam.org/doi/10.1137/0905021>, doi:10.1137/0905021.
- [80] D.J. Higham. Monotonic piecewise cubic interpolation, with applications to ode plotting. *Journal of Computational and Applied Mathematics*, 39:287–294, 5 1992. ISSN 03770427. URL: <https://linkinghub.elsevier.com/retrieve/pii/037704279290205C>, doi:10.1016/0377-0427(92)90205-C.

Table C.5: Nuclear charge radii, in fm, used in PUMAS for various atomic elements. The nuclear charge radii, $\sqrt{\langle r^2 \rangle}$, are given for isotopic mixtures with atomic mass A according to the PDG. The radii have been fitted from Vries et al. [21] using the procedure described in Appendix C. (*) Note that “rockium” (Rk) is a fictitious element used in standard rock.

symbol	Z	A	$\sqrt{\langle r^2 \rangle}$	symbol	Z	A	$\sqrt{\langle r^2 \rangle}$
H	1	1.008	0.858	Pr	59	140.908	4.897
D	1	2.0141	2.098	Nd	60	144.242	4.927
He	2	4.0026	1.680	Pm	61	144.913	4.948
Li	3	6.94	2.400	Sm	62	150.36	5.054
Be	4	9.01218	2.518	Eu	63	151.964	5.093
B	5	10.81	2.405	Gd	64	157.25	5.133
C	6	12.0107	2.470	Tb	65	158.925	5.177
N	7	14.007	2.548	Dy	66	162.5	5.197
O	8	15.999	2.734	Ho	67	164.93	5.210
F	9	18.9984	2.900	Er	68	167.259	5.264
Ne	10	20.1797	2.993	Tm	69	168.934	5.301
Rk*	11	22.00	2.958	Yb	70	173.054	5.390
Na	11	22.9898	2.940	Lu	71	174.967	5.371
Mg	12	24.305	3.043	Hf	72	178.49	5.429
Al	13	26.9815	3.035	Ta	73	180.948	5.479
Si	14	28.0855	3.098	W	74	183.84	5.423
P	15	30.9738	3.187	Re	75	186.207	5.400
S	16	32.065	3.245	Os	76	190.23	5.409
Cl	17	35.453	3.360	Ir	77	192.217	5.411
Ar	18	39.948	3.413	Pt	78	195.084	5.387
K	19	39.0983	3.408	Au	79	196.967	5.318
Ca	20	40.078	3.477	Hg	80	200.592	5.404
Sc	21	44.9559	3.443	Tl	81	204.38	5.471
Ti	22	47.867	3.595	Pb	82	207.2	5.498
V	23	50.9415	3.600	Bi	83	208.98	5.520
Cr	24	51.9961	3.644	Po	84	208.982	5.520
Mn	25	54.938	3.681	At	85	209.987	5.529
Fe	26	55.845	3.748	Rn	86	222.018	5.629
Co	27	58.9332	3.843	Fr	87	223.02	5.637
Ni	28	58.6934	3.776	Ra	88	226.025	5.661
Cu	29	63.546	3.943	Ac	89	227.028	5.669
Zn	30	65.38	3.942	Th	90	232.038	5.710
Ga	31	69.723	4.032	Pa	91	231.036	5.701
Ge	32	72.63	4.065	U	92	238.029	5.784
As	33	74.9216	4.078	Np	93	237.048	5.825
Se	34	78.971	4.123	Pu	94	244.064	5.824
Br	35	79.904	4.135	Am	95	243.061	5.817
Kr	36	83.798	4.188	Cm	96	247.07	5.843
Rb	37	85.4678	4.209	Bk	97	247.07	5.843
Sr	38	87.62	4.237	Cf	98	251.08	5.868
Y	39	88.9058	4.249	Es	99	252.083	5.875
Zr	40	91.224	4.306	Fm	100	257.095	5.906
Nb	41	92.9064	4.318	Md	101	258.098	5.912
Mo	42	95.95	4.363	No	102	259.101	5.918
Tc	43	97.9072	4.388	Lr	103	262.11	5.937
Ru	44	101.07	4.432	Rf	104	267.122	5.967
Rh	45	102.906	4.435	Db	105	268.126	5.973
Pd	46	106.42	4.479	Sg	106	269.129	5.979
Ag	47	107.868	4.520	Bh	107	270.133	5.985
Cd	48	112.414	4.612	Hs	108	269.134	5.980
In	49	114.818	4.646	Mt	109	278.156	6.033
Sn	50	118.71	4.640	Ds	110	281.164	6.051
Sb	51	121.76	4.630	Rg	111	282.169	6.056
Te	52	127.6	4.714	Cn	112	285.177	6.074
I	53	126.904	4.706	Nh	113	286.182	6.079
Xe	54	131.293	4.756	Fl	114	289.19	6.097
Cs	55	132.905	4.774	Mc	115	289.194	6.097
Ba	56	137.327	4.823	Lv	116	293.204	6.119
La	57	138.905	4.848	Ts	117	294.211	6.125
Ce	58	140.116	4.878	Og	118	294.214	6.125